CARBON MATERIAL BASED MICROELECTROMECHANICAL SYSTEM (MEMS): FABRICATION AND DEVICES

A Dissertation
Presented to
The Academic Faculty

by

Wenjun XU

In Partial Fulfillment
of the Requirements for the Degree
Doctor of Philosophy in the
School of Materials Science and Engineering

Georgia Institute of Technology
May 2011

CARBON MATERIAL BASED MICROELECTROMECHANICAL SYSTEM (MEMS): FABRICATION AND DEVICES

Approved by:

Dr. Mark G.Allen, Advisor
School of Electrical and Computer Engineering
Georgia Institute of Technology

Dr. David Bucknall
School of Materials Science and Engineering
Georgia Institute of Technology

Dr. Dennis W. Hess
School of Chemical and Biomolecular Engineering
Georgia Institute of Technology

Dr. Satish Kumar
Materials Science and Engineering
Georgia Institute of Technology

Dr. Donggang Yao
School of Materials Science and Engineering
Georgia Institute of Technology

Date Approved: [March,28 , 2011]

To my grandma, Yunlan LI, and my family

ACKNOWLEDGEMENTS

This work will not be finished within four years without the help from many people. Frist, I would like to express my gratitude to Dr. Mark G. Allen for being a knowledgeable, insightful and helpful advisor throughout my study period. His ability to come up with creative ideas to resolve difficult research problems have always amazed and inspired me.

I have received kind support from my committee members, Dr. David Bucknall, Dr. Dennis Hess, Dr. Satish Kumar and Dr. Donggang Yao. I want to thank them whole heartedly for their time to read my dissertation and give useful advices and comments to my work.

Special thanks go to Mr. Richard Shafter for the technical support and providing me with all kinds of customized experimental setups. I also want to thank Ms. Purnima Sharma for all the administrative assistance. I would like to thank Dr. Mike Kranz, Mr. Chao Song, Dr. Seungkeun Choi, Dr. Maxine McClain, and Dr. Oliver Brand for all the valuable discussions and great help in my PhD projects, as well as many MSMA group members, whom made my time in graduate school a very enjoyable one.

My family and friends deserve my most sincere gratitude. They have made my PhD life not just about equations and equipment. I would like to delicate this dissertation to my parents for their constant emotional support, understanding, patience and encouragement over the course of my studies. Special thanks go to grandmother, Yulan Li, an ordinary and extraordinary woman. Though she has been long gone, her strength and unconditional love have always inspired me along the way, and to her I want to delicate this dissertation as well.

TABLE OF CONTENTS

LIST OF TABLES

LIST OF FIGURES

SUMMARY

This PhD dissertation presents the exploration and development of two carbon materials, carbon nanotubes (CNTs) and carbon fiber (CF), as either key functional components or unconventional substrates for a variety of MEMS applications. Their performance in three different types of MEMS devices, namely, strain/stress sensors, vibration-powered generators and fiber solar cells, were evaluated and the working mechanisms of these two non-traditional materials in these systems were discussed. The work may potentially enable the development of new types of carbon-MEMS devices.

Carbon nanotubes were selected from the carbon family due to several advantageous characteristics that this nanomaterial offers. They carry extremely high mechanical strength (E_y=1TPa), superior electrical properties (current density of 4×10^9 A/cm^2), exceptional piezoresistivity (G=2900), and unique spatial format (high aspect ratio hollow nanocylinder), among other properties. If properly utilized, all these merits can give rise to a variety of new types of carbon nanotube based micro- and nano-electronics that can greatly fulfill the need for the next generation of faster, smaller and better devices. However, before these functions can be fully realized, one substantial issue to cope with is how to implement CNTs into these systems in an effective and controllable fashion. Challenges associated with CNTs integration include very poor dispersibility in solvents, lack of melting/sublimation point, and unfavorable rheology with regard to mixing and processing highly viscous, CNT-loaded polymer solutions. These issues hinder the practical progress of CNTs both in a lab scale and in the industrial level.

To this end, a MEMS-assisted electrophoretic deposition technique was developed, aiming to achieve controlled integration of CNT into both conventional and flexible microsystems at room temperature with a relatively high throughput. MEMS technology has demonstrated strong capability in developing silicon and metal based microsystems. In this thesis, this mature technique was exploited to generate a variety of microelectrode structures to facilitate the micropatterning and manipulation of the CNTs. Selective deposition of electrically charged CNTs onto desired locations was realized in an EPD process through patterning of electric field lines created by the microelectrodes fabricated through MEMS techniques. A variety of 2-D and 3-D micropatterns of CNTs with wafer-scale areas have been successfully achieved in both rigid and elastic systems. The thickness and morphology of the generated CNT patterns was found to be readily controllable through the parameters of the fabrication process. Studies also showed that for this technique, high surface hydrophobicity of the non-conductive regions in microstructures was critical to accomplish well-defined selective micropatterning of CNTs.

Upon clearing the hurdles of the CNT manipulation, a patterned PDMS/CNT nanocomposite was fabricated through the aforementioned approach and was incorporated, investigated and validated in elastic force/strain microsensors. The gauge factor of the sensor exhibited a strong dependence on both the initial resistance of the device and the applied strain. Detailed analysis of the data suggests that the piezoresistive effect of this specially constructed bi-layer composite could be due to three mechanisms, and the sensing mechanism may vary when physical properties of the CNT network embedded in the polymer matrix alter.

The feasibility of the PDSM/CNT composite being utilized as an elastic electret was further explored. The nanocomposite composed of these two non-traditional electret materials exhibited electret characteristics with reasonable charge storage stability when charged using a corona discharge. The power generation capacity of the corona-charged composite has been characterized and successfully demonstrated in both a ball drop experiment and cyclic mechanical load experiments.

Lastly, in an effort to develop carbon-material-based substrates for MEMS applications, a carbon fiber-based poly-Si solar cell was designed, fabricated and investigated. This fiber-type photovoltaics (PV) takes advantage of the excellent thermal stability, electrical conductivity and spatial format of the CF, which allows CF to serve as both the building block and the electrode in the PV configuration. The photovoltaic effects of the fiber PV were demonstrated with an open-circuit voltage of 0.14 V, a short-circuit current density of 1.7 mA/cm^2, and output power density of $0.059mW/cm^2$. The issues of this system were discussed as well.

CHAPTER 1

INTRODUCTION

The element carbon occurs in all known living organisms on Earth and is the basis for organic chemistry. It forms more compounds than any other element, with nearly ten million pure organic compounds reported to date. However, this is only a tiny fraction of those that have been theoretically predicted under standard conditions[1]. Many thousands of these compounds are vital to organic and life processes. Carbon possesses the highest melting and sublimation point (T_s=3900 K) among all known elements.

One unique aspect of this element is the variety of forms it can assume when carbon atoms connect with each other exclusively and generate different molecular configurations/spatial arrangements. The resultant carbon allotropes play very important roles in modern technology and industry due to their diverse properties which span a range of extremes[2,3]. Three of the most common carbon allotropes are diamond, graphene/ graphite, and amorphous carbon, each of which is categorized with respect to the type of orbital hybridizations of a carbon atom, namely, sp^3, sp^2, and sp hybridization. Newly discovered family members are fullerenes, which include carbon nanotubes (CNTs), carbon nanobuds, and buckyballs, to name a few. The physical and chemical properties of the allotropes are largely determined by the specific molecular configurations, which make the characteristics of one carbon material significantly different from another.

For instance, diamond is composed of tetrahedrally-bonded carbon atoms with sp^3 hybridization, as illustrated in Figure 1.1. The tetrahedrons in a diamond structure formed

by covalently-bonded carbon atoms create a 3-dimensional network with hexagonal carbon rings, allowing for zero bond angle strain and endowing the material with an incredibly high mechanical strength. Diamond is known as a transparent crystal with excellent electrical insulating properties, which has the highest hardness (Mohs=10) and thermal conductivity (900-2300 $W \cdot m^{-1} \cdot K^{-1}$) of any bulk material. As a result, diamond can be used as heat sinks for electronics and in polishing/grinding tools[4].

Graphene, on the other hand, consists of a one-atom-thick 2-D planar sheet with fused hexagonal rings which are composed of sp^2-bonded carbon atoms. It is an opaque material and possesses extraordinary electrical conductivity, as well as exceptional mechanical and heat resistant properties. In contrast to diamond where all four outer electrons of a carbon atom are immobilized through covalent bonding, each carbon atom in graphene contributes one electron to a delocalized system of electrons which is also a part of the chemical bonding. Graphene thereby conducts electricity due to the

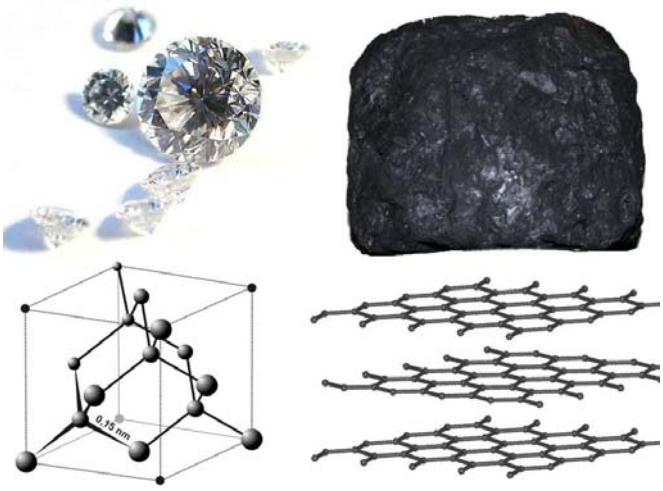

Figure 1.1: Image and structure of a diamond (left) and graphite (right).

delocalization of these *pi* bond electrons above and below the planes of the carbon atoms. It is considered as a promising candidate to replace silicon for the next generation of high performance electronics. Stacking graphene sheets with an interplanar spacing of 0.335 nm gives rise to the most stable form of carbon under standard conditions, graphite. Unlike diamond, graphite is soft enough to form a streak on paper (with its name originated from the Greek word "to write") due to the weak van der Waals forces between the graphene layers, and it has been exploited in a variety of fields including battery electrodes, reentry shields for missile nosecones, solid rocket engines, high temperature reactors, brake shoes and electric motor brushes[5].

Amorphous carbon contains a mixture of sp^3, sp^2, and *sp* hybridized carbon. The most common form of this allotrope is carbon black which usually exists as spherical particles. Carbon black is a very important black pigment for the ink and coating industries. The sp^2 and *sp* hybridized atoms in its structure endow it with a reasonable electrical conductivity and therefore it has been utilized as an inexpensive popular conductive filler in multiple applications[6].

It can be seen that carbon materials are available in a large variety of characteristics and structures, some of which carry very unique and promising attributes that can benefit modern microelectronics. Among all the allotropes, carbon nanotubes (CNTs) and carbon fiber (CF) possess their own unique properties, which have demonstrated great potential in high performance modern electronics, especially in microsystems. Their mechanical, electrical and dimensional characteristics are extremely suitable for applications in MicroElectroMechanical System (MEMS) and it is therefore

of our particular interest in this PhD study to develop microelectronic devices based on allotropes of carbon.

1.1 Overview of CNTs

1.1.1 Structural Properties of CNTs

Wrapping a single graphene sheet to form a seamless hollow cylinder, instead of stacking the sheets into a graphite structure, creates a nanomaterial termed single wall carbon nanotube (SWCNT), as shown in Figure 1.2. This material exhibits a high length-to-diameter ratio of up to 132,000,000:1 and is viewed as a quasi-1D single molecule[7]. The high-aspect-ratio hollow nanowire architecture can be regarded as a perfect arrangement of carbon-carbon bonds with sp^2 hybridized atoms oriented along the axis direction.The way the graphene sheet is wrapped is represented by a pair of chiral vector indices (n, m). The n and m denote the number of unit vectors along two directions in the honeycomb crystal lattice of graphene. $m = 0$ gives zigzag chirality and $n = m$ leads to an armchair structure. Others are called "chiral". The electrical property of a SWCNT largely depends on the chirality[8]. Furthermore, with multiple rolled layers or concentric tubes of single graphene sheets, another variety named multi-wall carbon nanotube (MWCNT) can be generated, sharing similar spatial format with SWCNT as illustrated in Figure 1.3. The bending of a planar graphene sheet shown in Figure 1.1 into a cylinder with a diameter of less than 10nm (Figure 1.2) introduces significant alternation of the electronic density of states among the carbon atoms. It causes certain aspects of the anisotropic properties of graphene to disappear and gives rise to various peculiar yet appealing characteristics to CNTs[8], which will be discussed shortly. Though the growth mechanism remains obscure so far, its unique electronic, mechanical, optical, thermal and

chemical properties have triggered intensive interest in the past two decades and have simulated extensive studies. The nano-diameter and macro-length spatial geometry is extremely suitable for the emerging nanotechnology and nano/microelectronics applications.

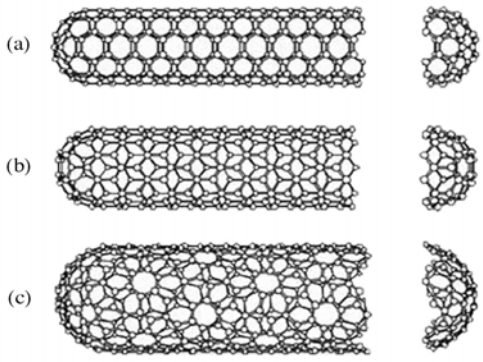

Figure 1.2: Structure of a SWCNT with (a) armchair, (b) zigzag, and (c) chiral chirality.

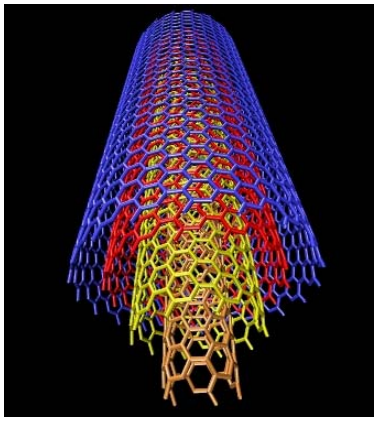

Figure 1.3: Structure of a MWCNT.

1.1.2 Mechanical Properties of CNTs

Carbon-carbon covalent bonds are one of the strongest in nature. A structure based on the perfect arrangement of these bonds oriented along the axis can produce an exceedingly strong material. Indeed, defect-free CNTs are the stiffest and strongest materials yet discovered in terms of tensile strength (63 GPa) and elastic modulus (~1 TPa). Table 1.1 compares mechanical properties of CNTs with two other common high strength materials, stainless steel and Kevlar® (poly-paraphenylene terephthalamide fiber). CNTs exhibit superior properties to the latter two materials. The CNT usually exhibited an elastic strain of 5% and subsequently shows plastic deformation before fracture. This property is promising for mechanical energy storage as demonstrated in a watch by Livermore *et al* [9]. The superior mechanical properties are therefore very attractive in structural reinforcement applications such as in aerospace, combing with other benefits such as low density (1.3 ~1.4 $g \cdot cm^{-1}$) and high aspect ratio[10]. Many applications have been proposed ranging from everyday products like sports gear to combat jackets and space elevators[11]. CNT fibers, yarns and sheets consisting of pure CNTs have been commercialized by *Nanocomp Technologies Inc*., where the fiber is spun continuously from the CNT vapor phase and makes the mass production of CNT products possible. CNT fibers have the potential to serve as ultra high strength yet lightweight fibers, electronic interconnects, power conversion, motors, transformers and electro-storage devices[12]. Moreover, novel applications such as single CNT-based nanoprobe in methodology and chemical/biological investigation have been demonstrated[13] owing to the nano-sized tip and superior mechanical strength of a CNT. CNT tips can further be chemically modified in a variety of ways due to the all-carbon

structure, which brings multi-functionality to the CNT nanoprobe and can be used in drug delivery, molecular recognition, chemically sensitive imaging and local chemical patterning.

Table 1.1 Comparison of mechanical properties

Material	Young's modulus (TPa)	Tensile strength (GPa)	Elongation at break (%)
SWCNT	~1 (from 1 to 5)	13–53	16
MWCNT	0.27[14]–0.95[14]	11[14]-150[15]	N/A
Stainless Steel	0.186–0.214	0.38–1.55	15–50
Kevlar®	0.06–0.18[16]	3.6–3.8[16]	~2

The mechanical stiffness in the radial direction of the CNT is much lower, primarily due to its hollow structure and high aspect ratio. TEM observation of the radial elasticity suggested that even the van der Waals force can deform two adjacent nanotubes[17]. The Young's modulus in the radial direction was found to be on the order of several GPa by several nanoindentation experiments on MWCNTs[18]. As the conductivity of a CNT can be greatly altered under stress or strain, this "soft" characteristic in the radial direction may potentially enhance the performance of CNTs in piezoresistive force or strain sensing, which will be discussed in detail in Chapter 3.

1.1.3 Electrical Properties of CNTs

One interesting property of the 1-D structure of CNTs arises from a substantial change of the electronic properties mainly induced by correlation effects among electrons constrained in one direction within a nanoscale curved tube. This geometry endows CNT with unique electronic properties that can excel in various types of modern electronics. In a quasi-1D nanostructure such CNT, the electrons can only propagate along the longitudinal direction, which approaches the near-ballistic electronic transport type and leads to an outstanding conductivity of the CNT[19]. Depending on the chirality, the curvature and the bandgap, the CNT can be either metallic or semiconductive. Theoretical studies suggest that metallic CNTs can carry an electrical current density of 4×10^9 A/cm^2, which outperforms metals such as copper by three orders of magnitude[20].

Other outstanding characteristics of this versatile nanomaterial have also been discovered in a wide range of electronics including room-temperature ballistic transistors, electron field emitters, energy storage, supercapacitors, flat panel display, device coolers, paper battery, solar cells, light emitting diodes, nanoradio, GHz mechanical oscillators, and flywheels, to name a few[21]. The application of CNTs can be further extended to other devices such as creating extremely small motors[22] produced from a single CNT. It is considered as the one of the first true examples of molecular nanotechnology, fabricating devices by precisely positioning atoms. In addition to electronics, CNTs may be useful in biomedical fields as well. Preliminary study has also shown that SWCNTs may be useful in Kanzius cancer therapy, in which they were inserted around cancerous cells and excited with radio waves. The heat generated subsequently killed the cells surrounding the CNTs. Carbon nanotubes have also served as scaffold for bone growth in tissue

engineering[23]. More importantly, under the appropriate wetting effects this nano-sized hollow structure can act as a high aspect ratio nano-template, which enables a new way to generate other nanomaterials. One-dimensional coatings/fillings of CNTs have been successfully created and the resultant composite combines the metallic/semiconductive properties of the CNTs and the properties of the foreign materials into low-dimensional systems[24,25].

Among all the distinctive characteristics of CNTs, one of the most interesting properties is that carbon atoms in a CNT are able to rehybridize in response to applied strain/stress, with certain degree of sp^2 to sp^3 transition. Such peculiar behavior results in a promising application in piezoresistive strain/stress sensing, as the electrical properties such as resistance are greatly affected by the deformation of the CNT. As discussed in 1.1.2, the compressive force can easily cause a CNT to bend, flatten or twist, which gives rise to a very high piezoresistive effect due to the alteration of its electronic transport properties. Indeed, a gauge factor of 2900[26,27] has been reported, which far exceeds the traditional metal foil strain gauge (G=2) and silicon piezoresistors[28] (G<150). Similarly, absorption of various gases (NO_x, NH_3, etc.) or chemicals onto CNTs also lead to the modification of their electron transport properties. This phenomenon further provides CNTs with chemical/gas sensing ability[29].

With the nano-scale dimensions and aforementioned unique properties, CNT is likely to benefit the modern micro/nano electronics and biomedical technology, and help them to meet the requirement for next generation of smaller, smarter and faster electronics.

1.1.4 Carbon Nanotube-Polymer Composites

Besides functioning as the format of an individual CNT, an entangled CNT network can serve as electrically conductive path or structural reinforcement component[30]. Incorporating such a network into a matrix such as polymer, metal or ceramic can endow the composite with multi-functionality such as electrical conductivity, high mechanical strength, electromagnetic shielding, and enhanced charge separation/transport for energy conversion. Unlike traditional composites where only one material property (i.e., mechanical properties: strength, toughness, or ductility) is enhanced, multiple functions such as structure, sensing, actuation, and power generation, among others can be achieved simultaneously within one CNT nanocomposite. Among these composites, polymer-CNT composites are of our particular interest due to the large variety of chemical/physical properties available in polymers. Similar to the individual CNT, the nanocomposites combining interesting characteristics of CNTs with polymers have demonstrated great potential in multiple applications such as supercapacitors, gas/bio sensors, photovoltaic cells, photodiodes, optical limiting devices, solar cells, high-resolution printable conductors, electromagnetic absorbers, and advanced transistors[8]. For instance, CNTs-loaded conducting organic polymers (COP) have proved to be promising in organic electronics[31]. Kim *et al.* reported nanocomposites based on PMMA and MWCNTs exhibiting a significant enhancement in the electrical conductivity of the polymer. A value of 3000 S/mat at a concentration of 0.4 wt % with an extremely low percolation threshold (around 0.003 wt%) has been achieved[32]. In the biomedical area, Bhattacharya *et al.* reported bone formation on carbon nanotube composite[33]. When implanted in critical-sized rat calvarial defect, the CNT-composite permitted bone formation and bone repair without signs of rejection or inflammation.

Load transfer from the matrix to the embedded CNT network can effectively increase the overall mechanical strength of the polymers. Since the early preparation of a CNT/epoxy composite by Ajayan[34] *et al.* in 1994, more than 30 polymer matrices have been investigated with respect to mechanical reinforcement through CNTs[35]. The outstanding reinforcement potential of CNTs is evident from the super tough composite fibers fabricated by groups of Baughman[36] and Poulin[37]. By optimizing a "coagulation spinning" method, they spun several hundred meters of composite fibers of CNT/PVA, which exhibit excellent tensile properties comparable to that of a spider silk (Young's modulus and strength of approximately 80GPa and 1.8 GPa, respectively).

1.1.5 Challenges of Integration of CNTs into Microelectronics

The superior mechanical, electrical and structural properties of CNTs have suggested their great potential in a wide range of fields, especially in modern microelectronics. Moreover, implementing these properties into flexible/stretchable systems can not only build microelectronics that cover arbitrary curvatures, but also enable pressure monitoring inside human body and energy scavenging from low-frequency motions. A significant challenge for the rapid progress of many of the aforementioned CNT-based applications is the manipulation of CNTs, especially in the micro/nanoscale, since CNTs have neither melting point nor sublimation point and therefore can not be directly vapor-deposited/sputtered into the systems like metals, except through in-situ synthesis. The nano-diameter and high surface area of CNTs induce high van der Waals forces between the tubes, resulting in a strong tendency to aggregate with each other in order to minimize the total surface energy. Hence CNTs have very limited dispersibility in most solvents, which further imposes a challenge in the

spin casting process. These issues have brought a question of how to precisely pattern and position CNTs onto desired locations in a particular micro/nano-system, given the fact that controlled integration of the functional component is critical for both the reliability and reproducibility of a device and a system. For instance, one basic building block of microelectromechanical systems (MEMS) processing is the ability to deposit thin films of material with a controlled thickness anywhere between a few nanometers to above 100 micrometers, which is not readily available in the present CNT integration process.

Another obstacle to tackle is how to fabricate nanocomposites with high weight fraction of CNTs, considering the extremely high viscosity of the CNT-polymer mixture during the processing induced by the high surface area of CNTs. This rheology issue limits practical progress of this type of composite when patterns with high CNTs loading are desirable such as conductive composite in flexible systems[38]. The work in this thesis therefore developed a new technique to facilitate controllable CNT patterning and manipulating, which will be discussed in details in the Chapter 2 and 3. Both the strain/stress sensing and power generation capacities of the resultant polymer/CNTs nanocomposite have been demonstrated in Chapter 3 and Chapter 4.

1.2 Overview of Carbon Fiber

Another focus in this thesis is to develop carbon fiber (CF) based electronics. Carbon fiber shares similar spatial format, as well as mechanical and electrical performance with its relative, CNTs. It is a well-developed and well-understood carbon material and is one of the most important textile products. Carbon fiber has a graphite structure, where 2-D graphene sheets stacked layer by layer with an interplanar distance

of 0.335 nm in to a 3-D structure as discussed previously. Therefore it is an electrical conductor with a conductance of 10^5 S/m. The fiber typically has a micro-scale diameter ranging from 5-10 μm and macrometer length up to hundreds of meters. Carbon atoms in the CF form microscopic crystals and generate a certain degree of alignment along the longitudinal axis of the fiber. This gives rise to a superior mechanical strength with a Young's Modulus of 530 GPa, as well as good thermal conductivity and chemical resistance. CF possesses a specific strength (strength/density) of 3 times of that of steel[39, 40] and is an excellent load-bearing reinforcement material in composites. In addition, as carbon fiber is synthesized through pyrolysis of precursor polymers such as polyacrylonitrile (PAN) at a temperature of up to 2500 °C, it shows very high thermal stability. These properties such as high tensile strength, thermal stability, lightweight and low thermal expansion have made CF a very popular reinforcement material for polymers, ceramics or metals in aerospace, civil engineering, military, and motorsports[41]. The mass production of carbon fiber is a well-established roll-to-roll process in the textile industry, which greatly reduces its cost and is appealing for large-area wearable electronics applications.

It is believed that much of the fuselage of the new Boeing 787 Dreamliner and Airbus A350 XWB will be made of carbon fiber reinforced polymers (CFRP), making the aircraft lighter than a comparable aluminum fuselage, with an additional benefit of less maintenance due to CFRP's superior fatigue resistance. Another application is in construction of high-end audio components such as turntables and loudspeakers because of its high stiffness. Fire resistance of polymers or thermoset composites can be significantly improved if a thin layer of carbon fibers is molded near the surface, where a

dense, compact layer of carbon fibers can efficiently reflect heat[42]. Lenovo/IBM and Sony have utilized CF as covers for lightweight and impact resistance laptops.

In addition to serving as a reinforcement material, carbon fiber is also a popular choice as electrodes in fuel cells, batteries and other electrochemical applications[43]. Researchers recently have begun to integrate it into devices such as MEMS scanning micro-mirror array[44] and ZnO-based solar cells[45], combing both the excellent mechanical and electrical properties, together with its high-aspect-ratio spatial geometry.

1.3 Microelectromechanical Systems (MEMS)

1.3.1 MEMS Technology in General

MEMS in general is defined as the utilization of fabrication techniques associated with integrated circuits to construct micro-scale mechanical structures, typically on semiconductor substrates[46]. MEMS manufacturing technology refers to a number of microfabrication processes including physical deposition (PVD), chemical deposition (CVD), photolithography, etching, surface/bulk micromachining, molding, and plating, to name a few. It has proved to be a very powerful batch fabrication technique which can generate a variety of 2D and 3D micro-scale structures over a large variety of both organic and inorganic materials such as silicon, metal, polymer and dielectrics[47,48,49], as shown in Figure 1.4 (a).

On the other hand, MEMS can refer to a device system including small machines with micro scale functional elements/structures usually fabricated though the techniques mentioned above. By scaling down the macro-scale transducer design concepts through both “top-down” and “bottom-up” design methodology of MEMS technologies, a diverse collection of miniaturized transducers[50] have been realized including

accelerometers, gyroscopes, gas sensors, ultrasonic transducers, and pressure sensors, among many others, some of which are shown in Figure 1.4 (b). Miniaturization offers

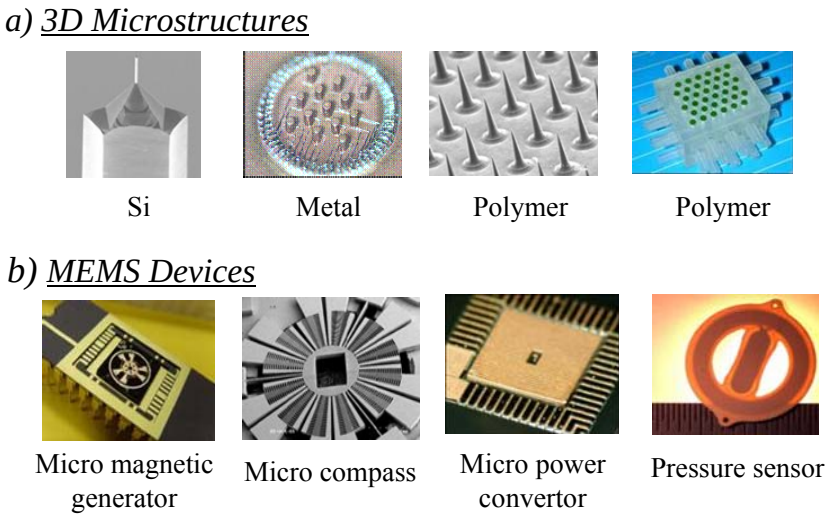

Figure 1.4: MEMS microstructures and devices (image courtesy of MSMA Group at GaTech).

multiple benefits. First, reduction in size and weight is critically important for applications in portable devices or space-based structural systems (*e.g.*, rockets and satellites). Second, smaller devices are easier to install, particularly if the sensor is densely-distributed and embedded within structural components. Moreover, miniaturization may sometimes lead to potential improvements in performance lif scaling laws that are favorable over their macro-scale counterparts[51], while simultaneously gaining significant reductions in fabrication costs engendered through the batch processing capability of MEMS technology. Last but not least, adoption of IC fabrication technologies can co-locate MEMS devices with computing and wireless communication circuits, offering complete system-on-a-chip solutions[51].

1.3.2 Carbon-MEMS

MEMS, since its beginning, has been applied primarily as a versatile and powerful technology for developing silicon and metal based microsystems. More recently, MEMS devices/structures based on carbon materials, termed Carbon MEMS (C-MEMS), start to gain increased scientific attention. C-MEMS is a microfabrication technique, where photoresists are patterned and then pyrolyzed in an inert environment (e.g vacuum or forming gas) to yield all-carbonaceous structural and functional materials[52,53,54]. The resultant material enables an entire new variety of MEMS devices which exploits carbon structures having a wide variety of shapes, resistivity and mechanical properties. Moreover, carbon surfaces form excellent electrochemical electrodes and are easier to derivatize with organic molecules than other traditional MEMS materials such as silicon and metals. The mechanical/physical properties of the carbon structure can be tailored by chemical reaction of the carbon atoms with many other types of elements to generate various organic compounds, which expands the MEMS into a series of new applications such as bio sensing, chemical sensing, and organic electronics fields.

The shape and geometry of the carbon structures are primarily determined by the initial patterning process. Well-developed techniques such as traditional photolithography, inclined photolithography and stereolithography permit highly diversified 2D and 3D complex carbon structures to be fabricated[55], some of which are unattainable from silicon or metals. The ability to form densely packed 3-D microstructures with large surface area associated with the 3D spatial geometry is extremely favorable in devices such as mini-battery and solar cells where the

performance relies substantially on the total effective surface area and small footprint is desired simultaneously. For instance, Madou[56,57] *et al.* have exploited an array of high aspect ratio carbon micro-pillars produced from pyrolysis as a 3D microelectrode array in a miniaturized battery. The 3D battery exhibited a higher current density and energy density than that of the 2D battery, with a suitable reduction in footprint. Piezoresistive sensing is another potential application for this type of microstructure.

In addition to conductive carbon structures, diamond and diamond-like carbon (DLC) MEMS have also been designed and developed[58,59,60]. The superior properties of diamond such as high Young's modulus, hardness, high thermal conductivity and low thermal expansion coefficient have been brought into relevant MEMS devices. Applications of diamond and DLC films in MEMS are in two categories: surface coatings and structural materials. Thin diamond and DLC coatings mainly improve the wear and friction resistance of micro-components and reduce stiction between microstructures and their substrates. The biocompatibility of the coating also opens new applications for the devices in implantable biomedical systems. Meanwhile, the high elastic modulus of diamond and DLC films has been exploited in the design of high frequency resonators and comb-drives for communication and sensing applications. Chemically modified surfaces and structures of diamond and DLC films have been designed to serve as sensor materials for sensing traces of gases, as well as for detecting bio-molecules in biological research and disease diagnosis.

Extending these studies, implementing carbon nanotubes and carbon fiber which carry multiple superior and unique material properties into MEMS devices can greatly

widen the range of carbon-MEMS, when the appropriate fabrication techniques are established.

1.4 Research Objectives

As illustrated in Figure 1.5, this PhD dissertation aims to effectively incorporate the unique and superior properties of carbon materials both as key functional components and substrates into MEMS systems, which can potentially enable new types of carbon-MEMS devices. Among all carbon materials, carbon nanotubes and carbon fiber, as discussed in 1.2 and 1.3, possesses extremely favorable characteristics and are great candidates for the aforementioned objectives.

Carbon nanotubes carry extremely high Young`s Modulus (E_y=1TPa), superior electrical properties (current density of 4×10^9 A/cm^2), exceptional piezoresistivity (G=2900), and unique spatial format (very high aspect ratio hollow cylinder with nano-diameter and micro/macro-length), among other properties. If properly utilized, all these merits can give rise to a variety of new types of carbon nanotube based micro- and nano-electronics that may greatly fulfill the need for the next generation of faster, smaller and better devices. However, before these functions can be fully explored and realized in a nano/microsystem, one substantial issue to cope with is how to incorporate CNTs into these systems in an effective and controllable fashion. As discussed in 1.1.5, the challenges associated with CNTs integration include their very poor dispersibility in solvents, lack of melting/sublimation point, and unfavorable rheology with regard to mixing and processing highly viscous, CNT-loaded polymer solutions. These issues hinder the practical progress of CNTs from being studied in a lab scale as well as real applications in the industrial level.

Therefore, the first objective of this thesis is to develop an appropriate fabrication technology that achieves controlled integration of CNT into Microsystems. Since MEMS technology has demonstrated strong capability in developing silicon and metal based microsystems, we will take advantage of this mature technique to facilitate the micropatterning and manipulation of the CNTs. Specific to this body of work, a MEMS-assisted electrophoretic deposition (EPD) technique will be developed to achieve controlled CNT patterning on both rigid and flexible micro-/macro-systems at room temperature with relative high throughput. The controllability of the process will also been evaluated in Chapter 2.

Upon clearing the hurdles of the CNT pattering, the second objective is to implement CNT as the primary functional component in electronics. The exceptional and unique piezoresistive, structural and electrical characteristic of a specially constructed CNT-elastomer composite will be incorporated, investigated and validated in two types of elastic electronics, force/strain microsensors (Chapter 3) and electrets based energy harvesters (Chapter 4). The resultant nanocomposite combines the excellent piezoresistive and charge storage properties of the CNTs with the ductility of the polymer simultaneously, in an effort to develop conformal, low cost and mechanically elastic/flexible electronics with tunable properties. The performance of CNT based-MEMS devices will be characterized and evaluated. The optimization of the material properties will be studied as well.

In addition to utilizing CNTs as the functional components in MEMS systems, the third objective of this dissertation is to explore the possibility of extending the application of carbon fiber to serve as a substrate/building block for MEMS devices. Though carbon

fiber has been exploited as a flexible spring in a MEMS scanning micro-mirror array, its full potential in advanced electronics has yet not been fully tapped. The excellent mechanical strength (E_y=530GPa), fiber-shape geometry with micro-scale diameter and macro-scale length, superior thermal stability (up to 1500 °C), good electrical conductivity (10^6 S/m) and roll-to-roll processability of the CF suggest that it can serve as both a building block and the electrode in constructing next generation of hairlike silicon solar cells for wearable or stealth devices. Chapter 5 will discuss the design, fabrication and characterization of this fiber solar cell in detail. The study may open up new applications for both the CF and the solar cell.

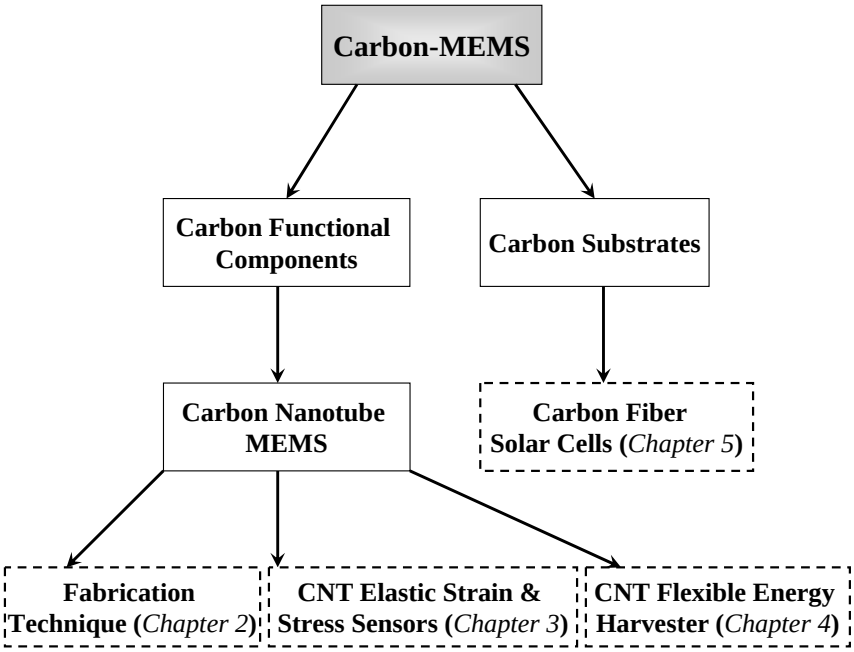

Figure 1.5: A schematic outline of the major objectives presented in this dissertation.

1.5 References

(1) *Chemistry Operations, "Carbon", Los Alamos National Laboratory* **2003**, December 15.

(2) Charitidis, C. A. *International Journal of Refractory Metals and Hard Materials* **2010**, *28*, 51.

(3) Burchell, T. D. *Carbon Materials For Advanced Technologies*; ELSEVIER, 1999.

(4) Dyment, J. C.; D'Asaro, L. A. *Electron Devices, IEEE Transactions on* **1967**, *14*, 630.

(5) Shalamov, V. T. *Graphite*; W. W. Norton & Company; 1st edition, 1981.

(6) Gerhard, K.; Alan B, *Carbon Black Manufacturing and Applications*; CRC 2007.

(7) Wang, X.; Li, Q.; Xie, J.; Jin, Z.; Wang, J.; Li, Y.; Jiang, K.; Fan, S. *Nano Letters* **2009**, *9*, 3137.

(8) Harris, P. J. F. *Carbon Nanotube Science: Synthesis, Properties and Applications*: Cambridge University Press; 1st edition 2009.

(9) Hill, F. A., T.F. Havel, D.; Lashmore, M. Schauer and C. Livermore In *Proceedings of the 10th International Workshop on Micro and Nanotechnology for Power Generation and Energy Conversion Applications, PowerMEMS 2010* Leuven, Belgium, December 2010.

(10) Manocha, L. M.; Pande, R. *Journal of Nanoscience and Nanotechnology* **2010**, *10*, 3822.

(11) Pugno, N. M. *Journal of Physics-Condensed Matter* **2006**, *18*, S1971.

(12) Nakayama, Y. *Japanese Journal of Applied Physics* **2008**, *47*, 8149.

(13) Lee, J.; Liao, A.; Pop, E.; King, W. P. *Nano Letters* **2009**, *9*, 1356.

(14) Yu, M. F.; Lourie, O.; Dyer, M. J.; Moloni, K.; Kelly, T. F.; Ruoff, R. S. *Science* **2000**, *287*, 637.

(15) Demczyk, B. G.; Wang, Y. M.; Cumings, J.; Hetman, M.; Han, W.; Zettl, A.; Ritchie, R. O. *Materials Science and Engineering a-Structural Materials Properties Microstructure and Processing* **2002**, *334*, 173.

(16) Wagner, H. D. In *Encyclopedia of Polymer Science and Technology*; John Wiley & Sons, 2002.

(17) Ruoff, R. S.; Tersoff, J.; Lorents, D. C.; Subramoney, S.; Chan, B. *Nature* **1993**, *364*, 514.

(18) Palaci, I.; Fedrigo, S.; Brune, H.; Klinke, C.; Chen, M.; Riedo, E. *Physical Review Letters* **2005**, *94*.

(19) Baughman, R. H.; Zakhidov, A. A.; de Heer, W. A. *Science* **2002**, *297*, 787.

(20) Lu, X.; Chen, Z. *Chemical Reviews* **2005**, *105*, 3643.

(21) Avouris, P.; Martel, R. *Mrs Bulletin* **2010**, *35*, 306.

(22) Regan, B. C.; Aloni, S.; Jensen, K.; Ritchie, R. O.; Zettl, A. *Nano Letters* **2005**, *5*, 1730.

(23) Zanello, L. P.; Zhao, B.; Hu, H.; Haddon, R. C. *Nano Letters* **2006**, *6*, 562.

(24) Xu, W. J.; Chen, H. Z.; Shi, M. M.; Huang, Y. G.; Wang, M. *Nanotechnology* **2006**, *17*, 728.

(25) Cao, L.; Chen, H. Z.; Zhou, H. B.; Zhu, L.; Sun, J. Z.; Zhang, X. B.; Xu, J. M.; Wang, M. *Advanced Materials* **2003**, *15*, 909.

(26) Stampfer, C.; Helbling, T.; Obergfell, D.; Schöberle, B.; Tripp, M. K.; Jungen, A.; Roth, S.; Bright, V. M.; Hierold, C. *Nano Letters* **2006**, *6*, 233.

(27) O'Connell., M. J. *Carbon Nanotubes. Properties and Applications*; CRC Press, 2006.

(28) Stampfer, C.; Jungen, A.; Linderman, R.; Obergfell, D.; Roth, S.; Hierold, C. *Nano Letters* **2006**, *6*, 1449.

(29) Liu, S.; Shen, Q.; Cao, Y.; Gan, L.; Wang, Z. X.; Steigerwald, M. L.; Guo, X. F. *Coordination Chemistry Reviews* **2010**, *254*, 1101.

(30) Dubnikova, I.; Kuvardina, E.; Krasheninnikov, V.; Lomakin, S.; Tchmutin, I.; Kuznetsov, S. *Journal of Applied Polymer Science* **2010**, *117*, 259.

(31) Baibarac, M.; Gomez-Romero, P. *Journal of Nanoscience and Nanotechnology* **2006**, *6*, 289.

(32) Kim, H. M.; Kim, K.; Lee, S. J.; Joo, J.; Yoon, H. S.; Cho, S. J.; Lyu, S. C.; Lee, C. J. *Current Applied Physics* **2004**, *4*, 577.

(33) Bhattacharya, M.; Wutticharoenmongkol-Thitiwongsawet, P.; Hamamoto, D. T.; Lee, D.; Cui, T. H.; Prasad, H. S.; Ahmad, M. *Journal of Biomedical Materials Research Part A* **2011**, *96A*, 75.

(34) Ajayan, P. M.; Stephan, O.; Colliex, C.; Trauth, D. *Science* **1994**, *265*, 1212.

(35) Spitalsky, Z.; Tasis, D.; Papagelis, K.; Galiotis, C. *Progress in Polymer Science* **2010**, *35*, 357.

(36) Dalton, A. B.; Collins, S.; Munoz, E.; Razal, J. M.; Ebron, V. H.; Ferraris, J. P.; Coleman, J. N.; Kim, B. G.; Baughman, R. H. *Nature* **2003**, *423*, 703.

(37) Miaudet, P.; Badaire, S.; Maugey, M.; Derré, A.; Pichot, V.; Launois, P.; Poulin, P.; Zakri, C. *Nano Letters* **2005**, *5*, 2212.

(38) Thostenson, E. T.; Ren, Z.; Chou, T.-W. *Composites Science and Technology* **2001**, *61*, 1899.

(39) Bhadeshia, H. *Materials Science and Technology* **2005**, *21*, 1293.

(40) Morgan, P. *Carbon Fibers and Their Composites (Materials Engineering)*; CRC Press; 1 edition 2005.

(41) Donnet *Carbon Fibers, Third Edition,*; CRC Press; 1st edition, 1998.

(42) Zhao, Z. F.; Gou, J. *Science and Technology of Advanced Materials* **2009**, *10*.

(43) Wang, X.-L.; Oh, I.-K.; Kim, J.-B. *Composites Science and Technology* **2009**, *69*, 2098.

(44) www.mezmeriz.com last retrieved on March 25, 2011

(45) Unalan, H. E.; Wei, D.; Suzuki, K.; Dalal, S.; Hiralal, P.; Matsumoto, H.; Imaizumi, S.; Minagawa, M.; Tanioka, A.; Flewitt, A. J.; Milne, W. I.; Amaratunga, G. A. J. *Applied Physics Letters* **2008**, *93*.

(46) Kovacs, G. T. A. *Micromachined Transducers Sourcebook*; McGraw-Hill: NewYork, NY 1998.

(47) J. Lee, K. N., H. Hunter, J. Berg, T. Wright, C. Courcimault, N.Naik, M. G. Allen, O. Brand, A. Glezer, W. King In *Proceeding of 2005 ASME IMECE* Orlando, FL, Nov. 5-11, 2005, Paper number: IMECE2005-81698.

(48) Rajaraman, S.; Zhao, Y. Z.; Wu, X.S.; Kim, S.H; Allen M.G. In *in Tech. Dig. International Symposium on Flexible Automation (ISFA 2008)* Atlanta, USA, June 2008.

(49) Park, J.H.;Yong, Y.-K.; Choi, S. O.; Prausnitz, M.R.;Allen, M.G. *IEEE Transactions on Biomedical Engineering* **2007**, *54*, 903.

(50) Gardner, J. W. *Microsensors: Principles and Applications*; John Wiley & Sons: West Sussex, England 1994.

(51) Gardner, J. W.; Varadan, V.K.; Awadelkarim, O.O *Microsensors, Mems and Smart Devices*; John Wiley & Sons: West Sussex, England, 2001.

(52) *MEMS Lab., Department of Mechanical Engineering, College of Engineering, SDSU, San Diego, CA 92182.*

(53) Madou, M. J., Lal, A., Schmidt, G., Song, *in: Electrochemical Society Proceedings* **1997**, *97-19*, 61.

(54) Lee, J. A.; Lee, S.; Lee, K. C.; Il Park, S.; Lee, S. S. *Journal of Micromechanics and Microengineering* **2008**, *18*.

(55) Yoon, Y. K.; Park, J. H.; Allen, M. G. *Journal of Microelectromechanical Systems* **2006**, *15*, 1121.

(56) Madou, M. J.; Zaouk, R.; Wang, C.; Park, B. Y. *ECS Transactions* **2006**, *1*, 1.

(57) Wang, C. T., Lili; Jia, Guangyao; Kassegne, Sam; Zoval, Jim V.; Madou, Marc J. *MEMS, MOEMS, and Micromachining, Proceedings of the SPIE* **2004**, *5455*, 295.

(58) Peiner, E.; Tibrewala, A.; Bandorf, R.; Luthje, H.; Doering, L.; Limmer, W. *Journal of Micromechanics and Microengineering* **2007**, *17*, S83.

(59) Luo, J. K.; Fu, Y. Q.; Le, H. R.; Williams, J. A.; Spearing, S. M.; Milne, W. I. *Journal of Micromechanics and Microengineering* **2007**, *17*, S147.

(60) Schueller, O. J. A.; Brittain, S. T.; Marzolin, C.; Whitesides, G. M. *Chemistry of Materials* **1997**, *9*, 1399.

CHAPTER 2

MICRO-PATTERNING/MANIPULATION OF CARBON NANOTUBES

2.1 Background and Motivation

As discussed previously in Chapter 1, excitement has surrounded the carbon nanotube since its discovery in 1991.This excitement stems from its superior and unique properties which enable a wide range of applications in molecular electronics, microsensors, solar cells, field emission devices, bio-coatings, and so on[1,2,3,4,5,6]. This high aspect ratio nanomaterial carries interesting piezoresistive, electrical, mechanical, structural, and physiochemical properties that make it attractive to serve as a key constituent in microsystems[7,8,9]. Massive efforts have therefore been made to incorporate this versatile material into microelectronics[1]. However, despite of two decades of intensive study, very limited practical progress has been achieved to bring this material into real applications. Several issues regarding the controlled fabrication of these types of devices need to be addressed in order to utilize CNTs in real applications. First, the carbon nanotube is a nano-sized material with high surface area that can easily aggregate into bundles in order to reduce its overall surface energy. Hence, it has very poor dispersibility in solvents and foreign matrices which imposes a challenge on the solvent-based dispersion and casting processes. Moreover, CNTs cannot be directly vapor-deposited into device systems in a very controllable way compared with conventional metal or dielectric materials. Both facts hinder their widespread use and

progress, particularly in nano/microelectronics where precise patterning and control over the material morphology/geometry are required. As a result, an effective fabrication technique needs to be developed to tackle the problem of manipulation of the nanotubes, individually or collectively, in order to generate a particular arrangement of the nanotubes for a specific application.

Multiple approaches so far have been considered with respect to this issue to accomplish the goal of CNT patterning and manipulation. In general, there are two pathways to achieve the localization: during CNT synthesis and post CNT synthesis. The former usually involves pre-patterning of catalyst nanoparticles on the desired substrates, followed by a high temperature chemical vapor growth reaction[10]. This approach directly deposits vertically aligned nanotubes in patterned locations (Figure 2.1a), yet the high processing temperature (>400°C), inability to fully refine the CNTs after the growth, and difficulty to generate patterns over a large scale are potential limitations. The latter (post-CNT-synthesis patterning) overcomes all of these limitations, at the expense of extra processing steps. The second approach is potentially preferable in microsystems due to low processing temperature and the possibility to utilize purified CNTs, as impurities can potentially deteriorate device performance. Terranova *et al.* reported the assembly of CNTs across a micro-gap between two electrodes through dielectrophoresis under an AC field. Low yield and lack of control over the mass are two deficiencies that need to be improved for this approach[11] (Figure 2.1b). An AFM tip has been utilized to place an individual carbon nanotube onto desired locations in nano-devices[12] (Figure 2.1c). Nevertheless the low throughput and time consumption limit its practical applications. Cui *et al.* have explored polymer assisted layer-by-layer (LBL) assembly to generate

CNT layers on microstructures[13], which is a room temperature and mass controllable process. Yet this approach involves slow and labor intensive LBL processing and impurities (polymers with counterions etc.) are introduced into CNT layers which may be detrimental to the performance of CNTs in a given application[14]. Inkjet printing of CNT solutions has becomes a popular approach recently to produce complicated CNTs patterns continuously on flexible substrates such as paper and plastic sheets over a large scale (Figure 2.1d). Homogenous carbon nanotube dispersion is an essential requirement for this approach to avoid the clogging issue. The resolution of the generated patterns is limited to over a hundred micrometers and the print needs to be repeated multiple times in order to achieve desirable conductivity due to the low starting concentration of the CNT solution[15,16]. Micro-contact printing has been demonstrated to be another effective way to generate CNT micropatterns (Figure 2.1e). This approach imitates the lithographic printing process, where CNTs are first dispersed in a diluted polymer (e.g. PDMS) solution and subsequently spun cast on a flat substrate. A PDMS template bearing protruding microstructures is then brought in contact with the CNT layer and eventually the CNTs in the contact areas are peeled off and remain with the PDMS mold. Upon pressing the PDMS mold on a substrate, the CNT patterns are further transferred onto another substrate when appropriate conditions are applied. The difficulties remaining for this method include the requirement for precise control of contact transfer steps and the rheology issue with regard to mixing CNTs with PDMS in the initial spin-casting process[17]. Photolithography is the most straightforward way to generate precise CNT patterns using dry etching. Nevertheless, forming a uniform CNT film with different thickness on a substrate by either spin casting or direct transfer from vacuum-infiltration

is a challenge to overcome, and the subsequent photolithography process potentially introduces impurities such as photoresist residues inside the CNT network[18,19].

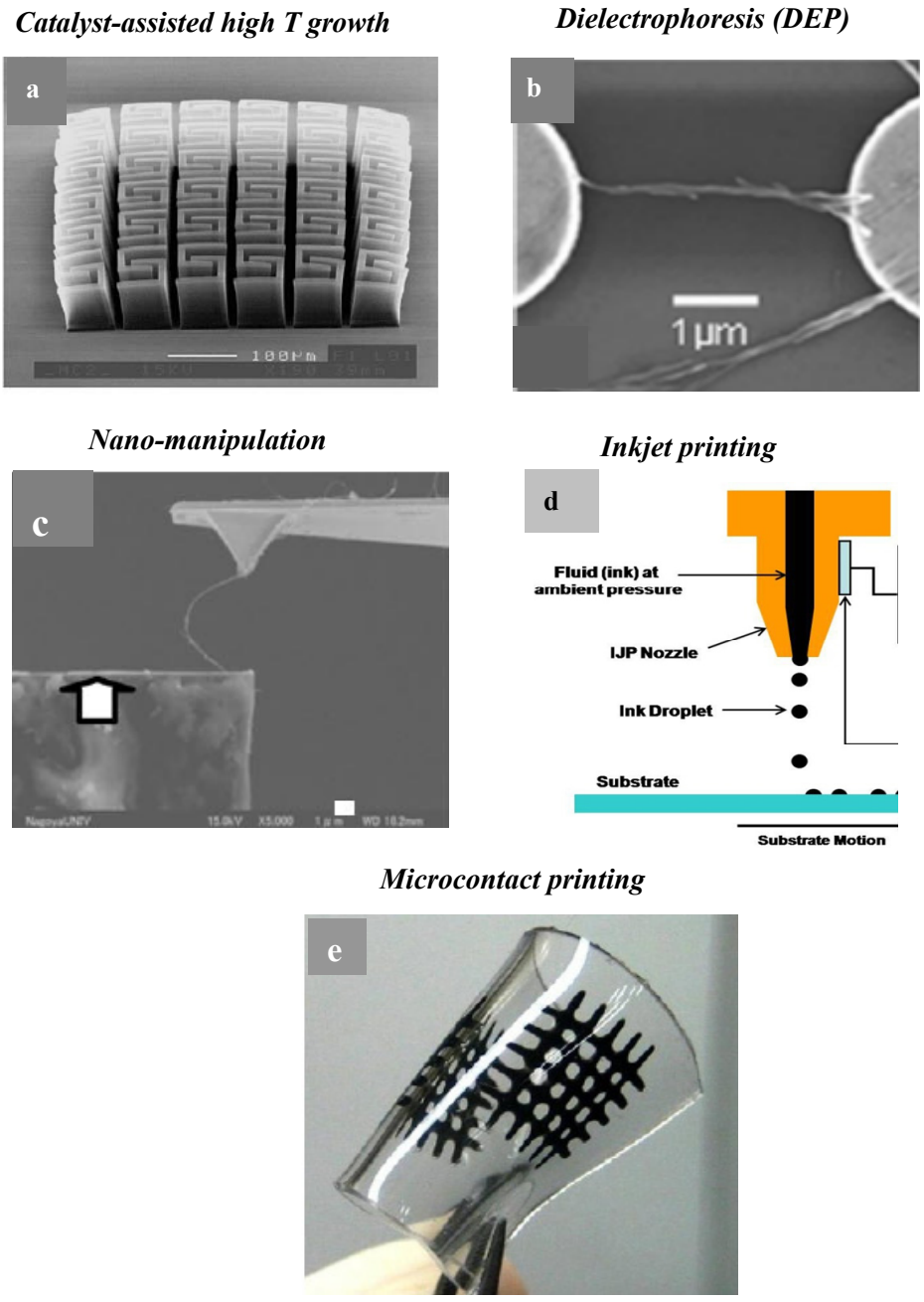

Figure 2.1: A variety of approaches for micropatterning/manipulation of CNTs.

In practical applications, purification of CNTs is critical for both reliability and reproducibility of the device performance on which they rely. Good control of the thickness and morphology of CNTs is also important for quantitatively studying their properties in micro-systems and optimizing their performance in resultant devices. Therefore in this chapter, we discuss the development of a high throughput, room temperature patterning process with good control over deposited mass, relatively high resolution, and the ability to achieve micropatterns of pristine CNTs over a large scale on both rigid and compliant substrates.

2.2 Micrpatterning/Manipulation of CNTs through MEMS-assisted Electrophoretic Deposition (EPD)

2.2.1 Introduction of EPD

Electrophoretic deposition, a technique in which electric fields are used to assist transportation of charged species in a liquid medium, has been demonstrated to be capable of uniformly depositing a wide variety of materials at room temperature (RT) with good control over deposited mass. This process has been widely used in generating coatings on metal components in industry for protection or multi-functional purposes. Those include automobile bodies and parts, electrical switch gear, appliances, metal furniture, beverage containers, fasteners, among many others[20]. In addition, EPD has also been utilized to produce customized microstructures such as functional gradients and laminates, through suspension control during processing[21]. More importantly, EPD can generate nanostructures which are very useful in the emerging nanotechnology fields[22].

Some key advantages which EPD can offer include[23]:

- Uniform and conformal deposition with controllable deposited mass

- High deposition rate with relatively high purity
- Deposition over complex shaped structures with good homogeneity
- Room temperature processing with high throughput over a large area
- Applicable to a wide range of materials (metals, ceramics, polymers, etc.)
- Easy control of the coating composition
- Automated process with very little human labor
- Efficient utilization of the coating materials
- Lower costs relative to other processes

When an electric field is applied across a liquid medium containing suspended charged particles, the particles migrate towards the corresponding electrode and precipitate/aggregate on it. The deposited mass for spherical particles, *M*, can be estimated by equation 2.1[23]:

$$M = \int_0^t \alpha A \mu E c dt \tag{2.1}$$

where α is the mass fraction of material deposited on a specific electrode, *A* is the total area of the energized electrode, μ is the particle mobility in a given solution, *E* is the applied electric field, *c* is the particle concentration in the dispersion, and *t* is the deposition duration. The deposited mass can be easily controlled by varying *E*, *c* and *t*.

CNTs under certain circumstances can be chemically modified to generate functional groups which allow the CNTs to carry either positive or negative charges when dispersed in an appropriate solvent[24]. Therefore they are suitable to be deposited by the EPD process. The ability of EPD to isolate, control and assemble nanoscale materials

into organized micro-/macro-scale morphologies/structures yields new and high-performance functional systems. The advantages offered by this bottom-up strategy meet almost every criterion of the specific goal for CNT manipulation in this study. Hence this approach has been chosen in this study to facilitate the micropatterning of CNTs in microsystems.

CNT deposition on un-patterned macro-scale electrodes has been successfully achieved[23]. With the hypothesis that the trajectory of a charged particle follows the electric field line, it is reasonable to assume that selective CNT deposition can be achieved if the electric field lines (or electrodes) are patterned, such as what has been demonstrated in the electroplating process. Since MEMS technology can easily generate suitably patterned microelectrodes in a variety of dimensions and geometries, this approach is combined with the EPD process to create selective assembly of CNTs over a large scale in a single step. To fully evaluate the proposed MEMS-assisted EPD process, CNT deposition on three common types of microstructures in microsystems fabricated by MEMS techniques was investigated and their suitability for CNT micropatterning was validated.

2.2.2 Fabrication Process

MWCNTs were purchased from Nanostructured & Amorphous Materials, Inc. with an outer diameter of 50-80nm, a length of 10-20 μm and a purity of 95%. Water was chosen as the liquid medium for CNT suspension in this study, partially due to the low electric field (<15V/cm) required for the deposition compared with organic solvents[23] (>30V/cm) and partially due to its low volatility and eco-friendly nature. The as-received CNTs contain 5% of un-desired impurities such as catalytic metal particles and

amorphous carbon. In addition, though the raw CNTs had been functionalized with 1-6wt% of carboxylic acid group (–COOH), they still tended to precipitate in water and had a very poor dispersion even after three hours of ultrasound sonication. To achieve a uniform deposition of CNTs through EPD, it is critical to ensure stable dispersion of CNTs in water[25,26]. To improve the purity and dispersibility of CNTs in water, MWCNTs were further acidified in a mixture of sulfuric acid and nitric acid (3:1 volume ratio) for 4 hours at room temperature with ultrasound sonication. The acid-treated CNTs were filtered through Teflon filter paper with a pore size of 1μm and subsequently rinsed with DI water and then air dried. The amount of impurities could be greatly reduced through the oxidation reaction[24]. Meanwhile, more carboxylic acid groups and oxygen-containing groups (SO_3^{2-} and NO_3^-) were introduced to the nanotubes through this acidification process. These acid groups will dissociate in water and form negative charges on CNTs, which not only enables the EPD process, but also improves the hydrophilicity of CNTs and provides electrostatic hindrance among CNTs which eventually helps to approach a stable and homogenous dispersion.

To evaluate the feasibility of the MEMS-assisted EPD process to implement CNTs into general microsystems, three types of microstructures being widely utilized in electronics (metal, Si and organic material) were fabricated on silicon substrates through MEMS fabrication techniques, as illustrated in Figure 2.2.

The first microstructure consists of interdigitated metal microelectrode arrays. The process started with deposition of a 1-μm-thick dielectric layer (SiNx, SiO2, SiC or parylene) through Plasma-enhanced chemical vapor deposition (PECVD) or Parylene coating on a silicon wafer. Afterwards, the gold patterns on the dielectric layer were

generated through two approaches. The first one was depositing a 500-nm-thick gold (Au) layer with a 50-nm-thick titanium (Ti) adhesion layer on top of the dielectric layer through electron-beam evaporation and subsequently patterning the Au/Ti layer through standard photolithography and chemical wet etching processes. The other was first patterning the photoresist on top of the dielectric layer through standard photolithography, followed by electron-beam evaporation of a 500-nm-thick gold layer onto the photoresist patterns and ultimately realizing the gold pattern through a lift-off process that dissolved the photoresist structure (Figure 2.2, I). The comparison of the two patterning processes of the gold layer will be discussed in section 2.2.3.6.

The second microstructure is composed of silicon micro-channels. A 1-μm-thick silicon nitride layer was first deposited on top of a silicon wafer. A 10-μm thick photoresist layer was then spin-cast and patterned on the silicon nitride layer through standard photolithography, serving as the mask for the subsequent dry etching of the SiN_x and the silicon. After generation of 30-μm-deep silicon channels using Plasma-Therm inductively coupled plasma (PT-ICP), a 500-nm-thick gold layer was deposited on the silicon wafer through Electron beam evaporation and followed by the lift-off process. Upon removal of the photoresist, the gold layer remained at the bottom of the channels, serving as the electrodes for the subsequent EPD process (Figure 2.2, II).

The third microstructure was fabricated from SU-8 epoxy (photoresist). In this configuration, a 500-nm-thickness gold layer was first deposited on a silicon wafer through an E-beam evaporator, on which the SU-8 was further spin-cast. Patterns such as a micro-circular well array with dimension of 200-μm in diameter, 40-μm in depth and 200-μm in spacing and microelectrode array were generated in the SU-8 layer through a

photolithography process. An oxygen plasma treatment using reactive ion etching (RIE) was performed to remove potential residues of the photoresist at the bottom of the microwells/trenches (Figure 2.2, III).

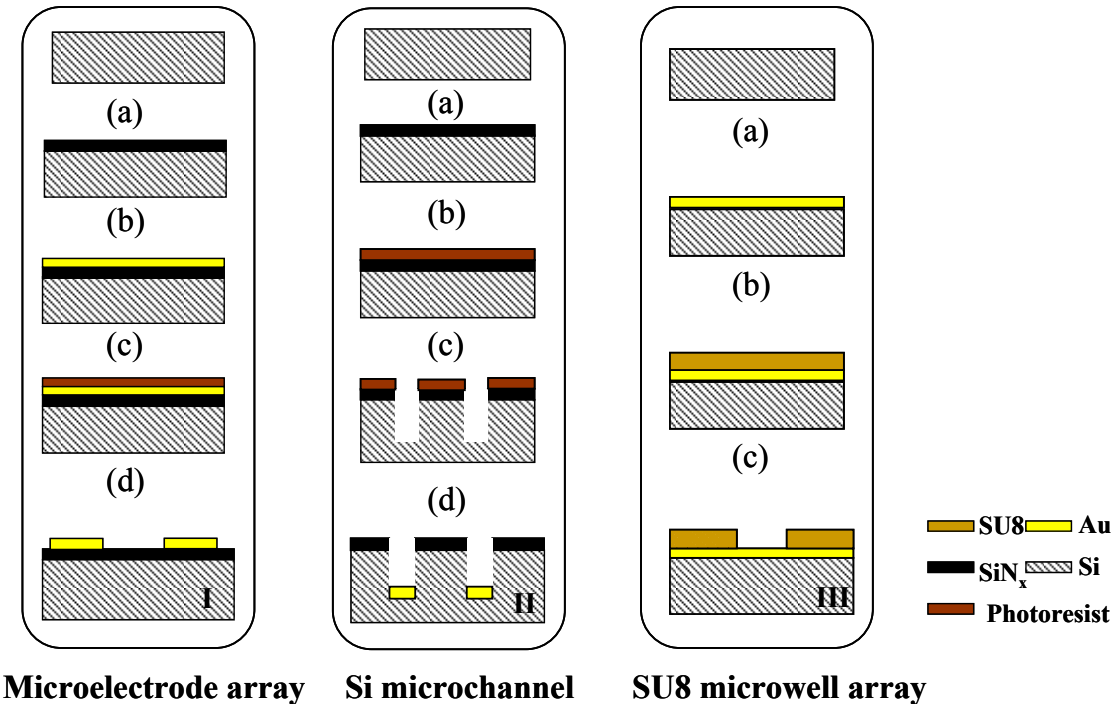

Figure 2.2: Fabrication process flow of three different microstructures utilized as the templates for selective CNT patterning: I, interdigitated gold microelectrode array; II, silicon micro-channel array, and III, photoresist microwell/trench array.

MWCNTs-COOH prepared as discussed previously were then dispersed in deionized water at various concentrations ranging from 0.1g/L to 0.5g/L and sonicated for 2 hours to ensure a homogenous suspension. No surfactant and additives were added into the solution. Later the microstructure-bearing substrates and a copper counter electrode were immersed directly into 50mL of CNT dispersion at room temperature and electrically energized with an external voltage source, with the copper serving as the

cathode and substrate serving as the anode. As illustrated in Figure 2.3, the negatively-charged CNTs-COO^- will be electrically directed in water towards patterned electrode surfaces on the microstructures (anode) under the influence of a constant electric field applied across two electrodes for various durations. As indicated in Equation 2.1, for a given microstructure/dispersion combination and with a high volume of CNTs solution, the parameters A, μ and α can be considered as constants. The electric field, deposition time and the solution concentration determine the thickness of the final CNTs layer. Their relationship was studied in order to accomplish a controlled deposition of the CNTs.

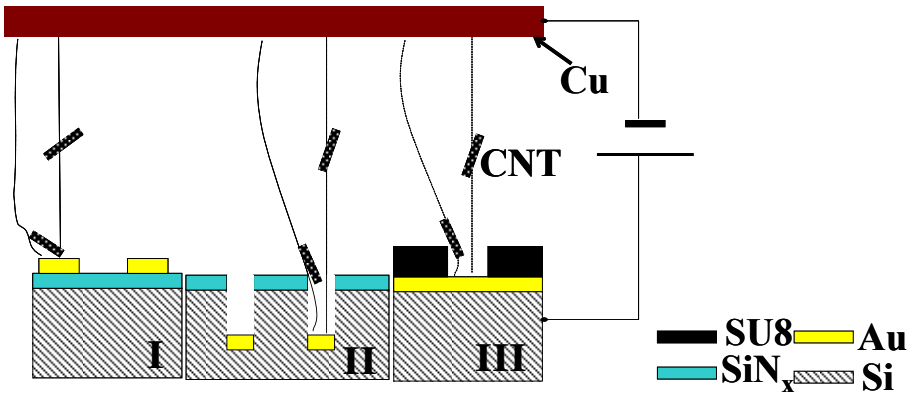

Figure 2.3: Process flow for electrophoresis of CNTs on different microstructures: I) interdigitated gold microelectrode array; II) silicon micro-channel array; and III) SU-8 microwell array.

The produced CNT micropatterns were further transferred to a polydimethylsiloxane (PDMS) matrix by pouring liquid PDMS oligomer (Sylgard® 184, Dow Corning) into the CNT micropatterns, degassing for 30min, curing it at 120 ºC for 40min, followed by demolding the PDMS (Figure 2.4). Upon demolding, the CNT layer

was transferred to the PDMS film. Complex CNT micropatterns can be embedded in the uppermost layer of the molded polymer film, while simultaneously maintaining their original geometric layout, eliminating the issues associated with rheology and dispersion of CNTs in the polymer. As a result, the combination of MEMS-assisted EPD technique with the micromolding process may be an effictive way to achieve fabrication of flexible CNT-based microelectronics.

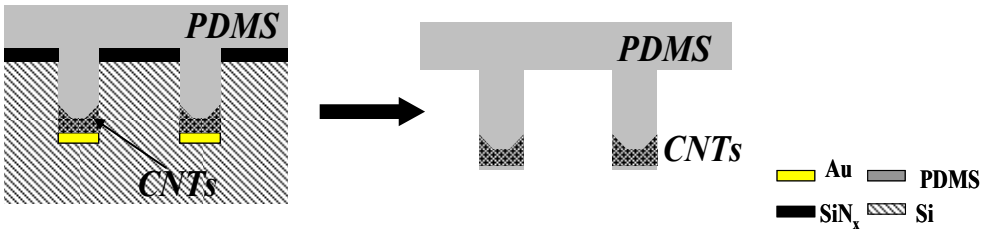

Figure 2.4: Scheme of transfer micromolding process of CNT patterns.

The morphology of the CNT patterns was characterized by Zeiss Scanning Electron Microscopy (SEM) Ultra60. Atomic force microscopy (AFM, MultiMode and Dimension 3000, Veeco Metrology) was used for topography and surface roughness study of the SU-8 microstructures before and after oxygen plasma treatment. Static contact angle measurements were performed thourgh a sessile drop method for the surface hydrophobicity evaluation. WVASE32 Woollam Ellipsometer and Tencor P15 Profilometer were utilized to investigate the thickness of the deposited CNTs layer on the microelectrodes.

2.2.3 Results and Discussion

2.2.3.1 Assembled CNT Micropatterns on Microstructures

The micropatterns of CNTs generated by EPD are shown in Figure 2.5. As expected, when no substantial topography was present in the microstructures, the resultant CNTs typically assembled only on conductive metal areas to which electric fields had been applied. The negatively charged CNTs were neutralized and aggregated when reaching those surfaces. Figure 2.5a and Figure 2.6a confirmed that CNTs did not assemble on micropatterns lacking an applied electric field. Similarly, no deposition was observed on the dielectric material region (SiN_x) adjacent to and between the metal areas as shown in the enlarged image (Figure 2.5b). As observed in Figure 2.5b, the CNTs deposited loosely over the microelectrode surface after 1min deposition under an electric field of 15V/cm and a dispersion concentration of 0.1g/L, with a thickness of approximately 133nm (Figure 2.6b). This thickness corresponded to approximately two to three layers of CNTs since the diameter of the CNTs is approximately 50~80 nm. A 6-μm-thick CNT layer was also produced in a single step as shown in Figure 2.6c after 5min deposition under an electric field of 30V/cm in a 0.3g/l solution. Thicker films up to tens of micrometers can be potentially obtained by applying several sequential depositions on the same substrate.

In addition to the loose assembly, CNTs were able to coalesce into thick blocks with very high packing density inside silicon micro-channels as shown in Figure 2.5c and 2.5d, under the extended experimental duration of 3min at an electric field of 15V/cm. SEM imaging revealed that the deposited layer was thicker at the edge of the microchannel and thinner in the middle, which could be partially due to the non-uniformity of the electric field distribution inside the micro-sized channels. Numerical analysis on similar structures has shown that the field strength is three

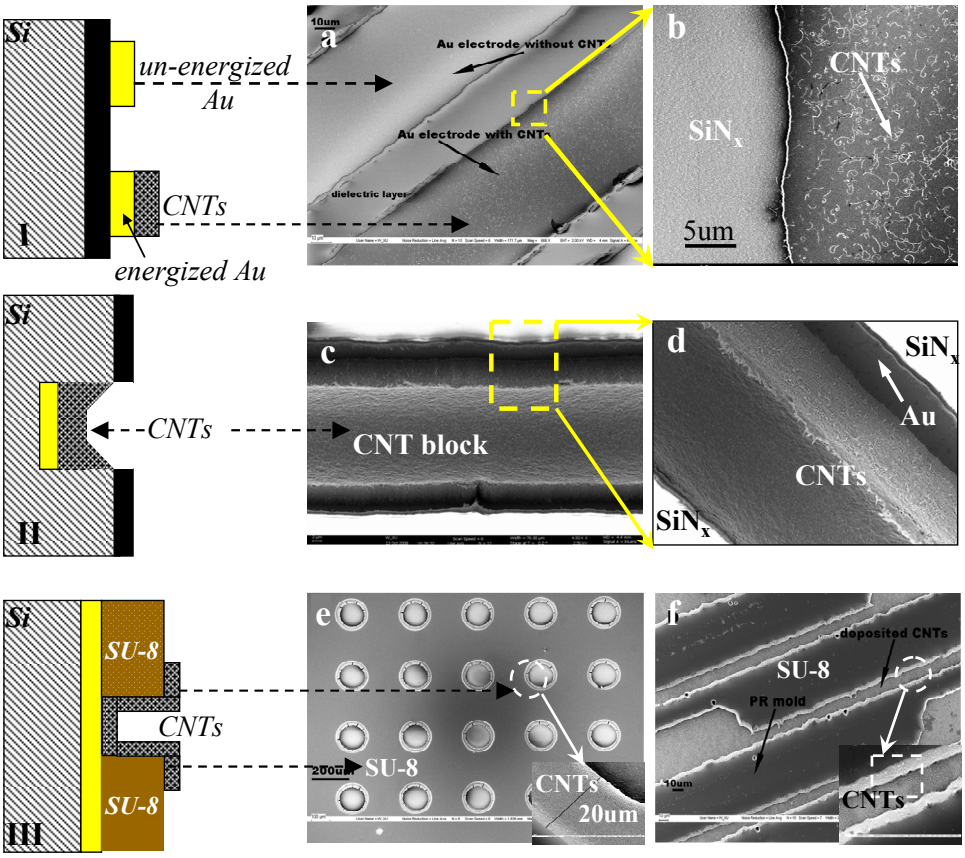

Figure 2.5: CNT micropattens achieved through EPD on: I) interdigitated gold microelectrode array; II) silicon micro-channel array; and III) SU-8 microwell array.

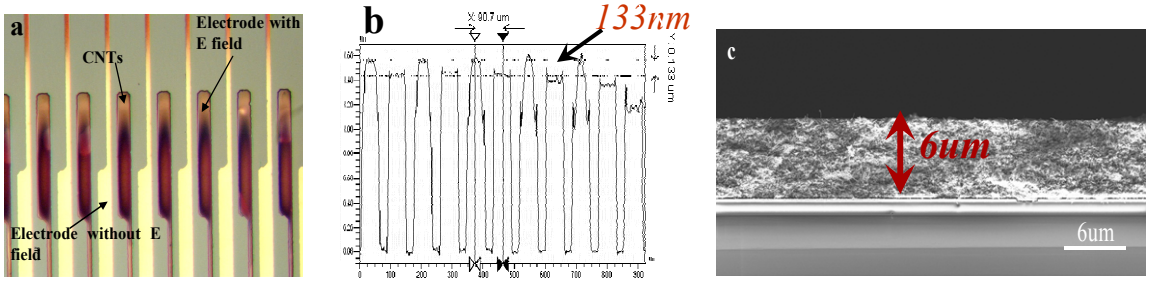

Figure 2.6: (a) optical image of CNT patterns on microelectrode array; (b) ellipsometry measurement of the layer thickness of the CNT pattern in (a), and (c) SEM image of CNT layer with a thickness of 6µm.

times higher at the microelectrode edge than that in the center due to field enhancement[27]. As a result, CNTs are deposited faster at the edge than in the middle of the channel.

In the case of the microstructures composed of photoresist, CNTs assembled conformally around the SU-8 microwell inner surface, and in addition generated a 20μm wide circular belt framing the well opening, thereby creating a continuous 3-D coating in each isolated microwell (Figure 2.5e). Similar assembly behavior was further observed in rectangular microchannels fabricated from SU-8 as shown in Figure 2.5f, where conformal assembly on the channel inner surface and a 5-10μm wide rectangular CNTs belt framing the channel were generated. These observations indicate that under these conditions, the deposition of CNTs is in accordance with the conformal coating nature of the EPD process[28].

The information obtained from Figure 2.5 and 2.6 confirms the assumption made in section 2.2, that is, the trajectory of CNT particles can be controlled and localized deposition can be achieved by patterning the electric field lines. It also demonstrated the feasibility of the proposed MEMS assisted EPD technique in generating selective deposition of CNTs in most types of microstructures in microelectronics (silicon, metal and polymer). The layer thickness of CNTs produced in this way can be readily controlled by the deposition time (t), concentration of the dispersion (c), and the applied electric field (E). Depending on the feature size of the microstructures, the combination of these three parameters need to be adjusted in order to approach a uniform and localized deposition. To achieve micro-scale selective deposition of CNTs, it was observed through the experiments that low concentration and low electric field were preferred. It was experimentally found that with a feature size of less than 200μm, a

concentration of less than 0.2 g/l, an *E* of less than 20 V/cm and a *t* of less than 3min were preferred. For the structures with a feature size larger than 200μm, a *c* of up to 0.5g/l and an *E* of up to 30V/cm could lead to a faster and more uniform assembly. These observations may be due to the different deposition rate of the CNTs under the different experimental conditions, nevertheless the exact reason is not yet to be concluded.

2.2.3.2 Assembled Micropatterns of CNTs in Flexible Systems

The images in Figure 2.7 show that a variety of CNT patterns such as micro-springs, micro coils and micro-pads ranging from micro to macrometer scale were achieved on both elastic (PDMS) and polymeric (polyolefin) substrates. The materials bearing the CNT patterns exhibit both excellent flexibility and elasticity, and can be easily wrapped around a cylindrical object as shown in Figure 2.7b or be bent/stretched as shown in Figure 2.7c. These multifunctional CNT-based polymeric composite structures have promising applications in physical strain/stress sensors[19], artificial muscles and skins[29],

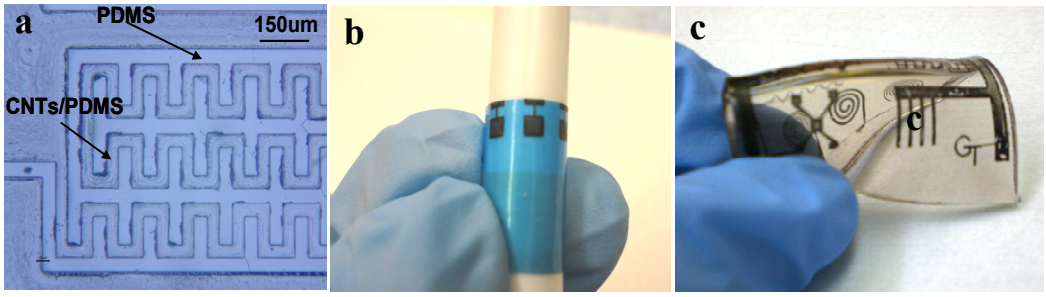

Figure 2.7: (a) optical image of CNT microspring patterns on PDMS, (b) digital image of CNT square patterns on a polyolefin film, and (c) digital image of CNT patterns on a PDMS substrate.

field effect transistors[30], field-electron emitters[31], organic light emitting diodes[32], energy textiles[33] and so on[34].

2.2.3.3 CNT Layer Thickness

Equation 2.1 describes an approximate relationship between the deposited mass and the parameters of EPD process for spherical particles. Such correlation for high aspect ratio cylindrical particles such as CNTs however has not yet been fully established. As thickness control is critical for CNT integration into microsystems in practical application, it is necessary to investigate the relationship of the CNT layer thickness as a function of process parameters. In this study, a fixed electrode material (gold), large volume of the solution, fixed total microelectrode area, and constant CNT concentration were chosen to achieve a constant α , μ , A and c, respectively in the experiment. Empirical relations of the deposited thickness (d) with applied electric field (E) under constant deposition time, as well as with deposition time (t) under constant E, were studied separately. For spherical particles, equation 2.1 can be rewritten as:

$$d = \frac{M}{\rho A} = (\alpha \mu c)\frac{E \cdot t}{\rho} \tag{2.2}$$

where ρ is the mass density of the deposited CNT layer, and other symbols are as defined previously. In the initial deposition stage, ρ will increase with the electric field or time, so d may not increase linearly with E or t. At a certain point when ρ approaches a constant, d then is likely to exhibit a linear increase with E or t.

The thickness study for CNT deposition was conducted on an array of planar gold

electrodes with a dimension of 1mm×1mm patterned on top of a silicon nitride-bearing silicon wafer. The fabrication process is the same with that of the interdigited microelectrode array described in section 2.2.2. The silicon nitride here serves as electrical insulation layer to facilitate the CNT patterning. As shown in Figure 2.8, though the precise equation has not yet been established for the deposition mass of CNT in an EPD process due to the complexity of the system, the deposited CNT layer thickness exhibited a monotonic increase with the increase of both the deposition time and electric field through the current experiments. The data obtained from this study shed some light on the deposition rate and thickness range achieved by the selected process parameters. The information provided useful guidance for the fabrication of microsensors based on pattern PDMS/CNTs nanocomposite with different initial resistance in Chapter 3, which facilitated the study of the resistance effects on the device sensitivity.

2.2.3.4 Surface Morphology of the Assembled CNTs

Surface morphology of the assembled CNT layer generated from different deposition duration was revealed by SEM imaging shown in Figure 2.9. A 133 nm thick layer with sparsely distributed CNTs has already been demonstrated in Figure 2.5b. Moreover, under the constant electric field of 20V/cm and concentration of 0.3 g/L, CNTs formed a thin layer with micro-sized pores and thickness of around 600 nm after 1min deposition, as shown in Figure 2.9a. These micro-sized pores were likely formed during the evolution of oxygen gas bubbles associated with the electrolysis of water on the anode surface since it occurs under the potential of 1.23V. When the deposition time increased to 2 min, the pore size in the CNT network decreased and a more uniform layer was observed (Figure 2.9b). As the deposition time continued to increase, the CNTs

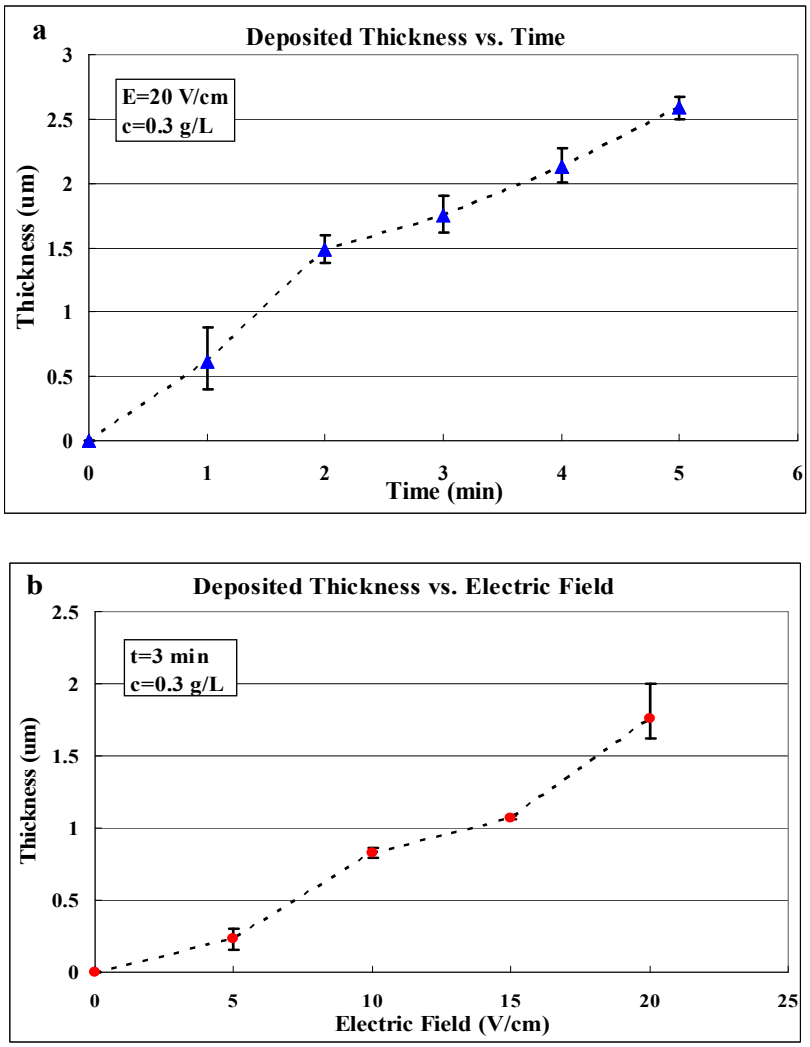

Figure 2.8: CNT layer thickness as a function of: (a) time under the constant *E* and *c*, and (b) electric field under the constant *c* and *t*. Error bars show the deviation of the thickness.

aggregated into a thicker and denser interpenetrating network. The porosity of the CNT film kept decreasing dramatically from micro-size to nano-size, as observed in Figure 2.9c-2.9e. Morphology of the CNT network plays an important role in the resistivity and the physical entanglement of the CNT film, which greatly affect the piezoresistivity of the CNT film which will be demonstrated in Chapter 3. The observations here indicate

that the MEMS-assisted EPD patterning technique may be capable of tailoring the porosity of the generated CNT layer, which partially determines the sensitivity of resultant strain/force sensors based on CNT network.

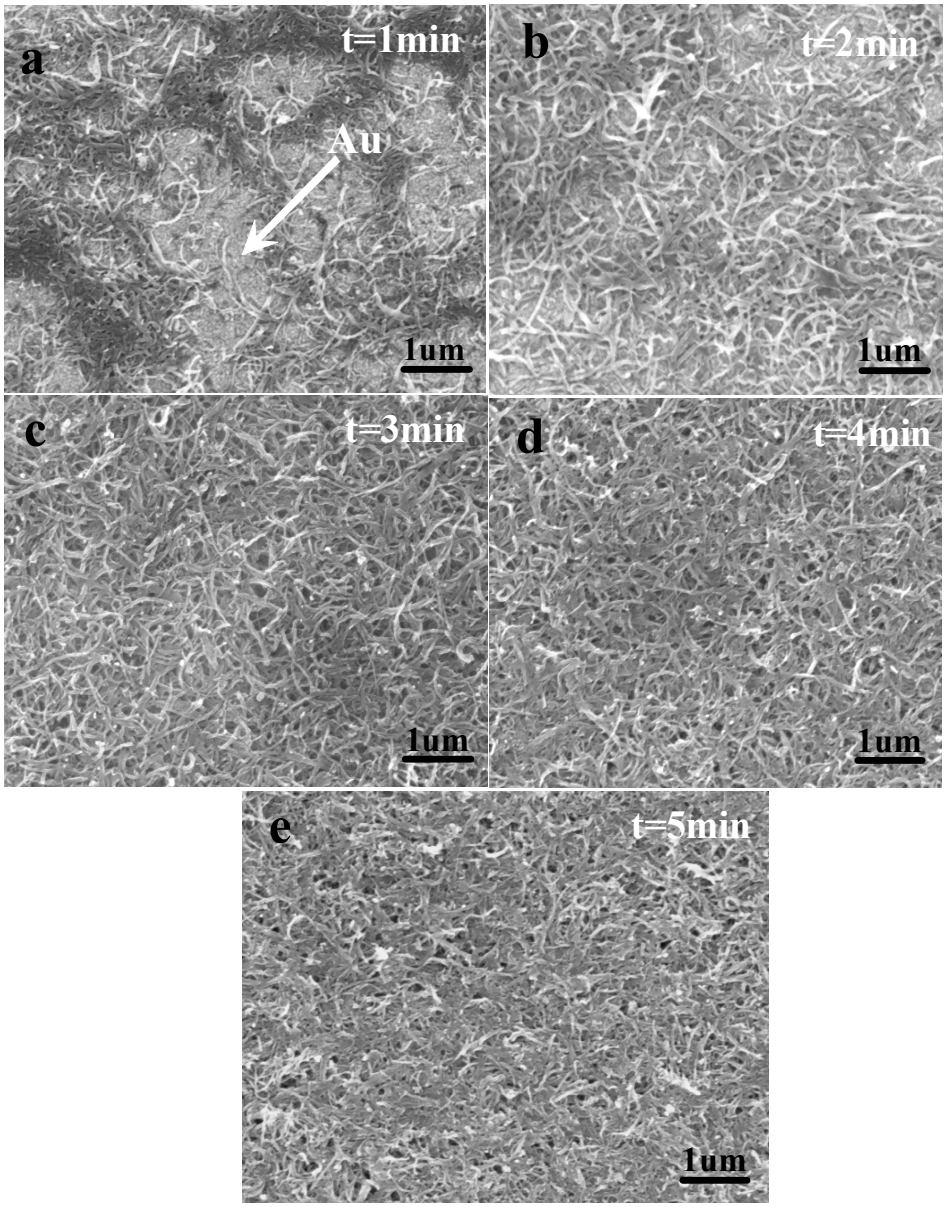

Figure 2.9: SEM image of surface morphology of EPD deposited CNT film with a deposition time of (a) 1min, (b) 2min, (c) 3min, (d) 4min and (e) 5min, under a constant electric field of 20V/cm and CNT concentration of 0.3 g/L.

2.2.3.5 Local Alignment of CNTs

CNT films produced from EPD under relatively low electric field (<50V/cm) generally exhibit an isotropic appearance. However, under sufficiently high electric strength[35] (>100V/cm) or magnetic fields[36], they are able to align perpendicularly to the electrode substrate (i.e., parallel to the external field lines). In addition, a well-dispersed CNT suspension is known to generate dense films with a certain degree of local alignment on conductive surfaces, which has been attributed to the drying of the gel-like material from the initial deposition[37]. In the present study, similar local alignment of the CNTs was also observed in the pattern structure shown in Figure 2.10. The CNT patterns exhibited micro-scale alignment, while lacking long-range alignment. Furthermore, the CNTs were found to undergo localized oriented assembly in the rectangular channel and microwell structures when these microstructures were of sufficiently small dimensions (15μm). As illustrated in Figure 2.11a, CNTs deposited in the microchannel structures generated a dense and one dimensional assembly transversely in the middle of the channel (Figure 2.11b), and also tended to assemble in a parallel fashion on the sidewall

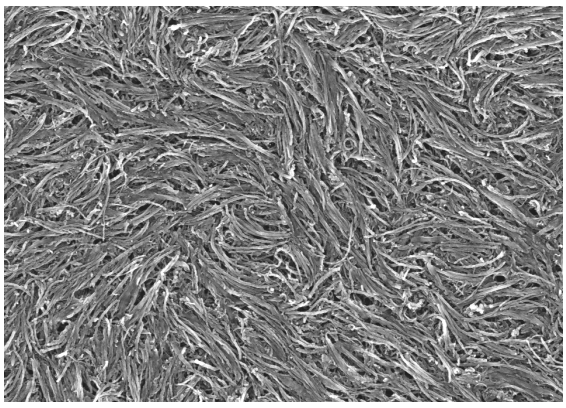

Figure 2.10: SEM images of localized alignment of CNTs deposited on unpatterned gold substrate.

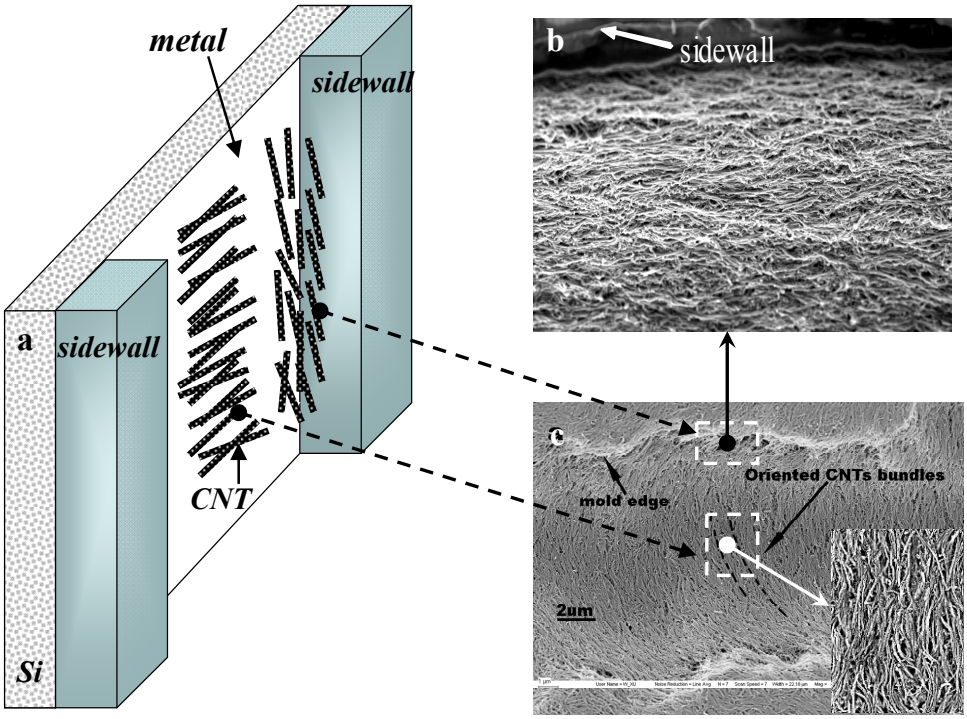

Figure 2.11: (a) Schematic of the alignment of CNTs after EPD deposition in microstructures with small dimensions, (b) SEM image of CNTs deposited along the sidewall of a silicon channel, and (c) SEM image of CNTs deposition in silicon micro-channel (insert: enlarged view of CNTs assembled in the middle of the trench).

of the channel (Figure 2.11c). However, this orientation effect was only observed in microstructures having openings with relatively small dimensions. For microstructures with larger dimensions, the CNTs seem to assemble in a much less oriented or random manner.

2.2.3.6 Effect of Surface Hydrophobicity on Selectivity of CNT Assembly

The surface hydrophobicity of the non-conductive layers, including the top surface exposed to the CNT dispersion, was found to play a significant role in the selective integration of CNTs into microstructures during the EPD process. In the case of interdigitated microelectrodes, the dielectric layer, which is underneath and between the

microelectrodes (Figure 2.1a), was exposed to a hydrofluoric acid (HF) aqueous solution (water:HF=50:1) for 10s that chemically removed the titanium adhesion layer between the gold and the dielectric layer during the electrode patterning process. This process was experimentally proved to be insufficient to completely remove the dielectric layer. The contact angle of the dielectric layer after the process decreased significantly as shown in Table 2.1. This rise of the hydrophilicity resulted in a continuous deposition of the CNTs over the whole microstructure, including the non-conductive dielectric region, which is not desired for selective pattern formation. This phenomenon may be due to the fact that CNTs aqueous solution can form a good interface with the hydrophilic surface where the moving CNTs under DC field collide and aggregate with the CNTs in the interface layer. A similar wetting effect was also observed by Han *et al.* in a spray coating process of CNT solution[38]. This negative effect can be reduced by changing the microelectrode patterning process from HF wet etching to a lift-off process by using acetone. In the later case, the hydrophobicity of the dielectric layers was preserved and 2-D patterns of CNTs on microelectrodes were achieved as shown in Figure 2.5a and 2.6a, with either parylene or SiN_x as the dielectric layer.

A similar hydrophobicity effect was further revealed in patterning CNTs into SU-8 microwell arrays. Oxygen plasma etching was applied to the array in the last step of the fabrication process of the SU8 microstructure in order to remove the possible residual of SU8 at the bottom of microwells. The surface topography of the pristine SU-8 before and after plasma treatment is shown in AFM images in Figure 2.12. Under the oxygen plasma treatment, the surface roughness increased from 0.289 nm to 12.149 nm. The contact angle of the micropattern dropped from 96.49 º to 28 º, which made the

Table 2.1 Contact Angle of the Dielectric Layer

Dielectric material	Contact angle without HF etching	Contact angle after HF etching
parylene	86.47º	59.54º
SiC	86.05º	43.88º
SiN_x	63.92º	40.41º
SiO_2	38.78º	<10º

surface turn from hydrophobic to hydrophilic. After the EPD process the CNTs generated a coating over the whole SU-8 microstructures (inserted image in Figure 2.13b), in contrast to forming a well-defined micropattern in each isolated microwell as shown in Figure 2.13a.

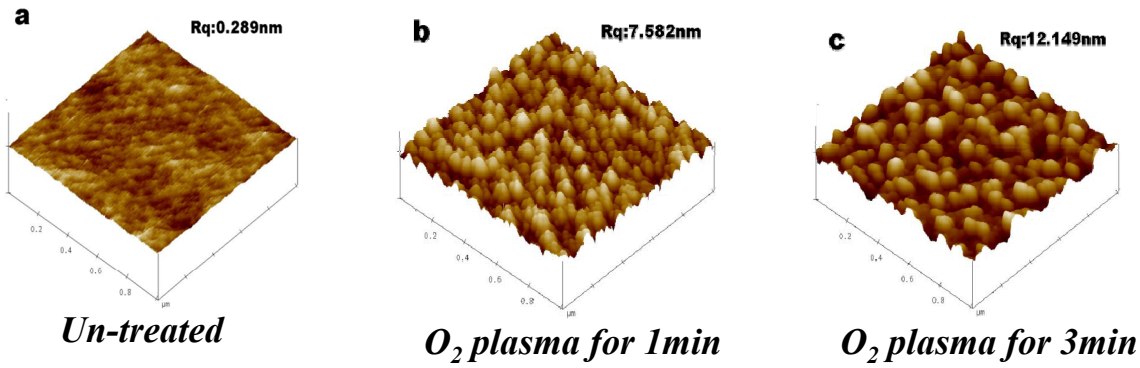

Figure 2.12: AFM images of the SU-8 flat surface: (a) without plasma treatment, (b) treated in O_2 plasma 200W for 1min, and (c) treated in O_2 plasma 400W for 1.5min. (Rq: surface roughness)

Another observation in this study is that the microwell patterns exhibit higher hydrophobicity than the flat/non-patterned SU-8 surface in all three stages. As illustrated in Figure 2.13c, after the oxygen plasma treatment, the contact angle was 28 º in the microstructure region and was close to 0 º in the flat area (i.e., non-patterned region). This is believed to be similar to surface topography-induced hydrophobicity[39].

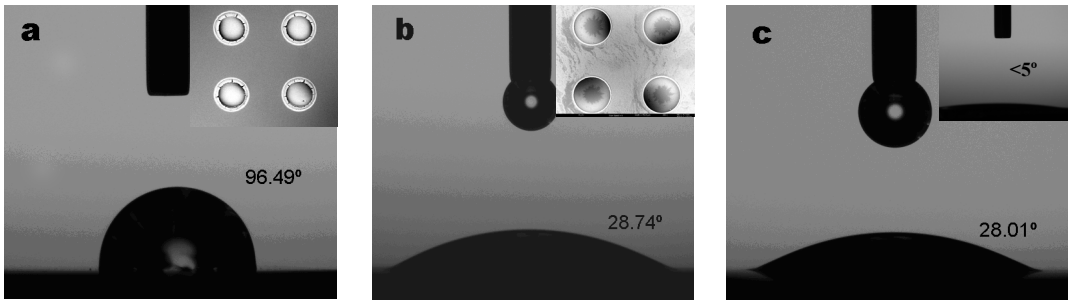

Figure 2.13: Contact angle measurements of: (a) pristine SU-8 microwell array (Insert: SEM image of CNT pattern), (b) plasma treated microwells with 200W power for 1min (Insert: SEM image of CNT pattern), and (c) plasma treated microwell array with 400W power for 1.5min (Insert: contact angle measurement of non-patterned SU-8 surface after plasma treatment).

2.3 Summary

In this Chapter, in an effort to effectively incorporate carbon nanotubes into microsystems, a MEMS-assisted EPD process was developed and studies. By patterning the electric field lines in a EPD process, CNTs were selectively directed into microstructures fabricated through MEMS technology. Uniform 2-D and 3-D micropatterns of CNTs with wafer-scale areas have been successfully achieved in both rigid and elastic system. This process offers favorable advantages such as high throughput, room temperature processing, good control over deposited mass, relatively

high resolution, and the ability to achieve micropatterns of pristine CNTs over a large scale on both rigid and compliant substrates.

Controllable CNT layer thicknesses ranging from 133nm to the micrometer range were accomplished within 5 min in a single step at room temperature. The deposited CNT layer thickness increased monotonically with the increase of applied electric field and deposition time when other process parameters were kept constant. Moreover, the morphology of the assembly film and the porosity of the CNT film were found to be readily controllable through the deposition parameters. Under appropriate deposition conditions, CNTs assembled conformally around the SU-8 microwell inner surface and generated a 20μm wide circular belt around the well opening, creating a continuous 3-D coating in each isolated well. Similar assembly behavior was revealed in rectangular microchannels constructed of photoresist, where a rectangular CNT belt was generated around the channel opening. This phenomenon was considered to arise from the conformal coating nature of the EPD process. The resultant CNT network displayed a random planar distribution with certain degree of local orientation when the feature size of the microstructures was sufficiently small. The high surface hydrophobicity of the non-conductive regions in microstructures was found to be critical to accomplish selective micropatterning of CNTs through this technique. Microstructures with hydrophilic dielectric regions yielded no selective patterning of the CNTs, which could be partially due to the potential wetting effect in the non-conductive hydrophilic regions.

Table 2.2 gives the comparison between the MEMS-assisted EPD technique and other reported CNT micropatterning/manipulation approaches. The patterning technique developed in this study offers all four favorable advantages simultaneously, which is

desirable for practical applications. The developed technique can be further applied to the co-electrophoresis or successive deposition of different materials to enable the fabrication of advanced CNT-based hybrid nanostrucutres for a variety of functional, structural and biomedical applications.

Table 2.2: Comparison of the CNT Patterning Approaches[10-19]

Approach	Process T[a]	Process duration	Throughput	Resolution
CVD growth	>400°C	hrs	medium	<10μm
DEP	RT[b]	minutes	low	N/A
LBL	RT	hrs	medium	<10μm
AFM	RT	hrs	very low	<100nm
Inkjet printing	RT	minutes	high	<100μm
Contact printing	RT	minutes	medium	<10μm
MEMS assisted EPD	**RT**	**<10min**	**high**	**<10μm**

[a]T: Temperature;
[b]RT: Room Temperature;

2.4 References

(1) JensenK; Kim, K.; ZettlA *Nat Nano* **2008**, *3*, 533.

(2) Kawano, T.; Chiamori, H. C.; Suter, M.; Zhou, Q.; Sosnowchik, B. D.; Lin, L. *Nano Letters* **2007**, *7*, 3686.

(3) Berson, S.; de Bettignies, R.; Bailly, S.; Guillerez, S.; Jousselme, B. *Advanced Functional Materials* **2007**, *17*, 3363.

(4) Yu, J.; Sow, C. H.; Wee, A. T. S.; Chua, D. H. C. *Journal of Applied Physics* **2009**, *105*.

(5) Boccaccini, A. R.; Cho, J.; Subhani, T.; Kaya, C.; Kaya, F. *Journal of the European Ceramic Society* **2010**, *30*, 1115.

(6) Boccaccini, A. R.; Chicatun, F.; Cho, J.; Bretcanu, O.; Roether, J. A.; Novak, S.; Chen, Q. Z. *Advanced Functional Materials* **2007**, *17*, 2815.

(7) Grow, R. J.; Wang, Q.; Cao, J.; Wang, D. W.; Dai, H. J. *Applied Physics Letters* **2005**, *86*.

(8) Chang, N. K.; Su, C. C.; Chang, S. H. *Applied Physics Letters* **2008**, *92*.

(9) Tong, H.; Sun, Y. *Ieee Transactions on Nanotechnology* **2007**, *6*, 519.

(10) Jeong, G.-H.; Olofsson, N.; Falk, L. K. L.; Campbell, E. E. B. *Carbon* **2009**, *47*, 696.

(11) An, L.; Cheam, D. D.; Friedrich, C. R. *The Journal of Physical Chemistry C* **2008**, *113*, 37.

(12) Fukuda, T.; Arai, F.; Dong, L. X. *Proceedings of the Ieee* **2003**, *91*, 1803.

(13) Xue, W.; Cui, T. *Sensors and Actuators A: Physical* **2007**, *136*, 510.

(14) Gao, B.; Yue, G. Z.; Qiu, Q.; Cheng, Y.; Shimoda, H.; Fleming, L.; Zhou, O. *Advanced Materials* **2001**, *13*, 1770.

(15) Small, W. R.; in het Panhuis, M. *Small* **2007**, *3*, 1500.

(16) Kordás, K.; Mustonen, T.; Tóth, G.; Jantunen, H.; Lajunen, M.; Soldano, C.; Talapatra, S.; Kar, S.; Vajtai, R.; Ajayan, P. M. *Small* **2006**, *2*, 1021.

(17) Liu, C. X.; Choi, J. W. *Journal of Micromechanics and Microengineering* **2009**, *19*.

(18) Lim, C. H.; Min, D. H.; Lee, S. B. *Applied Physics Letters* **2007**, *91*.

(19) Lee, K.; Lee, S. S.; Lee, J. A.; Lee, K. C.; Ji, S. *Applied Physics Letters* **2010**, *96*.

(20) Corni, I.; Ryan, M. P.; Boccaccini, A. R. *Journal of the European Ceramic Society* **2008**, *28*, 1353.

(21) Suzuki, Y. *IEEJ Transactions on Electrical and Electronic Engineering* **2011**, n/a.

(22) Gurrappa, I.; Binder, L. *Science and Technology of Advanced Materials* **2008**, *9*.

(23) Boccaccini, A. R.; Cho, J.; Roether, J. A.; Thomas, B. J. C.; Jane Minay, E.; Shaffer, M. S. P. *Carbon* **2006**, *44*, 3149.

(24) Karousis, N.; Tagmatarchis, N.; Tasis, D. *Chemical Reviews* **2010**, *110*, 5366.

(25) Shaffer, M. S. P.; Fan, X.; Windle, A. H. *Carbon* **1998**, *36*, 1603.

(26) Du, C.; Yeh, J.; Pan, N. *Journal of Materials Chemistry* **2005**, *15*, 548.

(27) Guduru M.; Dobbins T.A. *Mater. Res. Soc. Symp. Proc.* **2005**, *858E*.

(28) Boccaccini A. R.; Clasen R.; Uchikoshi T. *Electrophoretic Deposition: Fundamentals and Applications III (Key Engineering Materials)*; Trans Tech Publications, Ltd, 2009.

(29) Aliev, A. E.; Oh, J.; Kozlov, M. E.; Kuznetsov, A. A.; Fang, S.; Fonseca, A. F.; Ovalle, R.; Lima, M. D.; Haque, M. H.; Gartstein, Y. N.; Zhang, M.; Zakhidov, A. A.; Baughman, R. H. *Science* **2009**, *323*, 1575.

(30) Sekitani, T.; Noguchi, Y.; Hata, K.; Fukushima, T.; Aida, T.; Someya, T. *Science* **2008**, *321*, 1468.

(31) Hong, N. T.; Koh, K. H.; Lee, S.; Ngo, T. T. T.; Phan, N. M. *Journal of Vacuum Science & Technology B* **2010**, *28*, C2C5.

(32) Hu, L. B.; Li, J. F.; Liu, J.; Gruner, G.; Marks, T. *Nanotechnology* **2010**, *21*.

(33) Hu, L. B.; Pasta, M.; La Mantia, F.; Cui, L. F.; Jeong, S.; Deshazer, H. D.; Choi, J. W.; Han, S. M.; Cui, Y. *Nano Letters* **2010**, *10*, 708.

(34) Sharma, P.; Ahuja, P. *Materials Research Bulletin* **2008**, *43*, 2517.

(35) Choi, W. B.; Jin, Y. W.; Kim, H. Y.; Lee, S. J.; Yun, M. J.; Kang, J. H.; Choi, Y. S.; Park, N. S.; Lee, N. S.; Kim, J. M. *Applied Physics Letters* **2001**, *78*, 1547.

(36) Kordas, K.; Mustonen, T.; Toth, G.; Vahakangas, J.; Uusimaki, A.; Jantunen, H.; Gupta, A.; Rao, K. V.; Vajtai, R.; Ajayan, P. M. *Chemistry of Materials* **2007**, *19*, 787.

(37) Ma, C.; Zhang, W.; Zhu, Y.; Ji, L.; Zhang, R.; Koratkar, N.; Liang, J. *Carbon* **2008**, *46*, 706.

(38) Han, J. T.; Kim, S. Y.; Jeong, H. J.; Lee, G. W. *Industrial & Engineering Chemistry Research* **2009**, *48*, 6303.

(39) Su, Y. W.; Ji, B. H.; Zhang, K.; Gao, H. J.; Huang, Y. G.; Hwang, K. *Langmuir* **2010**, *26*, 4984.

CHAPTER 3

DESIGN AND FIBRACATION OF ELASTIC PDMS/CNTs FORCE AND STRAIN MICRO-SENSORS

3.1 Strain Sensors

Precise local pressure/strain monitoring is indispensible in fields such as biomechanical implants, artificial skins, touch screens and structural health monitoring[1]. For instance, strain sensors are responsible for detecting civil infrastructure damage and deterioration, which is essential to ensure the safe usage of these architectures and avoid catastrophes to people's properties and lives. Metal foil strain gauge and silicon piezoresistors shown in Figure 3.1 are two types of traditional strain sensors which have been well-developed.

The metal foil strain gauge is one of the most frequent choices in a structural health monitoring system. It is composed of a metallic foil pattern supported on an insulating flexible backing as shown in Figure 3.1a. The gauge is normally attached to the object by a suitable adhesive such as cyanoacrylate. The foil is generally arranged as a long, thin, conductive metal strip in a zig-zag pattern with parallel lines such that a small amount of stress in the direction of the orientation of the parallel lines results in a multiplicatively large strain over the effective length of the conductor, which gives rise to a large alteration in resistance. This type of strain sensor takes advantage of the conductance dependence on the geometry of a conductor. When stretched within the

limits of its elasticity, a metal structure becomes narrower and longer, and therefore electrical resistance will increase according to following equation:

$$R = \rho \frac{l}{A} \tag{3.1}$$

where R is the resistance of the structure, and ρ, l and A are the resistivity, length and cross-sectional area of the conductor. Conversely, when compressed such that it does not buckle, the structure will broaden and shorten, and resistance thereby decreases. As a result, the amount of applied stress/strain associated with the deformation of the object can be inferred from the resistance change. The sensitivity of a strain senor is characterized by the quantity known as the gauge factor (G), which is defined as:

$$G = \frac{\frac{R - R_0}{R_0}}{\varepsilon} \tag{3.2}$$

where R_0 is the initial resistance of the sensor and ε is the applied strain. The metal strain gauge offers advantages of easy fabrication and low cost. However, it has relatively large size and limited measurement resolution due to its small gauge factor (G=2-4)[2].

Another common type of strain sensor is the piezoresistive strain sensor. The piezoresistive effect of semiconductor materials like germanium, silicon, and silicon carbide can be several orders of magnitude larger than the pure geometrical effect in the metal strain gauge. Among them, silicon piezoresistors (Figure 3.1b) have been widely employed as pressure sensors and acceleration sensors, due to the high gauge factors (G=20-120)[3] and their compatibility with bipolar and CMOS circuits. The operation

mechanism of this type of device is based on the resistance changes induced by the alteration of both geometry and resistivity of the material. The resistance of n-type Si mainly changes due to the deformation of the multivalley conduction-band of Si atoms under strain/stress[4,5]. The shift of the band results in a redistribution of the carriers between valleys with different mobilities and further lead to varying mobilities dependent

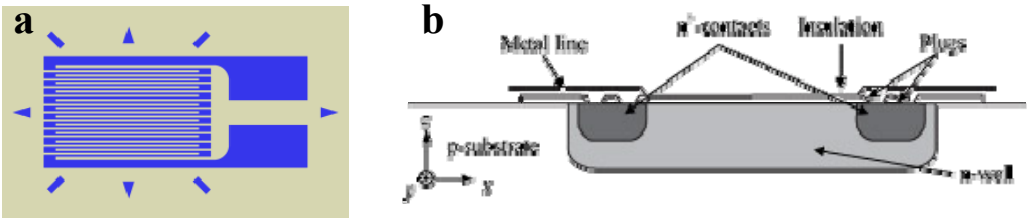

Figure 3.1: (a) metal foil strain gauge, and (b) silicon piezoresistive sensor.

on the direction of current flow[4]. Another minor effect is caused by the effective mass change related to altered shapes of the valleys. On the other hand, the phenomena in the p-type silicon piezoresistor are more complex and is a consequence of alterations in effective mass changes and hole transfer. Though outperforming metal foil strain gauge in terms of the gauge factor, the sensitivity of this type of device greatly depends on the temperature, doping level, crystalline structure and orientation by altering the band-gap[6,7]. As a result, they tend to be more expensive, more sensitive to temperature changes, and more fragile than foil gauges. Moreover, for both strain sensors, not being mechanically durable/conformable to end-uses and complex manufacturing processes hinder them becoming the "silver bullet" solutions in flexible strain sensing applications[8]. To overcome these issues and push forward the development of strain sensors, a new

generation of polymer composites with conducting fillers has been proposed and examined as piezoresistors.

3.2 Polymer/CNT Piezoresistive Composite

As alternatives to the metal/silicon based strain sensors, conductive filler loaded polymer nanocomposites are especially attractive when the structure undergoes mechanical deformation, since the combined architecture can benefit from both the elasticity of polymers and the piezoresistive properties of the conductive filler. The stretchable/flexible system not only is capable of covering surfaces and moving objects with arbitrary curvatures such as these in robots, but also enables development of low-cost, bio-compatible, and bendable electronics/systems. Carbon fibers[9], carbon black[10], and metal particles[11] have been introduced into polymeric matrices such as epoxy and rubber to create composite materials which exhibit reasonable piezoresistive properties, and which are also conformable and relatively easy to fabricate. The resistance change of these materials is primarily attributed to piezoresistivity induced by the change of tunneling resistance, where the average distance among adjacent conducting fillers is altered under compression or tension[11,12,13].

Compared with the aforementioned conductive fillers, carbon nanotubes offer an additional benefit of possessing very high intrinsic piezoresistive effect, apart from acting only as a pure conductive path. Under sufficient amount of stress or strain, the atoms of the carbon nanotube experience changes of local bonding from sp^2 to sp^3, resulting in alteration of the bandgap energy and electron transport property along the tube. Both theoretical modeling and experimental study have demonstrated an extremely high gauge factor of up to 2900 for CNT-based strain sensors[14,15]. For example, Stampfer *et al.*

applied tensile deformations to a suspended SWNT over a metallic cantilever support and observed a maximum piezoresistive gauge factor of 2900 arising from the change in the bandgap energy[14]. The result confirmed the potential of CNT in high performance nano-electromechanical displacement sensing. In addition, resistance responses of SWCNT to micro-scale strain were also revealed by mechanically deforming a CNT using an AFM tip[16]. It was found that different initial bandgap energy of a CNT gives rise to different piezoresistivity[17]. Small band-gap semiconducting (SGS) SWCNT shows higher piezoresistive responses than metallic SWCNT or large bandgap semiconducting SWCNT due to its potential to achieve a larger alteration in bandgap openings. This observation indicates that the piezoresistivity of CNT sensor can be tailored by choosing different types of CNTs in order to suit specific applications. However, a technical challenge so far is how to scale the nano-sensing properties of the CNT up to tangible and structural component length scales, while simultaneously controlling structure and assembly at the atomistic scale[18].

Moreover, by embedding a CNT interpenetrating network into an elastomeric polymer matrix and subsequently deforming it, the nanocomposite may exhibit a resistance change over a large strain range due to low Young's modulus (few MPa) and higher elasticity (up to 200%) of the elastomeric polymers, in contrast with silicon or metals which typically have a high Young's modulus of 20-100 GPa and elastic elongation of less than 4%. The favorable merits, such as high piezoresistivity associated with both the deformation of CNT-polymer network and the individual CNT, large working range and low cost, have made the CNT-elastomer nanocomposites an attractive alternative for the next generation of conformable strain/stress sensing component with

high resolution. These nanocomposites have been exploited in applications which require ductile properties of sensors, such as in situ pressure monitoring inside the human body (Figure 3.2). Intensive efforts have been made so far to develop CNT-thermoplastic or CNT-thermosetting polymer strain/stress sensors with the piezoresistive effect as the primary readout mechanism. CNTs have been introduced into a variety of polymer matrices, including PDMS[19], poly (L-lactide)[1], polyelectrolyte (PE)[20], Ethylene-Propylene-Diene-Monomer (EPDM)[21], polyimide[22], polyisoprene[23], PMMA[24]and so on. The reported gauge factor in these work ranges from 7-50 and the maximum applied strain is ~15% before device failure, which is superior to the conventional metal foil strain gauge and silicon piezoresistors in terms of higher sensitivity, flexibility and the capability of detecting larger deformation.

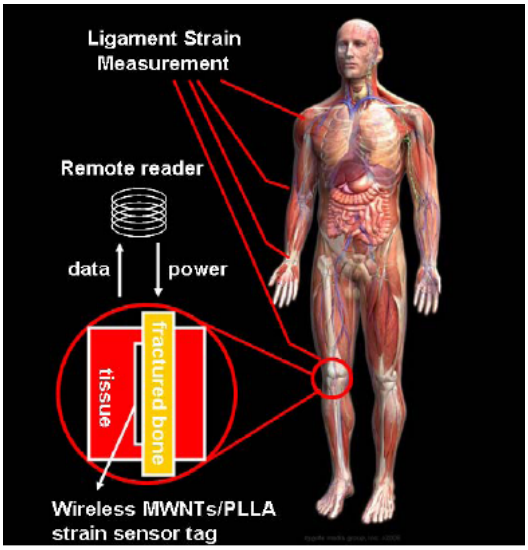

Figure 3.2: An experimental setup for remote measurement of strain inside the human body[1].

Up to now, the majority of reported CNT-polymer composite sensors are fabricated through blending of the constituents, where CNTs are mixed and dispersed throughout the polymer matrix. They are later cut or molded into desired shapes/geometries for micro-sensor applications. This approach carries process simplicity and good control over the weight ratio of the CNTs in the polymer matrix. Nevertheless it consumes large amounts of CNTs, and has further challenges of ensuring homogeneous dispersion of CNTs in viscous solutions and low viscosity required in the micromolding process. For instance, as part of our discussions in Chapter 2, only a maximum load of wt-30% of CNTs in PDMS can be achieved during the microcontact printing process of CNTs due to rheology issues associated with mixing the viscous elastomer with high volume fraction of CNTs[25]. The resultant composite film usually lacks optical transparency, which further limits the material to serve as flexible transparent electrodes/sensors in certain applications[19]. On the other hand, in CNT-based elastic microsystems, both CNT-loaded and CNT-free regions are usually required within the elastomer matrix, e.g. the stretchable organic transistor shown in Figure 3.3. Microcontact printing is one of the promising methods to achieve CNT micropatternig on elastomers. However this approach requires pre-mixing of CNTs in silicone rubber prepolymer, followed by spin coating of the viscous mixture to ensure a leveled surface that is critical in this process[25]. So the rheology problem remains a challenge. As shown in Chapter 2, by combining the MEMS-assisted EPD approach with a micromolding process, complex CNT micropatterns can be effectively generated on various polymer substrates, while eliminating the issues associated with rheology and dispersion of CNTs in polymer (Figure 2.7). In this work, the proposed technique was utilized to fabricate

PDMS/CNTs micro stress/strain sensors. Polydimethylsiloxane (PDMS) was chosen to serve as the elastic matrix for fabrication of CNT polymeric strain/stress sensors. PDMS is known to carry several distinctive properties including high mechanical elasticity, easy processiblity,

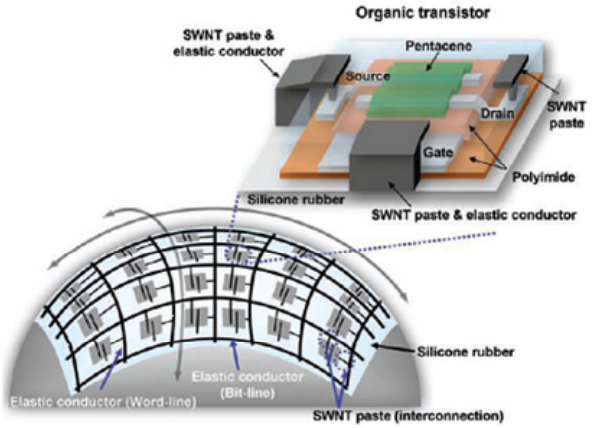

Figure 3.3: CNT flexible microelectronics[26].

biocompatibility, optical transparency, chemical stability and low cost, which have enabled wide applications in bio-medical, microfluidic and electronics fields[27]. In addition, it has a wide thermal operating range from −100 to 250 °C, which is suitable for high temperature/harsh environment applications. The MEMS-assisted EPD process not only patterns the CNTs, but also preserves the good rheological properties of unfilled PDMS and efficiently utilizes the CNTs. A variety of complex CNT micropatterns were realized on PDMS substrates as presented in Figure 2.7 and two types of CNT-PDMS sensors, strain and force sensors, were fabricated and their performance were characterized separately. The correlation between the piezoresistive behavior and the composite

properties was also established.

3.2. Fabrication and Material Development

Detailed description of the experiments and discussion of 2D/3D micropatterning of CNTs on both rigid and PDMS substrates through MEMS-assisted EPD process and micromolding process is given in Chapter 2. The specific design and fabrication of the PDMS/CNT microstructures for the evaluation of sensor performance will be discussed separately in the subsequent device testing section.

Scanning Electron Microscopy (SEM) (Zeiss, Ultra60) was utilized to study the morphology of the CNT micropatterns and PDMS/CNT bilayer structure. Energy-dispersive X-ray spectroscopy (EDS) was used to characterize the elemental composition of the topmost surface of the PDMS/CNT microstructures. Raman spectroscopy was exploited to probe the modification of the electronic structure in strained CNT.

3.3 Results and Discussion

3.3.1 Morphology of the Transferred CNT Patterns on the PDMS Matrix

The images in Figure 2.7 in Chapter 2 have shown that a variety of CNT patterns such as micro-springs, micro-coils and micro-pads ranging from micro to macro-scale have been achieved on compliant polymer substrate through the proposed technique. Figure 3.4a showed that the top surface of the PDMS/CNTs composite was found to be a smooth layer with the CNT buried underneath a continuous film. The SEM imaging in Figure 3.4b showed that the resultant PDMS/CNTs composite exhibited a bi-layer structure, a thin, highly-CNT-loaded PDMS layer sits atop a CNT-free PDMS bulk layer

which was molded from the original silicon micro-channel structure illustrated in Figure 2.4. The bottom bulk PDMS layer may provide additional mechanical support to the top

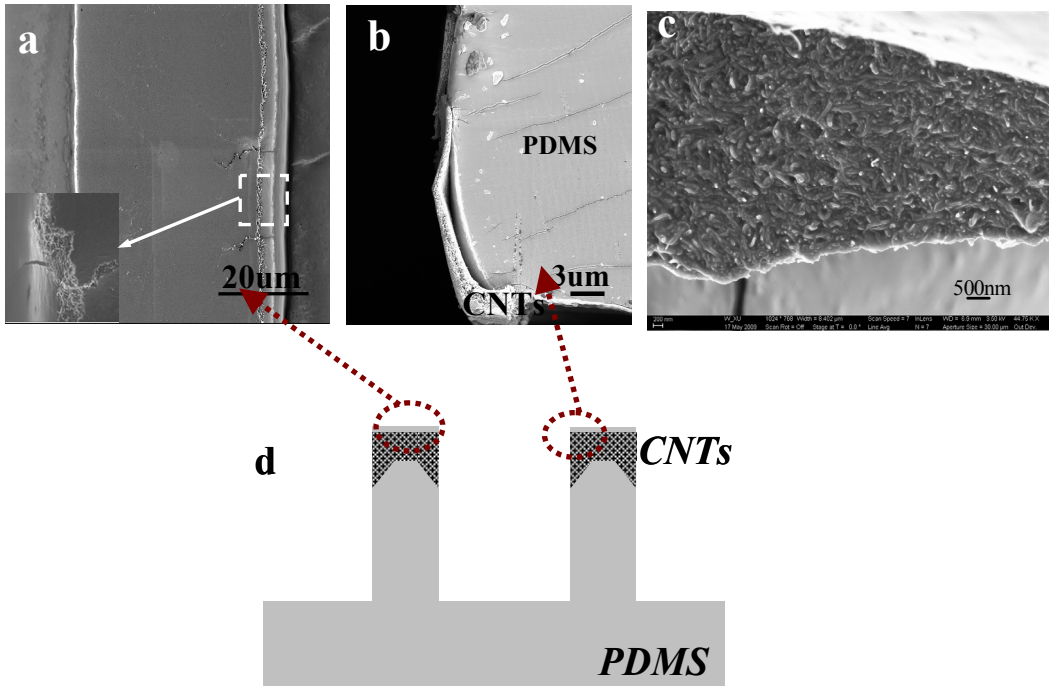

Figure 3.4: SEM images of PDMS/CNT bilayer microline (a) top surface view, (b) cross section view, (c) inner CNT layer and (d) scheme of the PDMS/CNT microline.

CNT layer. The thickness of the CNT layer in Figure 3.4b was found to vary from 800nm in the center to 4μm near the edge due to the non-uniform electric field distribution inside the silicon microchannel as discussed in Chapter 2. The SEM image of the CNTs layer in Figure 3.4c showed that inside the CNT/PDMS layer, each CNT was in situ coated with PDMS and the PDMS formed a matrix that interpenetrated the CNT network. This image confirmed that with the aid of vacuum degassing, the PDMS prepolymers penetrated and filled the voids in the CNT network during the micromolding process.

Figure 3.5 is the SEM image of the top surface of the CNT pattern in the PDMS matrix as illustrated in Figure 3.4d. The SEM observation of the top surface of the composite indicated that the CNTs were embedded underneath an ultra-thin film (~10nm). Further element spectrum study by EDS at a low voltage (4kV) was performed to probe the uppermost layer. The elemental weight percentages of carbon, oxygen and silicon of the composite were consistent with those of unfilled PDMS (Table 3.1). This thin PDMS film (~10nm) was considered to form in-situ during the micromolding process performed on the CNT patterns. During the PDMS micrmolding process, the pre-polymers of PDMS flowed from the top surface of the porous CNT layer and gradually penetrated the CNT network with the aid of vacuum degassing and capillary force. The contact area of each CNT with the bottom gold surface was small due to the cylindrical shape of the CNT. In addition, CNTs formed a randomly-oriented porous network at the interface with the gold layer (Figure 2.9), as opposed to generating a dense monolayer that could cover the whole interface and prevent all the prepolymers from reaching the gold surface. So the prepolymers were able to reach the Au surface and formed a quasi-continuous layer/film after curing.

The thin film may serve as an isolation layer between the CNTs and the ambient environment. Moreover, such a structure can potentially facilitate the heat conduction/dissipation in a practical sensing application when current runs through the CNT network, since the CNT layer sits very close to the surface of the composite, as opposed to bulk loaded polymer/CNTs composites where majority of CNTs are embedded deep inside the polymer bulk matrix which usually leads to a low heat conductivity. The CNT-PDMS bilayer structure produced in this way is capable of

preserving the optical transparency of the film which is advantageous in certain optical applications. The developed composite consists of a patterned CNT layer sandwiched

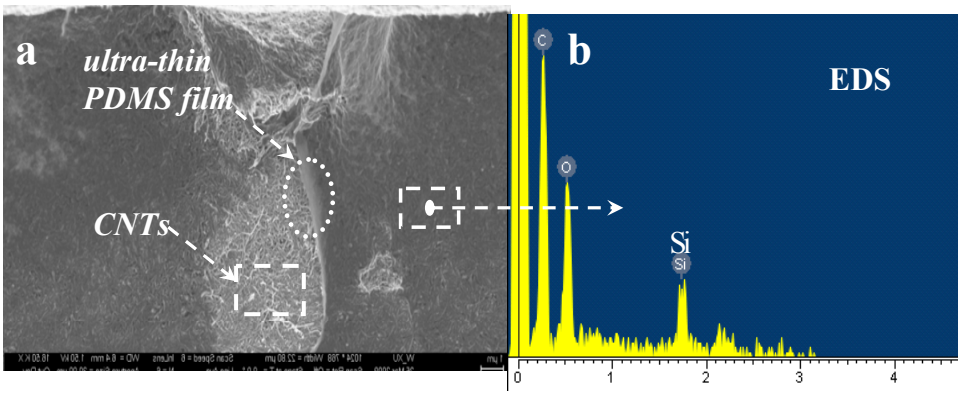

Figure 3.5: (a) SEM image of the top surface of PDMS/CNTs, (b)EDS spectrum of the top surface of PDMS/CNT microline.

Table 3.1 Elemental composition of the top surface of PMS/CNT composite

Spectrum	C	O	Si	Total
PDMS	32.96	32.74	34.3	100
PDMS/CNTs	33.91	32.70	33.39	100

between an ultra-thin surface film (~10nm) of PDMS and a bulk PDMS layer. This specially constructed sandwiched structure of the CNTs/PDMS also demonstrates charge storage capability and can act as an elastic power generator, which will be discussed in detail in Chapter 4.

3.3.2 Evaluation of the Resistance Response upon Transverse Compression Force

To validate the piezoresistivity of the produced PDMS/CNT composite, the relationship between resistance of the flexible microstructures and transverse compressive force was studied. The PDMS/CNT composite used for the testing was produced from first depositing CNTs into an array of silicon trenches with a depth of 30μm, a width of 40μm and a length of 1cm through the MEMS-assisted EPD process developed in Chapter 2 under an electric field of 15V/cm and the CNT concentration of 0.1g/L for 2min. At the bottom of each trench, there was a 500nm-thick gold layer deposited through E-beam evaporation that served as the electrode for the CNT assembly. The spacing between two adjacent trenches was 40um. Then the CNT patterns inside the silicon trench were transferred into the PDMS substrate through the aforementioned transfer micromolding process to achieve the CNT microline array on PDMS elastomer.

The scheme of the experimental test setup is shown in Figure 3.6. A sample film was placed on an electronic balance on a probe station. Two probes were placed 800um apart on a 40μm wide testing PDMS/CNT microline. An Agilent 34401A 6.5 digit multimeter was connected to the two probes to determine the resistance of the microline. The transverse compression force was applied using a 70μm-wide probe in the longitudinal center of the testing microline. During the testing, the two probes for the resistance readout were carefully adjusted each time after the force was applied to ensure good contact with the CNTs layer in order to minimize changes in the contact resistance. The compression force was read from the electronic balance supporting the sample.

The transverse compression force sensitivity of the PDMS/CNT bilayer micro-line was shown in Figure 3.7. The structure exhibited positive piezoresistive behavior and the resistance increased along with the increase of the transverse

compression force. With 7.68mN force, the resistance increased significantly from 0.23MΩ to 2.9MΩ. It was restored to the value of 0.25 MΩ when the load was

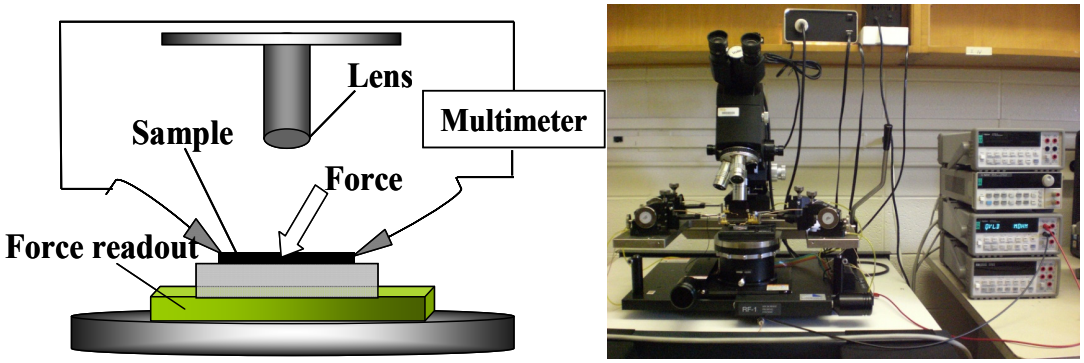

Figure 3.6: Left: Scheme of experiment setup of the transverse compression force sensing. Right: digital image of the experimental apparatus.

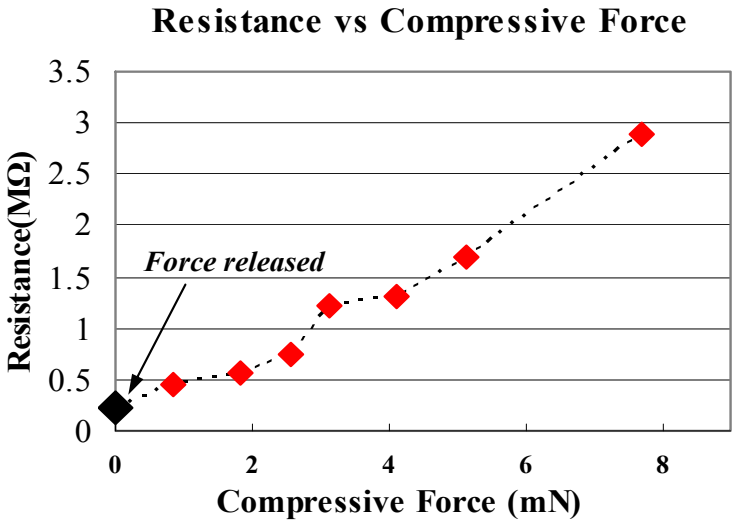

Figure 3.7: Compressive Force vs. Resistance of PDMS/CNT bilayer microline.

released. A cyclic force study on the same microline confirmed that the resistance of the composite can always recover to the value which is very close to the original value

(Figure 3.8). This result confirms that the increase of resistance is not due to damage of the PDMS/CNT conductive layer.

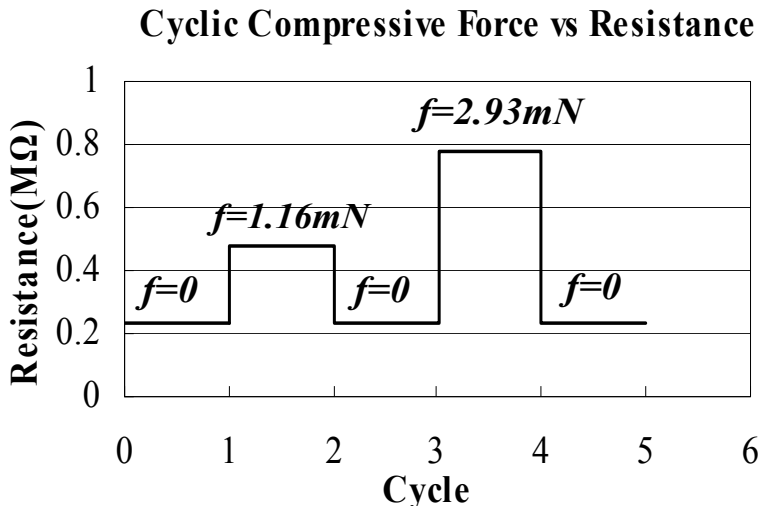

Figure 3.8 : Cyclic Force vs. Resistance on PDMS/CNT microline.

3.3.3 Characterization of the PDMS/CNTs Strain Sensor

The mechanical-resistance relationship of the nanocomposite was further characterized with a monotonic tensile testing in a Mini ElectroForce® 3100 Test Instruments (Bose, USA). As shown in Figure 3.9, a 200μm wide and 1000μm long PDMS/CNT bi-layer microline with two 2mm×2mm CNT pads at the two ends was fabricated through the process similar to that described above. Here, two CNT pads were designed and fabricated for the electrical connection from the center microline to the external output circuit. The frame, as shown in the middle picture of Figure 3.9, is made from a polyurethane resin (Vero 720) and was generated by a 3-D printer (Objet Eden 250). The frame was coated with three metal layers titanium (90nm)/gold (400nm)/ titanium (90nm), except for the wing area at the two sides of the center frame to

electrically isolate the two ends of the frame. The non-CNT-bearing regions of the CNT/PDMS sample were O_2 plasma treated (except for the CNT area) to increase the bonding strength with the epoxy-based glue. The two CNT pads were glued using silver epoxy to the metal layer on the two ends of the frame separately with the CNTs layer facing down to the frame, and the center 1mm-long microline was suspended over the 1mm-long gap of the frame. Epoxy-based glue was further applied to fully bond the sample to the frame. Two metal wires were adhered to the two ends of the frame using silver epoxy for the resistance readout. Monotonic tensile strain testing was then performed by a WinTest® digital control system. The resistance R was obtained through a multimeter connected to the metal wires. The gauge factor was calculated by equation 3.2, with the strain obtained from the WinTest® device and the resistance measured as described above.

To investigate the sensitivity of the conformable CNT-PDMS thin film strain

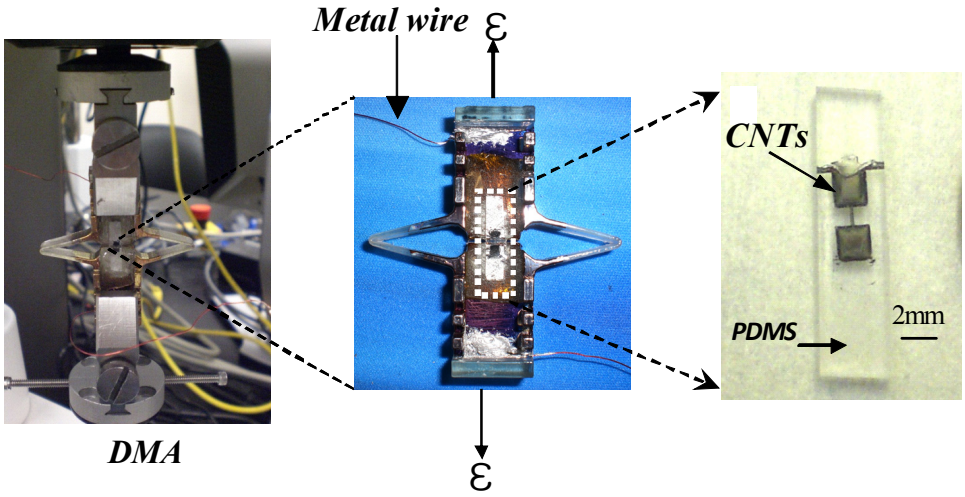

Figure 3.9: Left: digital image of the sample clamped between two movers in DMA apparatus, middle: digital image of testing frame with sample packaged in it, and right: digital image of the test PDMS/CNT film.

sensor, a series of laboratory experiments were undertaken where thin films with different initial resistance (R_0) were loaded under monotonic load patterns. The piezoresistive response of the PDMS/CNT bi-layer microstructure was characterized as a strain sensor. Four PDMS/CNTs strain sensors with different initial resistances, were tested under the same experimental conditions. The normalized resistance of the four samples displayed similar monotonic increase under the increase of strain (Figure 3.10). For the two samples with a lower R_0, they exhibited linear mechanical-resistance change in the small tested strain range (<2.5%), with extracted gauge factors (G) of 20 (R_0=462KΩ) and 31(R_0=380KΩ), respectively (Figure 3.11). Under a higher tested strain range (2.6% ~ 14%), non-linear relationships were observed for these two samples. After the strain was released, the resistances of the above two samples immediately restored to 420KΩ and590KΩ. The resistances were further reduced to 390 KΩ and 450 KΩ after 4 hours, which indicated that the microlines were not permanently deformed or damaged

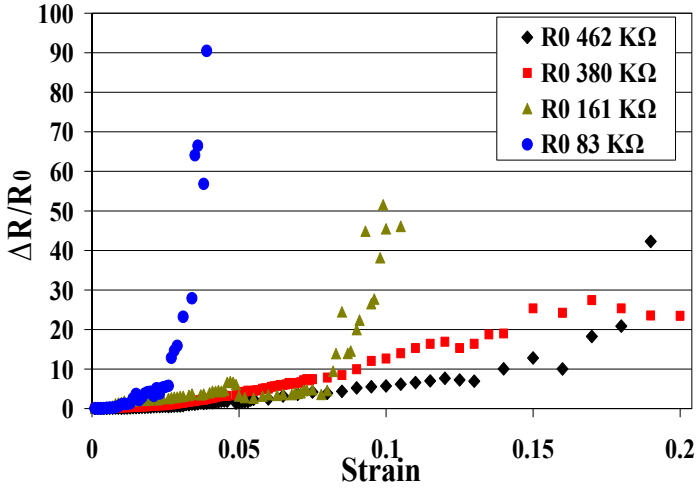

Figure 3.10: Strain vs. percentage change in resistance of the PDMS/CNTs microline with different initial resistance R_0.

during the sensing process. The delay of the recovery of the resistance is likely due to the viscoelasticity of the PDMS, as it takes some time for the stretched PDMS molecular chains to retract and readjust themselves back to the original unstrained state. For samples with lower initial resistance (83 KΩ and 161KΩ), the structures exhibited much higher piezoresistive response than the ones with lower R_0, as observed in the difference of the slopes of the curves (G) in Figure 3.10 and Figure 3.11. However, compared to the samples with higher R_0, the ones with lower R_0 exhibited more pronounced non-linearity over the whole testing region. The pullout of the concentric graphene tubes of MWCNT may be one of the factors which is responsible for this degradation of linearity[28]. Dang *et al.* also reported very similar nonlinear piezoresistive behavior in a silicone rubber/MWCNTs pressure sensor, while exact mechanisms are not yet to be concluded[29].

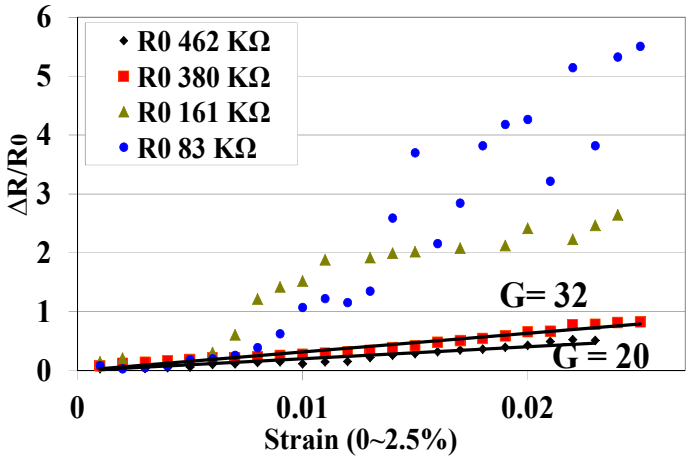

Figure 3.11: Piezoresistive response of CNT-PDMS microline under a small strain range (0~2.5%)

As the sensor sensitivity demonstrated a strong dependence on both the initial resistance of the device and the applied strain, a more detailed study was conducted in

order to gain a better understanding on the piezoresistive behavior of the PDMS/CNTs composite in this system. The acquired information can potentially provide both useful scientific insights and technical guidance for the design and fabrication of this type of sensors. The sensitivity of six samples (four were shown in Figure 3.10) with different R_0 were evaluated. Figure 3.12 gives a typical curve profile of the relationship between the normalized resistance change and the applied strain in this system. It exhibited three regions. In the region I where the applied range is from 0~1%, the curve shows a linear relationship in all tested samples, so the gauge factor can be extracted by fitting the curve in this region using the equation 3.2 and it is referred to G1. In region II and III, in which the applied strain is between 1% to 2% and 2% to 10%, the curve was found to have different degree of non-linearity. In order to compare the change of the G as a function of

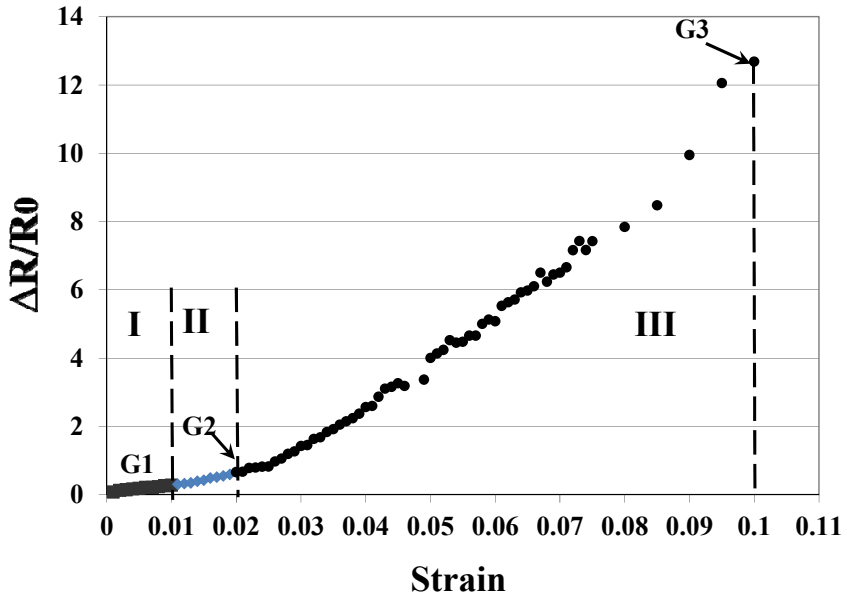

Figure 3.12: A typical graph of the relationship between normalized resistance change and applied strain of the composite.

strain, the values of G at the strain of 2% and 10% were calculated according to equation 3.2, and were referred to as G2 and G3 separately in Figure 3.12 and Figure 3.13. Gauge factor for each sample under each of the abovementioned three strain levels, as well as the gauge factor for samples with different R_0, were plotted together in Figure 3.13.

In all three strain levels, the sensitivity of each sensor (G) first exhibited a decrease as a function of increasing R_0 when R_0 was below a certain value (zone 1). The gauge factor then started to increase when R_0 was above that value (zone 2). It was also observed in Figure 3.13 that the gauge factor for all the tested devices increased consistently with the increase of the applied strain level.

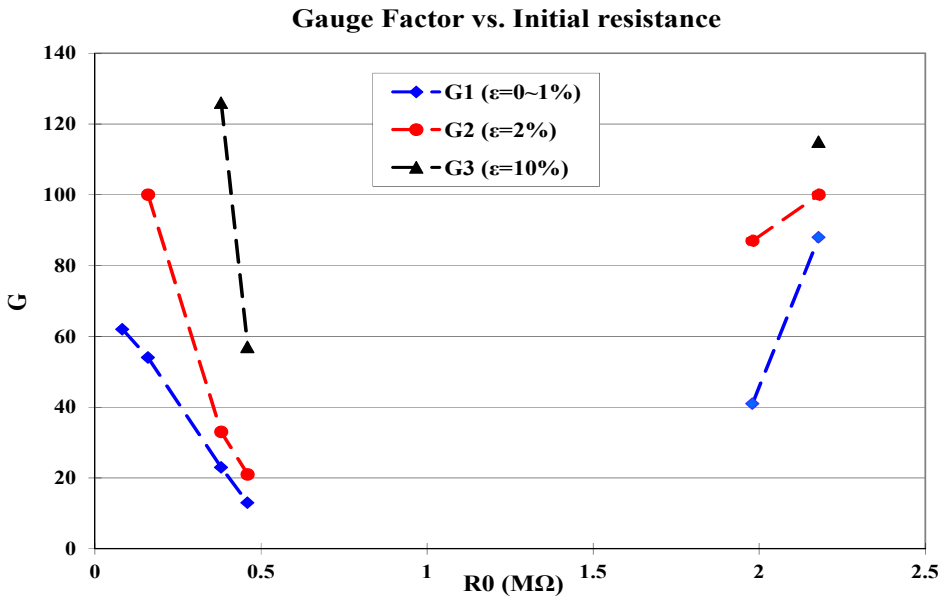

Figure 3.13: Gauge factor (G) as a function of the initial resistance (R_0) of the sensor and the applied strain range (ε). (G1, G2, and G3 are gauge factors under the three different strain levels shown in Figure 3.12.)

3.3.3.1 Possible Piezoresistive Effects in a CNTs-loaded Polymer Composite

In contrast to metal, the total resistance of a PDMS/CNT microline is attributed to three factors, as illustrated in Figure 3.14. When electrons are injected into the composite, they first have to overcome the intrinsic resistivity of the individual tube (R_i) in order to be transported. When electrons reach the end of the tube, they need to further overcome the energy barrier associated with the tunneling resistance (R_t) between two adjacent CNTs to move forward within the CNT network. Meanwhile, the resistance arising from the geometry of a conductor structure adds up to the total resistance of the composite (R_d) as well. When a tensile strain is applied to this structure, R_d, R_t, and R_i will change accordingly because the dimension of the structure, the distance between two adjacent CNTs and the length/geometry of an individual CNT will likely be altered. Consequently,

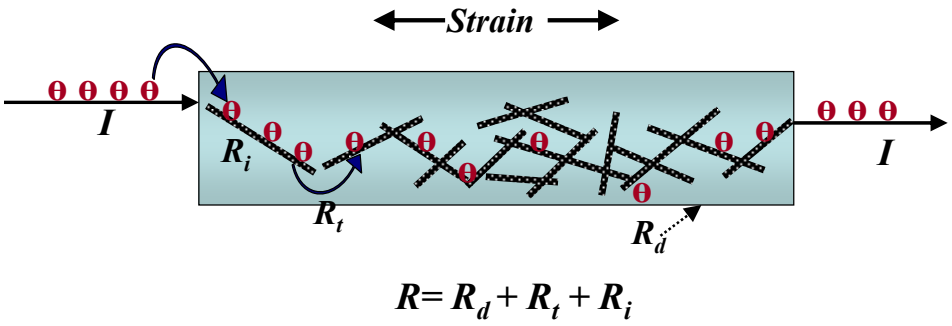

Figure 3.14: Scheme of electron transportation in a PDMS/CNT composite.

there are three possible piezoresistive mechanisms that may contribute to the sensing capability of a CNT-loaded polymer composite, which are termed in this study as G induced by dimensional change (G_d), G induced by alternation of tunneling resistance (percolation effect) (G_t) and G induced by modification of CNT bandgap (G_i). Given the

fact that the total resistance change is the sum of three effects, the total piezoresistivity (G) is the result of all three effects.

Each type of the gauge factors can be further deduced as following:

i) For the piezoresistivity caused by the dimensional change of a conductive line, the density of the composite can be assumed to be constant under relatively small applied strain. Since the PDMS is an incompressible material, then

$$A_0 \times l_0 = A_1 \times l_1 \tag{3.3}$$

where A_0 and l_0 are the initial cross-sectional area and length of the composite, A_1 and l_1 is the cross-sectional area and length of the line under applied strain,

as $R_1 = \rho \frac{l_1}{A_1}$, $R_0 = \rho \frac{l_0}{A_0}$ and $l_1 = (1+\varepsilon)\, l_0$, G_d can be calculated by the equation:

$$G_d = \frac{\frac{R_1 - R_0}{R_0}}{\varepsilon} = \varepsilon + 2 \tag{3.4}$$

where ρ is the density of the microline, ε is the applied tensile strain, R_1 and R_0 are the resistances at ε and zero strain. Equation 3.4 indicates that G_d increases linearly with the applied strain. Since the working range of the strain in most strain sensors is less than 15%, the gauge factor of a sensor, of which piezoresistivity relies entirely on the dimensional change is limited to 2.15, which is the case for most of the reported metal foil strain gauges.

ii) For the piezoresistivity induced by the change of tunneling resistance and total number of conductive paths in a composite, the resistance under strain can be expressed by the equation[24,30] :

$$R = R_T \frac{l_T}{A_T} = n \cdot (\exp(\frac{E_a}{k_B T})) \tag{3.5}$$

where R_T is the tunneling resistance, l_T and A_T are the effective length and the effective cross-sectional area of the tunneling resistance, n is a proportionality constant, E_a is the tunneling activation energy of the contact barriers, k_B is the Boltzmann constant and T is temperature. The resistance change can be further calculated as[31,32,33]:

$$\frac{R(\varepsilon)}{R_0} = \exp(2\alpha d_0 \varepsilon) \tag{3.6}$$

$$\alpha = \frac{2\pi}{h}(2m\varphi)^{1/2} \tag{3.7}$$

where $R(\varepsilon)$ and R_0 are the resistance under strain (ε) and $\varepsilon=0$, d_0 is the tunneling distance between CNTs, h is Planck's constant, m is the mass of the charge carriers, and φ is the height of the tunneling barrier. For a given composite material, α and d_0 can be considered as constants. The gauge factor, G_t, is:

$$G_t = \frac{\frac{R(\varepsilon) - R_0}{R_0}}{\varepsilon} = \frac{\exp(2\alpha d_0 \varepsilon) - 1}{\varepsilon} \tag{3.8}$$

G_t therefore exhibits a non-linear relationship with the applied strain. In order to compare the gauge factor observed in our study with the theoretical values, literature reported or theoretically predicted values of the variables, α and d_0, were chosen to obtain the correlation between G_t and ε, as well as the approximate range of G_t,

predicated by this theory. d_0 is set to be 5nm because this value is considered to be the maximum in a CNT- loaded nanocomposite to allow the composite to be conductive[34,35]. By choosing the maximum d_0, the maximum value of G_t could be obtained. α was reported to be around 1.65 x10^9~2.75 x 10^9 in a polyimide/SWCNTs system[30]. G_t can then be plotted as a function of applied strain according to the equation 3.8, as shown in Figure 3.15. G_t exhibits a non-linear monotonic increase with the increased strain. In addition, G_t was also reported to increase with increased R_0 of the device in this system, which is a reasonable phenomenon since the resistance change under strain will be more pronounced when the total number of conductive paths in the composite decreases. Therefore the piezoresistive effect was found to be more pronounced when the concentration of CNTs distributed in a polymer matrix is close to the percolation threshold[30,36,37].

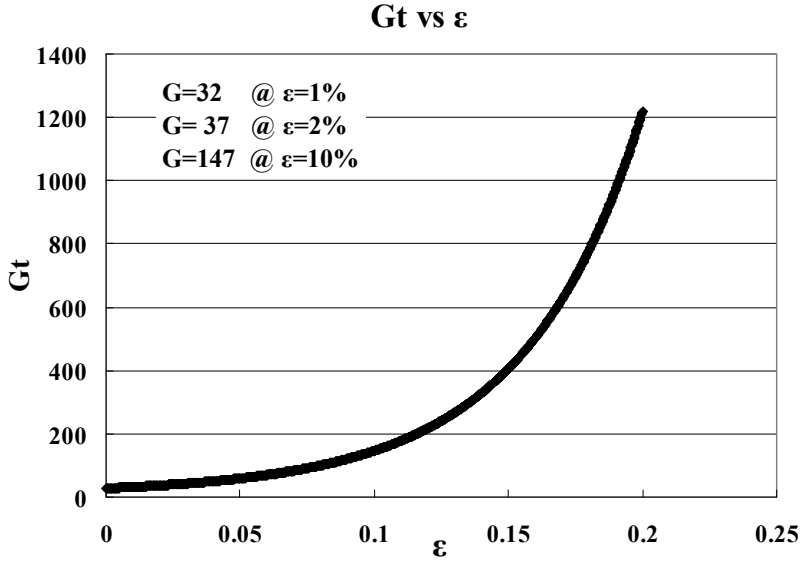

Figure 3.15: Modeled gauge factor (G_t) induced by tunneling resistance change as a function of applied strain (ε).

iii) As briefly discussed in section 3.1, an individual CNT exhibits unique intrinsic piezoresistivity due to the change of bandgap energy under strain/stress. The resistance under strain can be modeled according to the thermal activated transport[14] as following:

$$R_i(\varepsilon) = \frac{1}{|t|^2}\frac{h}{8e^2}\left[1+\exp(\frac{E_g(\varepsilon)}{k_B T})\right] \tag{3.9}$$

where $|t|^2$ is the transmission through the carbon nanotube, $E_g(\varepsilon)$ is the strain-dependent band gap of a metallic nanotube (torsion contributions are neglected) and $E_g = (\frac{dE_g}{d\varepsilon})\cdot\varepsilon$. e is the elementary positive charge, h is Planck's constant, k_B is the Boltzmann constant, and T is temperature. The gauge factor (G_i) –strain relationship then obeys the equation:

$$G_i = \frac{\exp(\frac{E_g(\varepsilon)}{k_B T}) - \exp(\frac{E_g(\varepsilon=0)}{k_B T})}{\left[1+\exp(\frac{E_g(\varepsilon=0)}{k_B T})\right]}\frac{1}{\varepsilon} \tag{3.10}$$

Similar with G_t in (ii), G_i exhibits a non-linear relationship with the applied strain as well. In addition, equation 3.10 indicates that G_i varies with zero-strain bandgap energy ($E_g(\varepsilon=0)$) which largely depends on the type of a specific CNT. This result explains the wide-range of the reported values of G_i for different carbon nanotubes (semiconductive, metallic or small-bandgap), ranging from 200 up to 2900[14,38]. One example of the reported G_i- ε curve is given in Figure 3.16. Both experimental results

and theoretical analysis confirm that G_i increases monotonically with applied strain. Equation 3.10 only considers the effect of tensile strain, in the real application, deformations such as bending, distorting, flattening and twisting can also result in alteration of the electronic transport property of a CNT and give rise to intrinsic piezoresistivity[14,15]. As discussed in Chapter 1, CNT has a high aspect ratio hollow structure which leads to a relatively weak mechanical stiffness and Young's modulus (several GPa) in the radial direction. Even Van der Waals force can deform the tube in the radial direction. Stampfer *et al.* showed that a transverse force of 50 nN is sufficient to induce 1% strain of a SWCNT[14]. Hence this type of deformation may potentially occur when a densely entangled CNT network is strained.

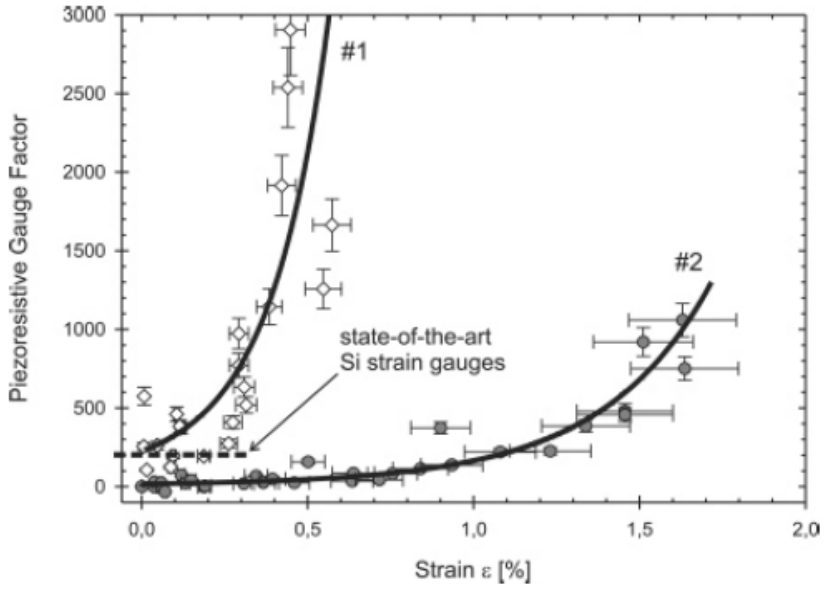

Figure 3.16: Gauge factor of two different SWCNT (sample #1 and #2) as a function of strain reported by Stampfer *et al.*[14]. The solid lines are computed from the theoretical model (equation 3.10).

3.3.3.2 Thickness Dependence of the Initial Resistance (R_0) and Initial Resistivity

As plotted in Figure 3.16, R_0 of the PDMS/CNT microline demonstrated a non-linear decrease with increased CNT layer thickness (*d*). This is likely due to the increased number of conductive paths within a CNT network when the CNT layer becomes thicker[19,39]. As indicated in Figure 3.17, the percolation threshold in the composite produced from the MEMS-assisted EPD process was likely to appear when the CNT layer thickness was approximately 400~500nm . When *d* reduced to a value that is well below the percolation point (e.g. *d*<200nm), the R_0 increased rapidly and eventually became infinite (the composite became non-conductive), which could be attributed to insufficient entanglement/contact of CNT tubes that formed continuous conductive paths

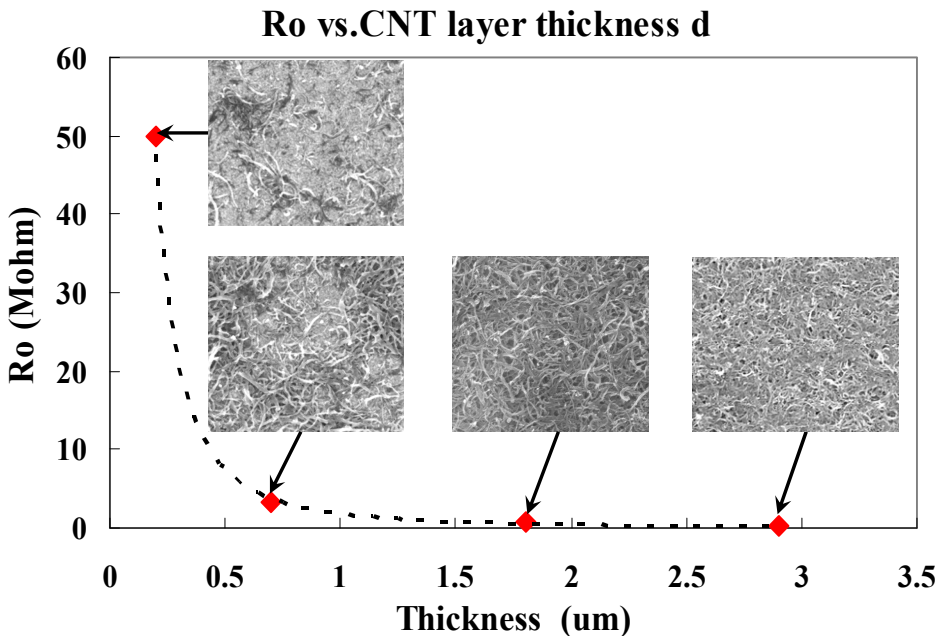

Figure 3.17: R_0 as a function of the CNT layer thickness in PDMS/CNTs microline. Inserted SEM images: morphology study on samples with different CNT layer thickness.

in the polymer matrix. This lack of entanglement was further revealed by the SEM images in Figure 3.17, where the tubes were barely in contact with each other in this R_0 region.

Furthermore, since the relationship between resistance and resistivity of a conductive line follows the equation:

$$R = \rho \frac{l}{A} = \rho \frac{l}{d \cdot w} \tag{3.11}$$

where ρ is the resistivity, l, w and A are the length, width, and the cross-sectional area of the microline, d is the thickness of the CNT layer. The relationship between the ρ and the d can be established accordingly, as shown in Figure 3.18. The resistivity of the CNT layer demonstrated reduction when d increased. The results agree well with the results obtained from the morphology study in Figure 3.17 and Figure 2.9, where the

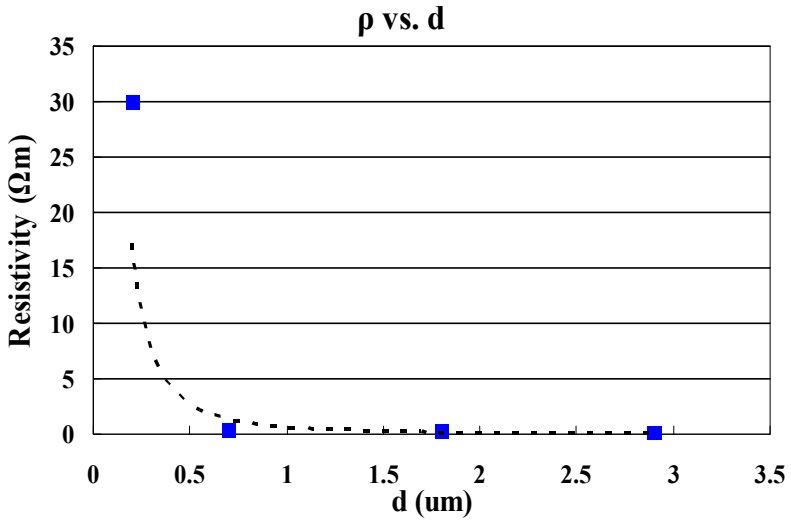

Figure 3.18: Initial resistivity (ρ) of the CNT layer as a function of CNT layer thickness (d) in the PDMS/CNTs microline.

porosity/density of the CNT layer tends to increase as the *d* increases. Therefore it results in a low resistivity since the volume fraction of the conductive path increases when ρ decreases in a CNT-loaded polymer matrix.

3.3.3.3 Interpretation of Piezoresistive Behaviors of the PDMS/CNTs Microline

The studies and results in sections 3.3.3.1 and 3.3.3.2 have shed some light on the understanding of the piezoresistive behaviors of the bi-layer PDMS/CNTs composite presented in Figure 3.13. As discussed previously, it is reasonable to speculate that all three piezoresistive mechanisms discussed in 3.3.3.1 were present and somewhat coupled when the PDMS/CNTs composite was strained, while the magnitude of each effect could be different when R_0 varied. Combining all the results, the following conclusions and explanations were then made:

1) When the R_0 of studied sensors was less than 500 KΩ (zone 1), the CNT layer thickness was found to be larger than 1μm. Since the diameter of each CNT is in the order of 50~80nm, the layer was approximately composed of at least 15 layers of CNT single layers. These layers formed a dense and interpenetrating conductive network and the CNT concentration should be well above the percolation point, as shown in Figure 3.16. As a result, it is reasonable to assume that in this R_0 region when the CNT layer is sufficiently thick, the primary piezoresistive mechanisms may be attributed to the intrinsic CNT piezoresistivity (G_i) and the dimensional change induced piezoresistivity (G_d). Since the CNT layer in this device configuration is in direct contact with the stretch frame, and the CNT network is highly entangled, the force applied to the frame through DMA can be directly transferred into the CNT network, propagate within the CNT film through the entanglement and subsequently

deform the tubes. This is opposed to the case where CNTs are embedded deep inside a polymer matrix and the interfacial strength between the CNT and the polymer is crucial to ensure sufficient load transfer from the polymer to the CNTs in order to deform the CNTs, which has been found to be difficult because the CNT has a much higher Young's modulus (~1TPa) that that of PDMS (~2MPa).

To verify the above assumption that the individual CNT was deformed under the applied strain in this region, a Raman study was conducted. Raman spectroscopy investigates the electronic structure of a material by exciting the molecules in a system using a laser with a certain wavelength. The laser incidence interacts with molecular vibrations, phonons or other excitations, and results in the energy shift of the laser photons, which provides useful information of phonon modes in the system. The Raman spectrum of a CNT usually has three most prominent singularities, termed D band, G band and 2D band. The D band involves photon scattering from a defect (e.g. porous, impurities, etc) which breaks the basic symmetry of the graphene structure in a CNT. It usually appears in the range of 1330 to 1360 cm^{-1}. The G band is closely related to vibrations in sp^2 hybridized carbon (ordered structure), and it is generally observed in the range of 1560 cm^{-1} and 1590 cm^{-1}. The 2D band is the second-order of the Raman scattering from D-band variation, and is located at the 2660 to 2720 cm^{-1} range. If the electronic structure of a CNT is altered under stress/strain, a strain dependent Raman shift can be observed[40,41,42]. The Raman spectrum therefore gives very useful information with respect to the deformation of an individual CNT. In our study, a room-temperature Raman spectroscopy apparatus with an excitation laser wavelength of 488nm was applied to a stretching stage to

which the two ends of the sample frame shown in the middle image of Figure 3.5 was tightly anchored. The controlled strain was imparted into the composite through a micrometer attached to the stage and the Raman spectrum was recoded immediately after each strain was employed. As shown in the Figure 3.19 and 3.20, both the 2D band and the G band exhibited blue shift under the increased strain, which was consistent with those reported by peers[40,41,42]. The results confirmed that the individual CNT in this case underwent deformation upon the strain/stress, which could contribute to the piezoresistivity of the composite. The gauge factor in this R_0 region (zone 1) varies from 13 to 160, which is found to be within the theoretically predicated and experimental reported values of the intrinsic piezoresistivity of a CNT as discussed in (iii) of section 3.3.3.1.

Furthermore, the higher G observed in a sample with a lower R_0 in this region is likely due to the larger stress that a thicker CNT layer experiences than the thinner

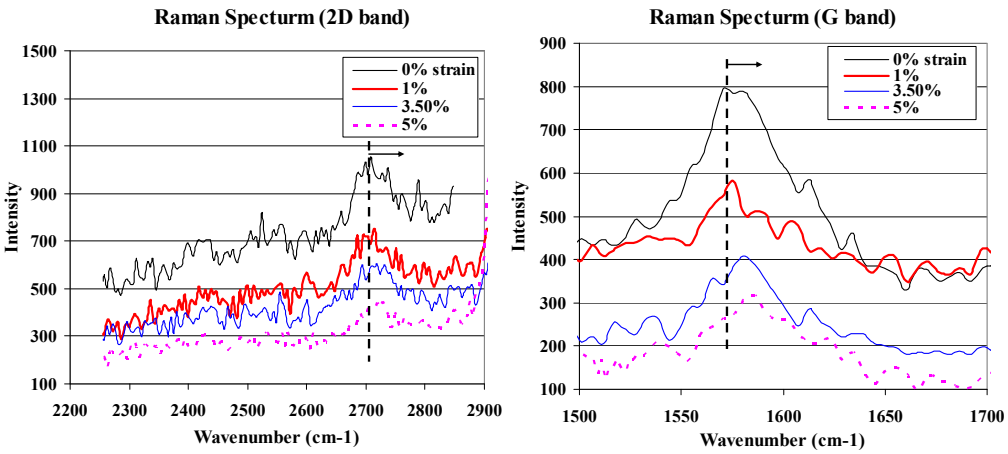

Figure 3.19: Raman shift of 2D band (left) and G band (right) of the PDMS/CNT composite under strain. (Curves have been shifted vertically for clarification.)

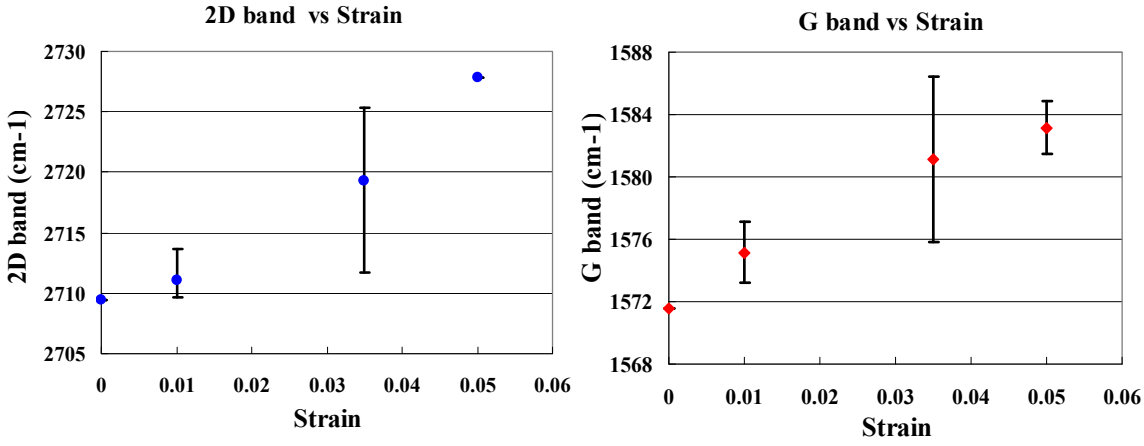

Figure 3.20: Raman shift of 2D band (left) and G band (right) of the PDMS/CNT composite under strain.

one under the same strain, and subsequently induced higher change in CNT bandgap as discussed in 3.3.3.1. As studied by Loh[43], a thicker CNT film from LBL assembly exhibited a higher Young's modulus (E_y) . Therefore under the same strain, the stress generated in a thicker CNT film is higher than that in a thinner one in accordance to the relation: stress=E_y× strain. The observed trend is again consistent with the system with intrinsic piezoresistivity induced G, in which a higher stress leads to a higher G in this effect[19,44,43]. Another observation is that a higher applied strain in this region gives rise to a higher gauge factor, which is well aligned with what has been theoretically predicted as shown in equation 3.9.

2) When the R_0 of tested devices was above 1.9MΩ (zone 2), the CNT layer thickness was found to reduce to less than 600nm. Figure 3.16 and morphology study showed that the composite in this region approached the percolation point. CNTs loosely packed with each other formed a much less entangled interpenetrating network in the PDMS matrix. In this case, the majority of the deformation under strain will likely

take place in the PDMS phase since the Young's modulus of PDMS is six orders of magnitude lower than that of the CNT. The resistance change due to the deformation of the individual CNT could therefore be much less pronounced or negligible due to the insufficient load transfer from the soft PDMS to the rigid CNT. Therefore the piezoresistivity induced by the change of tunneling resistance, G_t, may play the most important role in the device sensitivity in this R_0 region. Depending on the strain level, the gauge factor in this zone was found to be around 40~130. These values are well aligned with the theoretical modeled values as given in Figure 3.15. Opposite to the ones induced by the intrinsic piezoresistive effect as discussed in (1), the gauge factor in this region increases when R_0 increases, which is consistent with the results reported in the tunneling resistance change system as shown in ii) of 3.3.3.1. These observations then confirm that the alteration of the tunneling resistance is likely to be the primary cause for the piezoresistivity of the sensors in this region.

From the information gained through the aforementioned studies, the relationship between the gauge factor of a sensor and the CNT layer thickness could be elucidated and established, given the fact that *d* can be readily controlled through the parameters of EPD process such as applied electric field and the deposition time discussed in Chapter 2, the device sensitivity may consequently be controlled and tailored through the fabrication process parameters. These results may allow us to design a strain sensor with a desired gauge factor to meet the specific requirements for a certain application.

3.3.3.4 Hysteresis Study of the PDMS/CNTs Strain Sensor

Due to the viscoelasticity of the PDMS, the nanocomposite exhibits a certain level of hysteresis as shown in Figure 3.21, where some deviations occurred between the loading and unloading curves.

This issue is less pronounced in the lower strain region (<2.5%). Such phenomenon is common in most carbon nanotube-loaded elastomer system[45,46]. Studies of mechanical behavior of the same type of PDMS (Sylgard 184, Dow Corning) have shown that it also exhibits a small level of hysteresis[47] under strains of 5% (Figure 3.22). This hysteresis behavior is considered to arise from the energy loss during the cyclic deformation, where stretching and relaxing an elastomer incurs losses due to heating and friction from the rubbing of the crosslinked polymer molecular chains as they reorganize during elongation or contraction of the bulk polymer[48]. The hysteresis of the PDMS may be one of the factors that causes the similar hysteresis behavior in the resultant PDMS/CNTs composite. However, due to the complex nature of the nanocomposite and given the fact that hysteresis could have three sources including PDMS, CNTs, and their composite form, further investigation of the mechanisms is needed for a more accurate explanation and better understanding of the resistance-strain response in this system.

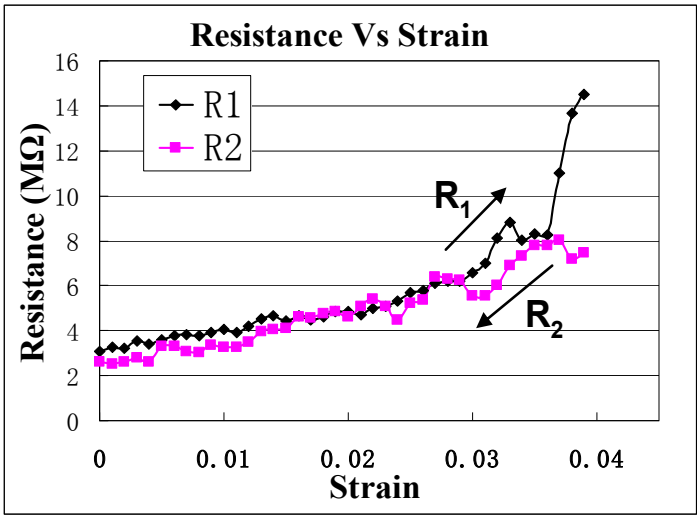

Figure 3.21: Hysteresis of the resistance response upon strain.

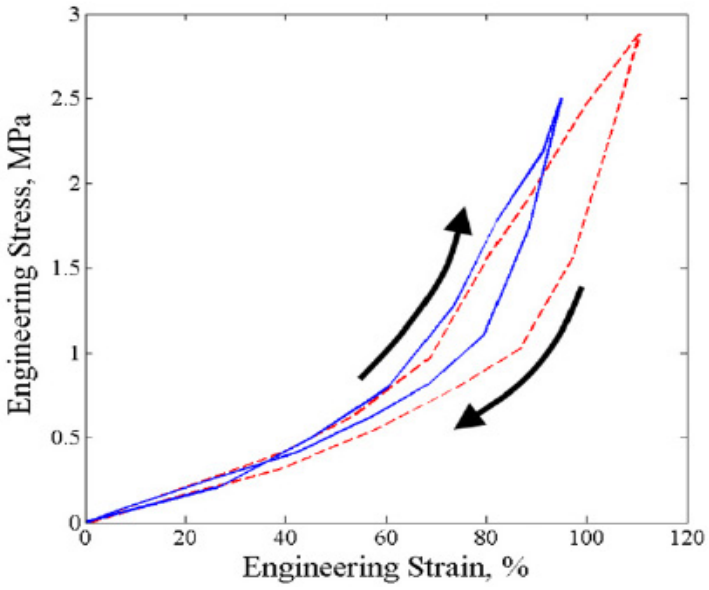

Figure 3.22: Hysteresis curves for Sylgard 184 reported by Gerratt *et al.*[47].

3.4 Summary

In this chapter, various micropatterns of CNTs on elastomeric PDMS have been successfully achieved through the combination of MEMS assisted EPD techniques and transfer micromolding process. The resultant PDMS/CNT composite exhibited a bi-layer structure which demonstrated very high sensitivity to both transverse compressive force and tensile strain. The gauge factor in the case of tensile strain sensing was found to have a strong dependence on both the initial resistance of the PDMS/CNTs composite and the applied strain, which could be attributed to the different piezoresistive mechanisms (tunneling resistance change induced piezoresistivity and intrinsic piezoresistivity of CNT) in this system. These results provide useful guidance for the design and fabrication of the strain/stress sensors with a specific sensitivity. Moreover, the PDMS/CNT bi-layer material in this study exhibits much higher or comparable strain sensitivity, compared with traditional metal foil strain sensors (G=2.1) or silicon piezoresistors (G<120), with the

additional advantage of larger working range (>10%) before device failure. The patterned PDMS/CNTs flexible composite developed in this work can be potentially utilized to sense and monitor local pressure or structural change in tissues or micro-fluidic systems, as well as flexible 3-D microsystems. In addition, comparing with conductive spherical particle loaded polymer such as polymer/carbon black (CB) composite, the polymer/CNT composite carries several preferential properties. First, the gauge factor achievable in the CNT system is much higher (up to 2000) than in the carbon black system[49] (<100). Second, the concentration of the CNT in a polymer matrix required to reach a conductive network is much lower[50](<5%) than that of the carbon black[51] (>30%) due to the advantage of the high aspect ratio cylindrical structure. Last but not least, the mechanical strength of a polymer reinforced by CNT (up to 80GPa[52,53]) outperforms the polymers reinforced by carbon black[54] (<10GPa). Therefore, though more expensive than CB, CNT can be utilized more efficiently and has great potential for the next generation of lightweight and high performance flexible/conformal devices.

3.5 References

(1) Yang, L.; Chakrabartty, S.; Gkinosatis, D. S.; Mohanty, A. K.; Lajnef, N. Biomedical Circuits and Systems Conference, 2007. BIOCAS 2007. IEEE, 2007; p 119.

(2) White N.; A. C. *Microelectronics International* **1987**, *4*, 32.

(3) Alpuim, P.; Costa, C. *Journal of Non-crystalline Solids* **2008**, *354*, 2585.

(4) Nakamura, K.; Isono, Y.; Toriyama, T.; Sugiyama, S. *Physical Review B* **2009**, *80*, 045205.

(5) Pollak, F. H.; Cardona, M. *Physical Review* **1968**, *172*, 816.

(6) Hwang, E.-S.; Kim, Y.J.; Ju, B.K. *Sensors and Actuators A: Physical* **2004**, *111*, 135.

(7) Kanda, Y.; *Electron Devices, IEEE Transactions on* **1982**, *29*, 64.

(8) Blazewicz, S.; Patalita, B.; Touzain, P. *Carbon* **1997**, *35*, 1613.

(9) Han, B.; Ou, J. *Sensors and Actuators A: Physical* **2007**, *138*, 294.

(10) Aiyar, A. R.; Song, C., Kim, S.H.; Allen, M.G. *Smart Materials and Structures* **2009**, *18*, 115002.

(11) Bloor, D. D., K; Hands, P. J.; Laughlin, P.; Lussey, D. *Journal of Physics D: Applied Physics* **2005**, *18*, 2851.

(12) Radhakrishnan, S.; Chakne, S.; Shelke, P. N. *Materials Letters* **1994**, *18*, 358.

(13) Hu, N.; Karube, Y.; Arai, M.; Watanabe, T.; Yan, C.; Li, Y.; Liu, Y.; Fukunaga, H. *Carbon* **2010**, *48*, 680.

(14) Stampfer, C.; Helbling, T.; Obergfell, D.; Schöberle, B.; Tripp, M. K.; Jungen, A.; Roth, S.; Bright, V. M.; Hierold, C. *Nano Letters* **2006**, *6*, 233.

(15) Tabib-Azar, M.; Run, W.; Yan, X.; Liang, Y. Nano/Micro Engineered and Molecular Systems, 2006. NEMS '06. 1st IEEE International Conference on, 2006; p 1297.

(16) Minot, E. D.; Yaish, Y.; Sazonova, V.; Park, J.-Y.; Brink, M.; McEuen, P. L. *Physical Review Letters* **2003**, *90*, 156401.

(17) Cao, J.; Wang, Q.; Dai, H. *Physical Review Letters* **2003**, *90*, 157601.

(18) Nalwa, H. S. *Nanostructured Materials and Nanotechnology*; Academic Press: San Diego, 2002.

(19) Lee, K.; Lee, S. S.; Lee, J. A.; Lee, K. C.; Ji, S. *Applied Physics Letters* **2010**, *96*.

(20) Loh, J. K.; Lynch, J.P.; Kam, N.W.S.;Kotov, A.N. *Smart Materials and Structures* **2007**, *16*, 429.

(21) Ciselli, P.; Busfield,J.C.; Peijs, T.; *E-Polymers* **2010**, 014.

(22) Murugaraj, P.; Mainwaring, D. E.; Mora-Huertas, N. *Composites Science and Technology* **2009**, *69*, 2454.

(23) Knite, M. O.; K.; Zavickis, J.; Tupureina, V.; Klemenoks, I.; Orlovs, R *Journal of Nanoscience and Nanotechnology* **2009**, *9*, 3587.

(24) Kang, I.; Kim, J. *Smart Mater. Struct.* **2006**, *15*, 737.

(25) Liu, C. X.; Choi, J. W. *Journal of Micromechanics and Microengineering* **2009**, *19*.

(26) Sekitani, T.; Noguchi, Y.; Hata, K.; Fukushima, T.; Aida, T.; Someya, T. *Science* **2008**, *321*, 1468.

(27) Tambe, N. S.; Bhushan, B. *Ultramicroscopy* **2005**, *105*, 238.

(28) Olek, M.; Ostrander, J.; Jurga, S.; Möhwald, H.; Kotov, N.; Kempa, K.; Giersig, M. *Nano Letters* **2004**, *4*, 1889.

(29) Dang, Z. M.; Xie, D.; Yao, S.H.; Zhang, L.Q.; Bai, J. *J. Appl. Phys.* **2008**, *104*, 024114

(30) Kang, J. H.; Park, C.; Scholl, J. A.; Brazin, A. H.; Holloway, N. M.; High, J. W.; Lowther, S. E.; Harrison, J. S. *Journal of Polymer Science Part B-Polymer Physics* **2009**, *47*, 994.

(31) Ezquerra, T. A.; Kulescza, M.; Cruz, C. S.; Baltá-Calleja, F. J. *Advanced Materials* **1990**, *2*, 597.

(32) Simmons, J. G. *J Appl Phys* **1963**, *34*, 1793.

(33) Dawson, J. C.; Adkins, C. J. *Journal of Physics-Condensed Matter* **1996**, *8*, 8321.

(34) Du, F. M.; Scogna, R. C.; Zhou, W.; Brand, S.; Fischer, J. E.; Winey, K. I. *Macromolecules* **2004**, *37*, 9048.

(35) Adkins, C. J. *Journal of Physics-Condensed Matter* **1989**, *1*, 1253.

(36) Bautista-Quijano, J. R.; Aviles, F.; Aguilar, J. O.; Tapia, A. *Sensors and Actuators a-Physical* **2010**, *159*, 135.

(37) Gau, C.; Ko, H. S.; Chen, H. T. *Nanotechnology* **2009**, *20*.

(38) O'Connell., M. J. *Carbon Nanotubes. Properties and Applications*; CRC Press, 2006.

(39) Woo, C. S.; Lim, C. H.; Cho, C. W.; Park, B.; Ju, H.; Min, D. H.; Lee, C. J.; Lee, S. B. *Microelectronic Engineering* **2007**, *84*, 1610.

(40) Schadler, L. S.; Giannaris, S. C.; Ajayan, P. M. *Applied Physics Letters* **1998**, *73*, 3842.

(41) Qiu, W.; Kang, Y. L.; Lei, Z. K.; Qin, Q. H.; Li, Q.; Wang, Q. A. *Journal of Raman Spectroscopy* **2010**, *41*, 1216.

(42) Barone, P. W.; Yoon, H.; Ortiz-Garcia, R.; Zhang, J. Q.; Ahn, J. H.; Kim, J. H.; Strano, M. S. *Acs Nano* **2009**, *3*, 3869.

(43) Loh, K. J. Ph.D. Thesis, University of Michigan, 2008.

(44) Song, X. H.; Liu, S.; Gan, Z. Y.; Lv, Q.; Cao, H.; Yan, H. *Microelectronic Engineering* **2009**, *86*, 2330.

(45) Liu, C. X.; Choi, J. W. *Ieee Transactions on Nanotechnology* **2010**, *9*, 590.

(46) Ci, L.; Suhr, J.; Pushparaj, V.; Zhang, X.; Ajayan, P. M. *Nano Letters* **2008**, *8*, 2762.

(47) Gerratt, A. P.; Penskiy, I.; Bergbreiter, S. *Journal of Micromechanics and Microengineering* **2010**, *20*.

(48) Khanna, Y. P.; Turi, E. A.; Taylor, T. J.; Vickroy, V. V.; Abbott, R. F. *Macromolecules* **1985**, *18*, 1302.

(49) Gammelgaard, L.; Rasmussen, P. A.; Calleja, M.; Vettiger, P.; Boisen, A. *Applied Physics Letters* **2006**, *88*.

(50) Huang, Y. Y.; Terentjev, E. M. *Advanced Functional Materials* **2010**, *20*, 4062.

(51) Cao, Q.; Song, Y. H.; Tan, Y. Q.; Zheng, Q. A. *Carbon* **2010**, *48*, 4268.

(52) Dalton, A. B.; Collins, S.; Munoz, E.; Razal, J. M.; Ebron, V. H.; Ferraris, J. P.; Coleman, J. N.; Kim, B. G.; Baughman, R. H. *Nature* **2003**, *423*, 703.

(53) Miaudet, P.; Badaire, S.; Maugey, M.; Derré, A.; Pichot, V.; Launois, P.; Poulin, P.; Zakri, C. *Nano Letters* **2005**, *5*, 2212.

(54) Adohi, B. J. P.; Mdarhri, A.; Prunier, C.; Haidar, B.; Brosseau, C. *Journal of Applied Physics* **2010**, *108*.

CHAPTER 4

MICROPATTERNABLE ELASTIC PDMS/CNTs ELECTRETS

4.1 Electret Materials

An electret is a dielectric which exhibits quasi-permanent electric charge or dipole moment. The quasi-permanent internal or external electric fields created by electrets can be exploited in multiple applications such as microphones, copy machines, micro power generators, sensors/actuators, micro fluidic devices, air filters, biomedical implants, and organic field effect transistor memories[1,2,3.4].

Based on the charge storage mechanism, electrets can be approximately classified into four types, as summarized in Table 4.1. The first type is a real-charge electret which traps excess charges with one or both polarities on its surface or within its volume owing to its high bulk resistivity. The second type is oriented-dipole electrets, where the molecules are capable of forming aligned dipoles that lead to an overall dipole moment. The third/fourth type is composite/cellular space charge electrets, where the internal bipolar charges reside at the interface of the two phases or in the voids within the electret. Some dielectric materials are capable of possessing two or more types of charge storage mechanisms.

Free excess charges are generally introduced into an electret through a charge transfer process such as corona charging, soft X-ray, vacuum UV, contact charging or electrification. These free charges usually concentrate either on the top surface or several micrometers below the electret surface, and decay exponentially. The decay constant is a

function of the material's relative dielectric constant and its bulk resistivity[5]. Materials with extremely high bulk resistivity such as Teflon AF® (Polytetrafluoroethylene) may retain excess charge for hundreds of years. On the other hand, the dipole moment in an electret is produced from aligning the dipoles of electret molecules under a very high electric field with the temperature above its glass transition temperature ((T_g). The oriented dipoles relax notably when the temperature is above T_g during usage; therefore, a dielectric with a high T_g is preferred for this type of electret.

Table 4.1 Types of Electrets[6,7,8,9]

Electret material	Dominant charge storage mechanism	Charge density ($mC\ m^{-2}$)	Young`s modulus (GPa)	Piezoelectric coefficient (pC/N)
non-polar polymers (Teflon, PE,PP)	space/bulk charge	<6 (0.5 for Teflon AF®)	1-3	0.1-1.0
polar Polymers (CYTOP®, Parylene)	dipole moment	<63 (1.37, 3.69)	2-4	0.1-3.0
SiO_2/SiN_x	Interface Dipolar charge	11.5	40-70/ 100-300	N/A
porous polymer (cellular PP, PTFE)	charges in the interface of the voids	<2.1	6×10^{-6}-1×10^{-3}	<300

Traditional electret materials such as silicon dioxide/silicon nitride, and thin film fluoropolymers such as Teflon AF® and CYTOP® (amorphous fluoropolymer), possess key electret properties of high surface charge density and long-term charge stability. For

instance, H. Amjadi studied a negatively charged SiO_2/SiN_x double layer that exhibited charge retention capability of over three years when properly stored in a box[10]. However, fabrication of SiO_2/SiN_x electrets usually requires a high processing temperature[10] (>300 °C). Furthermore, the electret film produced from these materials is rigid and brittle with a high Young's modulus of over 40 GPa, which may limit its applicability in flexible devices. Teflon holds excellent charge stability, yet it only has limited solubility in very few fluorinated solvents, which makes it difficult to be processed into thin films and results in a lack of compatibility with MEMS processes[11]. CYTOP® is one of the state-of-art electrets that can be spin coated and has demonstrated a surface charge density of 1.3 mC/m^2 and good charge storage stability for over 4000 hours[12]. Yet both of the Teflon and CYTOP® have relatively high Young's modulus of 0.5 GPa and 1.2 GPa respectively[13]. It is therefore still a challenge to deploy those materials in applications requiring good micropatternability, low processing temperature, and mechanical flexibility/elasticity all at the same time.

Patterns of electrostatic charges in an electret, on the other hand, have been used in conventional xerography and can serve as templates to induce self-assembly and patterning of DNA, proteins and nanoparticles[14,15]. Moreover, micropatternable electrets can enable some specific applications in MEMS such as electrostatic motors, non-contact electrostatic micro-bearings, and micro power generators [8,12, 16,17]. For example, Kasagi *et al.* has reported the utilization of a patterned perfluorinated polymer electret in vibration-induced power generation by varying the total overlap area between the patterned electret and the counter electrode[12].

Squeezable/elastic electrets may open new applications, such as skin-like energy

harvesters that could be pervasively integrated into existing electronic systems and tap low frequency vibrations. Such vibration resulting from human or object motion could provide power for, for example, portable electronics when a person is walking/jogging[18]. Most traditional inorganic or polymeric electrets have a relatively high E_y, typically in the range of 1-100GPa. Elastomeric materials have a much lower E_y, typically several MPa. In addition, the use of an elastomer in electrets can enhance piezoelectric transduction. The equivalent piezoelectric coefficient of an electret, d_{33}, can be determined by the following equation[6]:

$$d_{33} = 2\eta\sigma_s / E_y \tag{4.1}$$

where σ_s is the surface charge density of the material and η is a material constant that depends on the material properties such as permittivity. Therefore, a lower E_y can lead to a higher d_{33}. As illustrated in Table 4.1, cellular polymeric electrets with a low E_y exhibit much higher equivalent d_{33} than those with higher E_y. However, elastomers are non-electrets in most cases, partially because of their low glass transition temperature (T_g) which is well below room temperature. A low T_g can cause the relaxation of the dipole alignment of an electret after charging. Introduction of air voids into a polymer electret film is one strategy to reduce the overall E_y and endow it with the elastic-like behavior, which is appealing for both sensor and actuator applications[15,18].

4.2 Electret Power Generators

Electrets can be utilized in fixed-charge variable capacitance devices, and therefore vibration energy harvesting based on this material has received considerable

attention in recently years. Placing a charged electret film in parallel with a counter electrode gives rise to a capacitor structure with a permanent built-in electric field. Modification of the capacitor geometry, and therefore its capacitance, by mechanical force creates an alternating displacement current which provides useful electrical power for the external circuit. Differing from other types of power generators such as electromagnetic or electrostatic energy harvesters, an electret power generator carries a permanent build-in electric field. The permanent charges presented in an electret may eliminate the overhead required by other types of electrostatic power generators.

In general, electret power generators can be classified into three types of configurations, as illustrated in Figure 4.1.

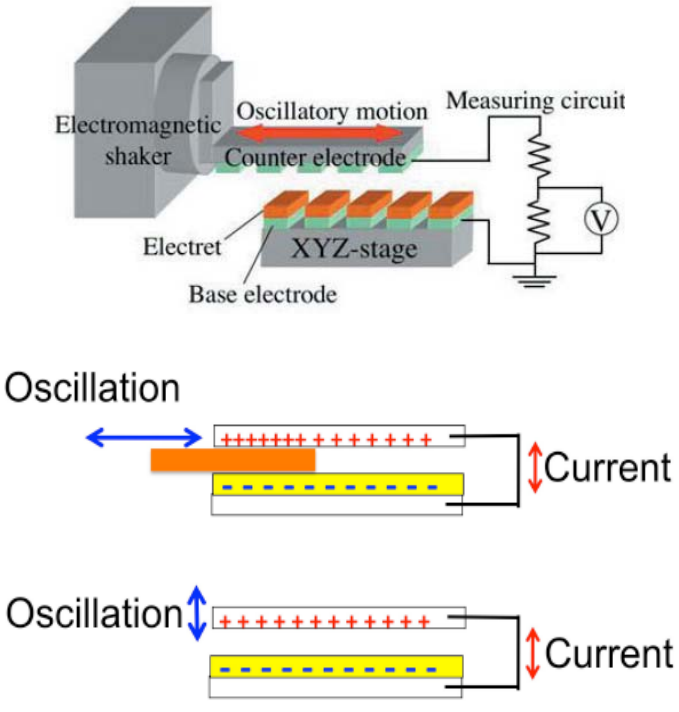

Figure 4.1: Different configurations of electret power generators. (Top: in-plane with variable overlapping area[19], Middle: in-plane with oscillating dielectric[20], and bottom: out-of-plane with variable gap distance[20].

4.2.1 In-plane Electret Power Generator with Variable Overlap Area

In this device configuration, a counter electrode oscillates above the patterned electret, leading to a variation of the total overlap area between the two (Top image in Figure 4.1). The capacitance of the device, *C(t)*, is:

$$C(t) = \frac{\varepsilon_0 \cdot A(t)}{g} \tag{4.2}$$

where *g* is gap of the capacitor, *A(t)* is the overlapping area, and ε_0 is the permittivity of the air. The capacitance response to the variation of the overlapping area is described as:

$$\frac{\partial C(t)}{\partial t} = \frac{\varepsilon_0}{g} \cdot \frac{\partial A(t)}{\partial t} \tag{4.3}$$

The equation indicates a linear relation between the change of the capacitance and overlap area. When placing a charged electret on a stationary electrode in the power generator, mirror charges are induced on the counter and stationary electrode. If the overlap area between the counter electrode and the electret is zero, all charges reside on the stationary electrode. When the counter electrode oscillates in-plane over the electret and overlaps with it, charges are induced in the counter electrode and the resultant displacement current flows through the external load. The generated voltage (*V(t)*) across the two electrodes changes with time as the counter electrode oscillates, which leads to power generation. From equation 4.2 and 4.3, *V(t)* can be described as[21]:

$$V(t) = \left(\frac{-d}{\varepsilon_r \varepsilon_0}\right)\sigma_s + \left(\frac{d}{\varepsilon_r \varepsilon_0} + \frac{g}{\varepsilon_0}\right)\frac{Q(t)}{A(t)} \tag{4.4}$$

$$Q(t) = \frac{\int \frac{d\sigma_s}{R\varepsilon_r\varepsilon_0} e^{\int\left[\left(\frac{d}{\varepsilon_r\varepsilon_0}+\frac{g}{\varepsilon_0}\right)\frac{1}{RA(t)}\right]dt} dt + C}{\exp(\int\left[\left(\frac{d}{\varepsilon_r\varepsilon_0}+\frac{g}{\varepsilon_0}\right)\frac{1}{RA(t)}\right]dt)} \tag{4.5}$$

where d is the thickness of the electret , $Q(t)$ is the total mirror charge created on the counter electrode, ε_r is the permittivity of the electret. R is the load, and C is an arbitrary constant.

The power generator based on this configuration can work at very low frequency as long as the relative motional force can break the frictional force induced by the attractive electrostatic force between the electret charges and their image charges on the counter electrode. It is the most widely studied and exploited architecture of electret power generators due to its capability to achieve relatively large change of overlap area, which gives rise to a high power output up to the mW range [8,12, 16,17]. However, in this design, it is challenging to achieve a spring system with both low-resonant-frequency that enables large in-plane amplitude and large out-of-plane spring constant in order to avoid stiction between electrets and electrodes generated from the electrostatic force [20]. Also this configuration requires an air-gap between the electret and the counter electrode, yet the need for gap-controlling structures often complicates the design and fabrication of the device[8].

4.2.2 In-plane Electret Power Generator with Variable Gap Permittivity

The second configuration, as shown in the middle illustration of Figure 4.1, is a capacitor with a dielectric material that oscillates inside the air gap between the immobilized charged electret and the counter electrode. The permittivity of the capacitor

alters accordingly which changes the strength of the electric field within the charged capacitor structure. As a result, mirror charges are induced in the counter electrode. Similarly, the capacitance change in this configuration can be calculated as:

$$\frac{\partial C(t)}{\partial t} = \frac{A}{g}\frac{\partial \varepsilon(t)}{\partial t} \tag{4.6}$$

C (t) exhibits a linear relationship with the modification of the permittivity. When the air gap is completely empty, the capacitor has an induced voltage (V_0) of

$$V_0 = \frac{Qg}{\varepsilon_0 A} \tag{4.7}$$

where Q is the total charge on the electret. When the dielectric material fully occupies the gap, the voltage becomes

$$V_{\lambda/2} = \frac{Qg}{\varepsilon_0 \varepsilon_r A} \tag{4.8}$$

where ε_r is the permittivity of the dielectric material, λ/2 represents half a period of oscillation. The AC voltage of this generator will then have an open-circuit peak-to-peak voltage of

$$V_{p-p} = \frac{Qg}{\varepsilon_0 A}\left(1 - \frac{1}{\varepsilon_r}\right) \tag{4.9}$$

The potential between the two output electrodes changes in time proportionally to the permittivity of the air gap. If a flowing liquid such as water serves as the oscillating dielectric, this configuration can potentially eliminate the need for the shaker required to

drive the counter electrodes in the previous configuration[8, 21]. However, an appropriate design of an extra component to drive the dielectric material in and out of the air gap adds additional complexity to the device. The periodic oscillation of a material inside the capacitor gap may wear the device, and good control over the horizontal movement of the dielectric inside the micro-scale gap may also be very challenging.

4.2.3 Out-of-plane Electret Power Generator with Variable Gap Distance

The third configuration of the electret energy harvester is the capacitor with variable gap distance (Bottom image in Figure 4.1). An electret microphone and electret impact sensor are similar well known devices for converting pressure waves into electrical signals by varying the distance between a charged electret and the counter electrode. Similar to the above-mentioned two types, the voltage output, *V(t),* of this structure can be described as:

$$V(t) = \left[\frac{g(t)}{\varepsilon_{r(gap)} \varepsilon_0 A} + \frac{d}{\varepsilon_r \varepsilon_0 A} \right] Q(t) - \frac{\sigma_s d}{\varepsilon_r \varepsilon_0} \tag{4.10}$$

$$Q(t) = \frac{-\int \frac{d \cdot \sigma}{R \varepsilon_r \varepsilon_0} \cdot e^{\int -\left[\left(\frac{d}{\varepsilon_r} + \frac{g}{\varepsilon_{r-gap}} \right) \frac{1}{\varepsilon_0 \cdot R \cdot A(t)} \right] dt} dt + C}{\exp\left(\int -\left[\left(\frac{d}{\varepsilon_r} + \frac{g}{\varepsilon_{r-gap}} \right) \frac{1}{\varepsilon_0 \cdot R \cdot A(t)} \right] dt \right)} \tag{4.11}$$

where $\varepsilon_{r\text{-}gap}$ is the permittivity of gap material. When the electret thickness is orders of magnitude lower than the gap of the capacitor, *d* can be approximated to be zero, *V(t)* then becomes:

$$V(t) = \frac{\sigma_s}{\varepsilon_0 \varepsilon_{r-gap}} \cdot g(t) \tag{4.12}$$

Therefore, the voltage output changes linearly with the variation of the gap. This configuration carries device simplicity and can conveniently tap compressive mechanical energy. Nevertheless it has not yet been widely utilized as a power generator up to date because the maximum capacitance change achievable with this structure is greatly constrained by the displacement range that a support structure can allow, which needs to be large and flexible in order to compete with other two configurations[21].

So far, the gap material utilized in this system is limited to be air in a majority of reported MEMS electret power generators. If a highly compliant material such as cellular polymer film or an elastomer is utilized as the gap material instead of air, the displacement of the material (Δg) for a given mechanical force (F) is given by:

$$\Delta g = \frac{F \cdot g_0}{A \cdot E_y} \tag{4.13}$$

where g_0 is the initial gap distance. From Equation 4.12 and 4.13, a lower E_y can lead to a higher Δg under the same mechanical load, which may result in a higher voltage output for this type of power generator. This configuration with a highly deformable capacitor is extremely attractive in applications of tapping low frequency energy occurred during human walking or car running, where the periodic compressive force is the primary energy source to induce the alternation in the physical structure of a capacitor.

4.3 PDMS/CNTs Composite as an Electret

As discussed in Chapter 3, the PDMS/CNT nanocomposite fabricated through

MEMS assisted electrophoretic deposition (EPD) and the subsequent transfer micromolding process exhibits a sandwich structure, with a conductive CNT layer embedded between two dielectric layers of PDMS (Figure 3.4). Figure 4.2a showed the top surface of the CNT-bearing side of the resultant PDMS/CNTs composite. From the region in the image where the topmost PDMS film was torn, it could be seen that the CNT layer is sealed underneath an ultra thin film of PDMS as indicated by the arrows. Meanwhile each individual CNT is well encapsulated by PDMS, as shown in Figure 4.2b. This specially-constructed bilayer architecture is intrigueing our interest because it may lead to a composite material which is suitable for elastic electret formation. PDMS is an elastic, low cost, micropatternable, easily processible and bio-compatible insulator with a low Young's modulus of 1-5 MPa and a high

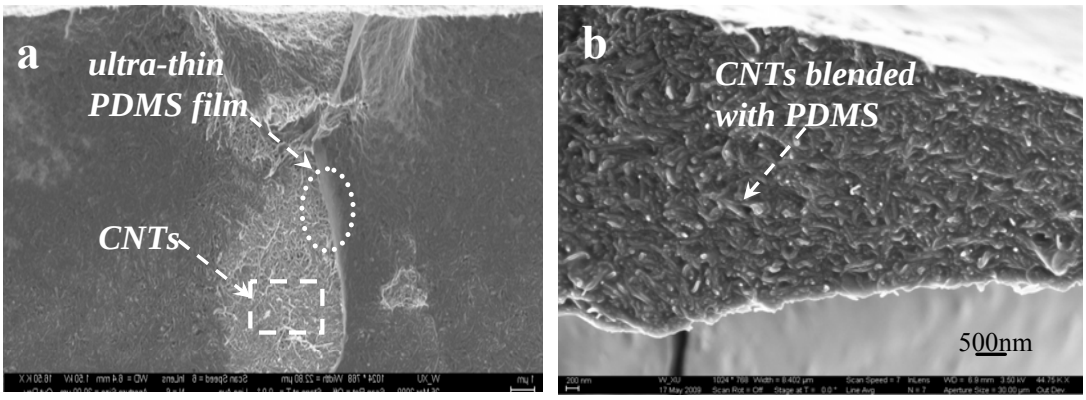

Figure 4.2: SEM image of (a) top surface of the PDMS/CNTs nanocomposite, and (b) inner CNT layer.

dielectric strength of 20kV/mm. Studies have shown that a distorted carbon nanotube and CNT interpenetrating network can trap charges at the strained CNT sites[22]. In addition, CNTs bearing defects or absorbing molecules such as water and ammonia exhibit charge

trapping capability [23,24,25] as well. Through the fabrication technique developed in Chapter 2, this nanomaterial with charge storage ability can be micropatterned at room temperature. Though the electret characteristics of both materials have not yet been reported, the micropatternable PDMS/CNTs nanocomposite combines these two non-electret materials into a structure that may trap/store charges as illustrated in Figure 4.3, allowing its potential utilization as a micropatternable and squeezable/elastic electret. When free charges with sufficient kinetic energy are injected into the topmost surface of the PDMS/CNTs composite, they may penetrate the top ultra-thin PDMS film and reach the CNT layer. It has been shown that an electron injected into a Teflon film by Corona charging with an energy of 8 keV has a penetration depth of 0.6μm[26]. Therefore it is reasonable to assume that the electrons/ions generated by a corona charging process with a potential of higher than 8 keV are capable of penetrating a 10-nm thick PDMS film that has a lower density (1.03 g/cm^3) than Teflon (~2g/cm^3). Since CNTs have charge trapping ability[12], these injected charges can potentially be captured by CNTs and reside either in the PDMS-CNT interface or within the CNT. As PDMS is a dielectric material,

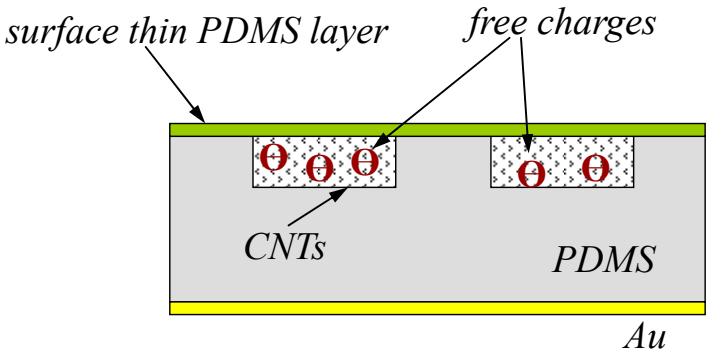

Figure 4.3: Possible charge storage mechanism of the elastic PDMS/CNT nanocomposite.

the embedded charges may not be able to migrate back to the composite surface and recombine with the particles/molecules in the ambient environment. Therefore, the PDMS/CNTs bi-layer structure may be a good candidate to realize the micropatternable elastic electret bearing the advantages discussed in 4.1.

Furthermore, if this composite material proves to preserve charges like an electret, it can be conveniently configured and implemented into the out-of-plane electret power generator discussed in 4.2.3. The elastic PDMS with low Young's modulus can serve as the gap dielectric material in the capacitor, which eliminates the need for complicated spring or support structures in this type of the device and greatly simplifies the fabrication process. Meanwhile the top CNT layer where the charges reside can serve as the electret layer and create a permanent built-in electric field. Since this composite can be easily patterned and scaled up to the macro size, an energy harvester based on this material is likely to enable a large area electret energy scavenging system.

To verify the above speculations and prove the feasibility of the elastic PDMS/CNT composite being utilized as an electret, the PDMS/CNTs nanocomposite with micropatterns was fabricated through the combination of MEMS assisted EPD techniques and the transfer micromolding process developed in Chapter 3. Corona charging was exploited to implant charges into the composite and the charge storage capability was evaluated. A power generator based on this elastic material was designed, tested and characterized as well.

4.4 Development of the Micropatterned Elastic PDMS/CNT Composite

4.4.1 Material Development

Figure 4.4 depicts the fabrication process of the proposed electret material. The CNT micropatterns on an elastic PDMS matrix were fabricated through the two-step EPD and micromolding process developed and discussed in 2.2.2 in Chapter 2. A gold layer was further evaporated onto the non-CNT-bearing side of the PDMS film, serving as the backside electrode for the electret where the compensation charges may reside (Figure 4.4c). Detailed morphology and micropatternability studies on the resultant PDMS/CNTs composite have been given previously in 2.2.2 and 3.3.1.

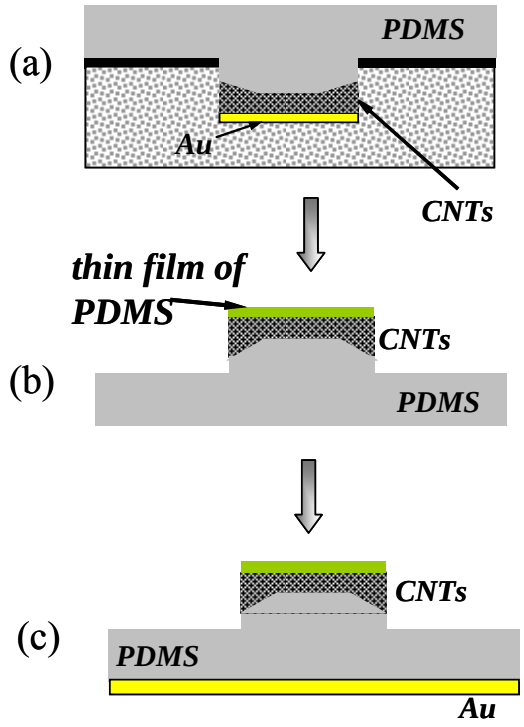

Figure 4.4: Scheme of the fabrication process for elastic Au/PDMS/CNT composite: (a) molding of micropatterned CNTs, (b) transfer micromolding of CNT micropattern, and (c) deposition of gold backside electrode.

4.4.2 Investigation of the Electret-like Behavior of the Composite

4.4.2.1 Corona Charging

Negative charges were implanted into the sample films with a point-to-plane corona discharge method (Figure 4.5). The sample was placed on a grounded metal plate with the CNT-bearing side facing upwards under a stainless steel needle electrode. To maintain consistency across all materials investigated, the charging apparatus was placed

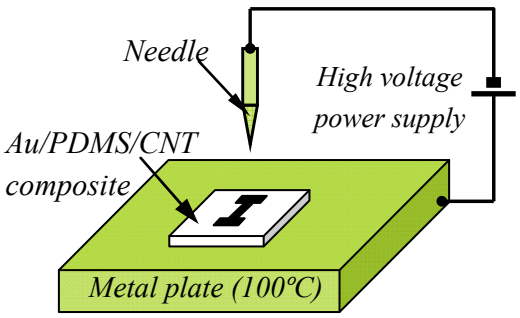

Figure 4.5: Schematic of the corona charging apparatus.

inside an oven and heated to 100ºC. The distance between the tip of the needle and the grounded plate was maintained at 15cm. In this study, when the sample size is larger than 1 cm^2, a metal wire mesh grid was inserted and suspended 15mm above the sample surface to ensure a uniform distribution of the surface charge. A voltage of -2500V was applied to the mesh during the charging process. For small samples, no grid was exploited in order to achieve a high charging voltage. A constant voltage of -10kV was applied to the needle electrode to create the charged molecules, since, the electrons under this charging voltage have sufficient kinetic energy to penetrate the topmost 10 nm-thick ultra thin PDMS films and reach the CNT layer[26]. The charging process will stop when the surface voltage of the sample reaches that of the needle tip or grid. The surface charge density of the material was measured as a function of time and it was found that the

surface charge density increased initially and reached to a constant value after half-hour. Therefore, the charging time in this study for all the samples was set to be 30 minutes. Afterwards, the sample was first allowed to cool down to room temperature before the voltage was turned off. The decay of the surface charge density of the sample was investigated by a surface potential voltmeter (Surface DC Voltmeter model SVM2, *AlphaLab Inc.*) and its details will be given in discussion in section 4.5. SEM imaging was performed both before and immediately after the corona charging.

4.4.2.2 SEM Imaging of the Charged/Uncharged Samples

Compared with the uncharged PDMS/CNT composite (Figure 4.6a), the SEM image of the charged composite shows image distortion and interference (Figure 4.6b).

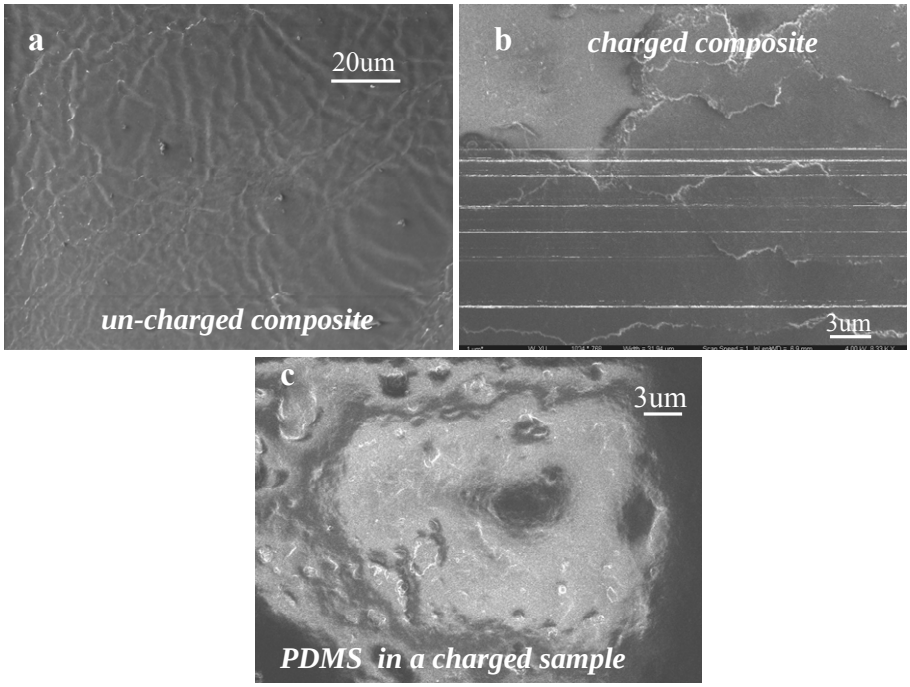

Figure 4.6: SEM image of (a) uncharged PDMS/CNT composite (b) charged PDMS/CNT composite and (c) region with pure PDMS in a charged sample.

This likely represents the interaction of the charges in the electret after charging with the SEM electrons[8], qualitatively demonstrating successful charge implantation into the material. Further imaging on the region composed of the pure PDMS in a charged sample shows no such phenomenon (Figure 4.6c), which may indicate much more rapid decay/relaxation of the charge/dipole alignment in the pure PDMS phase than that in the PDMS/CNT composite region. This will be investigated in detail later.

4.5 Study of Charge Storage Stability

To elucidate the charge storage mechanism of this electret composed of two non-traditional materials, three reference samples were investigated in parallel for comparison as illustrated in Figure 4.7. The samples comprised PDMS with no CNTs, PDMS with a cast CNT layer as opposed to an embedded/molded layer (PDMS/cast-CNTs), and a gold layer sandwiched between a thin film of PDMS and a bulk PDMS layer (PDMS/Au/PDMS). These were fabricated and charged under the same corona charging conditions as the original PDMS/CNT composite. In addition, in order to compare the performance of the composite with the traditional electrets, a 300 μm-thick Teflon film was charged using the same corona charging apparatus. The surface charge stability of all five samples was then measured and characterized as a function of time by using the aforementioned surface potential voltmeter. The surface charge density was calculated by the following equation:

$$\begin{aligned} \sigma_s &= V_{displayed} \times 3.6 \times 10^{-14} \times \frac{f}{f-1} \\ f &= \sqrt{1 + D^2 \big/ 4L^2} \end{aligned} . \qquad (4.14)$$

where σ_s is the surface charge density (ampsec/cm^2), $V_{displayed}$ is the reading from the voltmeter (Volts), D is diameter of the sample and L is the distance between the sensor disk to the top surface of the sample.

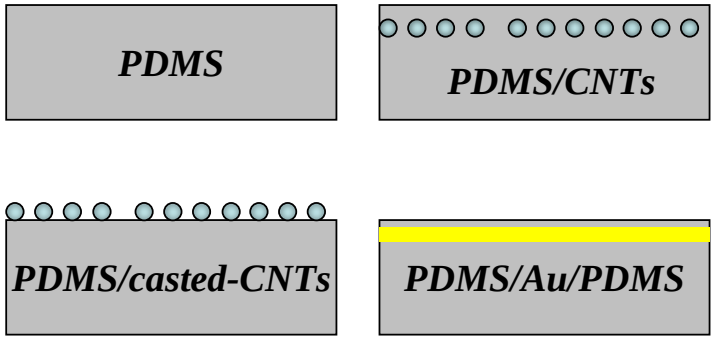

Figure 4.7: Scheme of the composite and reference samples.

The PDMS/CNT composite and the Teflon exhibited much higher initial surface charge density than the other three reference samples as listed in Table 4.2. The surface charge density of the Teflon obtained here (1×10^{-5} C/m^2)in our study is an order of magnitude lower than the highest value (i.e. $5x10^{-4}$ C/m^2) reported by other peers[27], which may arise from suboptimal charging conditions, variation in ambient environment, or the test sample.

As shown in Figure 4.8, the surface charge density (Q/A) of the PDMS/CNT composite underwent a sharp drop to 26% of its initial value within the first 30 min after charging, and then exhibited a relatively stable plateau, at approximately 5% of the initial value, for the ensuing measurement duration of 280 hours. Relative to the PDMS/CNT composite, the three reference samples all exhibited much faster decay of the surface

charge density, no stable plateau, and complete charge exhaustion in less than 5 hours (bottom graph in Figure 4.8).

Table 4.2 Initial Surface Charge Density

Sample	PDMS/CNTs	PDMS	PDMS/ casted-CNTs	PDMS/ Au/ PDMS	Teflon
Initial surface charge density(C/m^2)	4×10^{-5}	3×10^{-6}	3×10^{-7}	6×10^{-7}	1×10^{-5}

These observations support the following conclusions:

(1) The charges injected into the pure PDMS are unstable and tend to dissipate within a short period of time, which is consistent with the results reported by Nguyen[28] *et al.*;

(2) Pure CNTs without being encapsulated by a PDMS dielectric layer could not store charges for an extended time either;

(3) The charge retention capacity of the CNTs embedded in the PDMS may not be due only to the conductivity of the CNT since the sample with a gold layer as the charge trapping layer did not exhibit stable charge storage. Distorted carbon nanotubes and CNT interpenetrating network could trap charges at the strained CNT sites[22]. CNTs bearing defects or absorbing molecules such as water and ammonia exhibit charge trapping capability [23,24,25] as well. Gold nanoparticles were also found to carry charge trapping ability due to the particle charging[29]. Yet in the evaporated gold layer investigated in this study, these three trapping mechanisms presented in CNTs and gold nanoparticles are likely absent and a rapid charge decay was thereby observed.

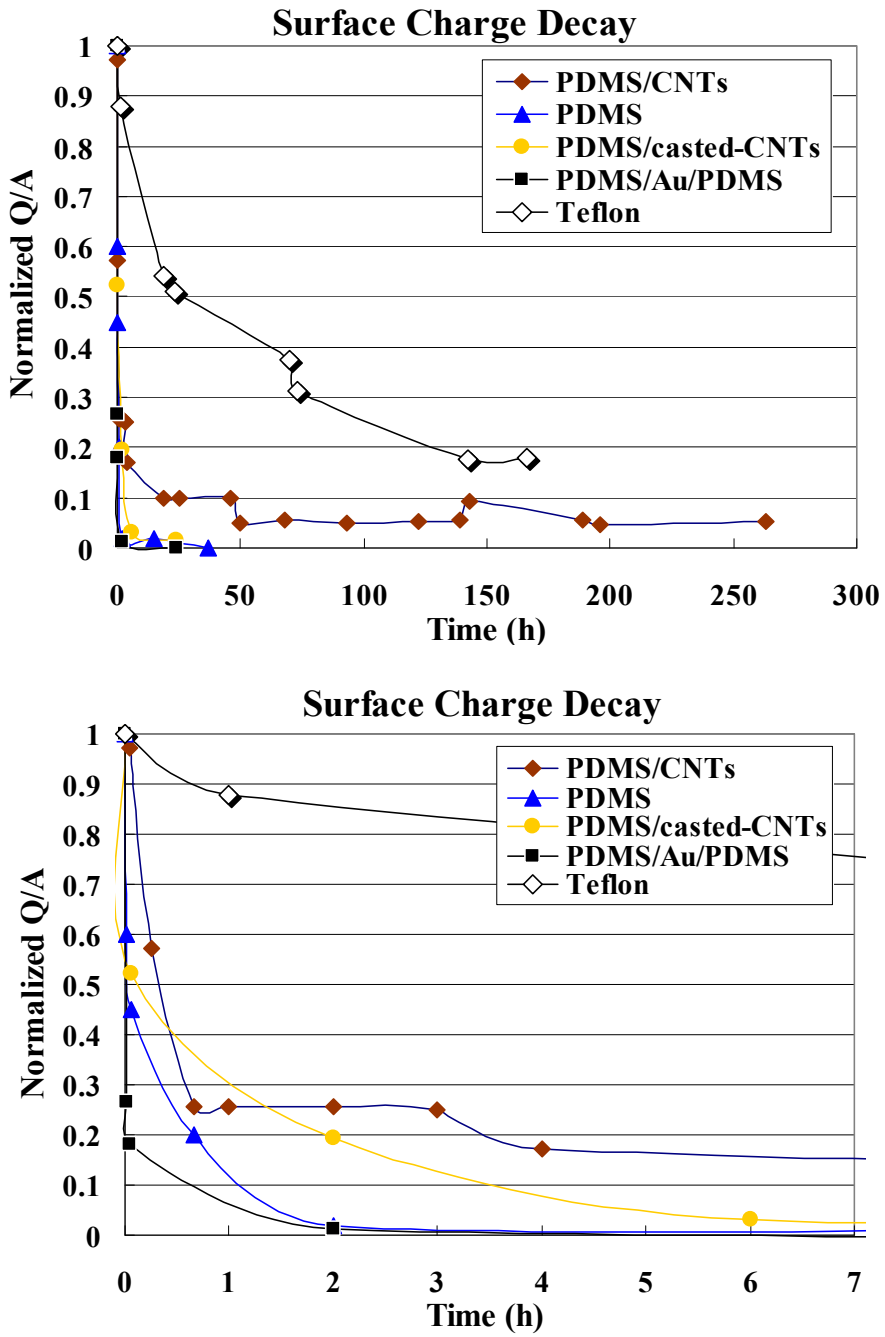

Figure 4.8: Top: Decay curves of the surface charge density (Q/A), Bottom: enlarged decay curve of the first 7 hours. The surface charge density in all cases has been normalized to its value at t=0.

Since there is a significant difference in charge storage behavior between PDMS/CNT composite materials and pure PDMS, it is reasonable to conclude that, as illustrated in Figure 4.3, charges can penetrate the topmost ultra-thin PDMS film and be trapped by the CNTs during the corona-charging. Since PDMS is an excellent electrical isolation material with a dielectric strength of 20 kV/mm, this thin dielectric layer may act as an energy barrier to prevent the charges injected to the CNTs from escaping to the outer environment. As a result, the PDMS/CNT composite shows higher long-term surface charge stability than either pure PDMS or pure CNTs. In this sense, the patterning of electrostatic charges can be achieved through the patterning of the CNTs. However, compared with some other non-elastic polymer electrets, such as Teflon which is charged under the same conditions, the elastic PDMS/CNT composite material still suffers faster charge decay (Figure 4.8). This may be partially attributed to the high volatile gas/vapor permeability and the relatively low volume resistivity of PDMS (~10^{14} Ω•cm), in contrast to the Teflon, which has a higher bulk resistivity of 10^{18} Ω•cm and much higher hydrophobicity that can prevent the trapped charges from recombining with water/gas molecules. The charge storage stability of the proposed micropatternable elastic material may potentially be improved by utilizing other elastomers with a lower electrical conductivity and lower vapor permeability as the matrix.

4.6 Evaluation of Power Generation of the Charged Elastic Composite

4.6.1 Ball Drop Experiment

To test the power generation of the charged composite, a ball drop experiment was performed (Figure 4.9a). In order to electrically connect the CNT/PDMS sensor structure, a 500 nm-thick gold electrode was first deposited on a glass slide using an

E-beam evaporator, followed by a deposition of a 1μm-thick silicon dioxide layer on top of it through a plasma-enhanced chemical vapor deposition (PEVCD) process. A metal wire was then fixed to one end of the gold electrode using silver epoxy. A corona charged PDMS/CNT composite with a dimension of 2 cm in length, 2 cm in width and 2mm in height was sandwiched between two glass substrates bearing the two-layer (Au/SiO_2) coatings. The assembled structure was electrically connected to an oscilloscope (Tektronix TDS 2014, 1MΩ input impedance and 95 pf capacitance) through the metal wires on both the top and bottom glass substrates. A steel ball with a mass (m) of 4.07g and a diameter of 10 mm was centered above the top glass slide and subjected a free fall from various heights (h). The output voltage of the sample was recorded from the oscilloscope.

From the curves in Figure 4.9b and Figure 4.10, a monotonic increase of voltage output across the charged composite was observed with the increased impact energy ($E=mgh$). A voltage response of 3V was generated from a 7mJ mechanical energy, which

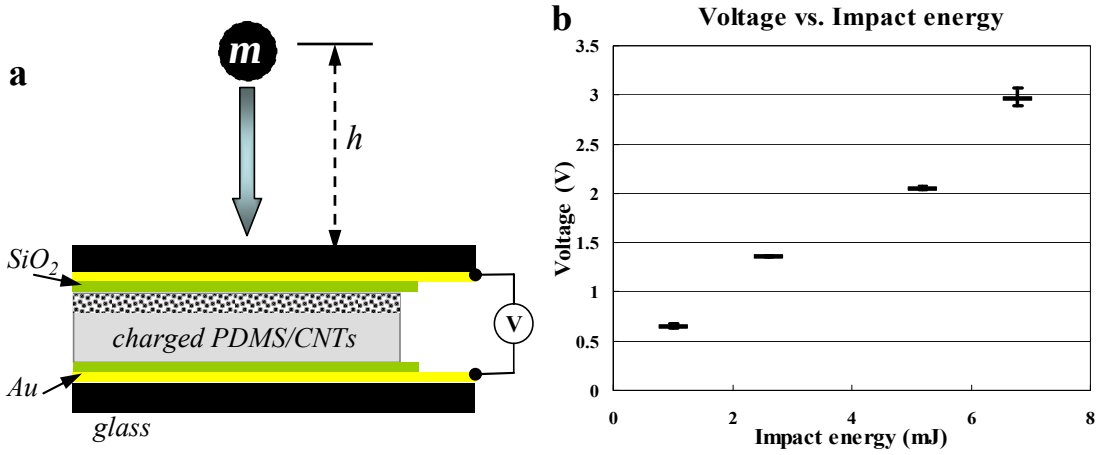

Figure 4.9: (a) Scheme of the ball drop experiment, and (b) voltage output as a function of impact energy ($E=mgh$).

may lead to potential applications in vibration-based energy harvesters, as well as impact sensors.

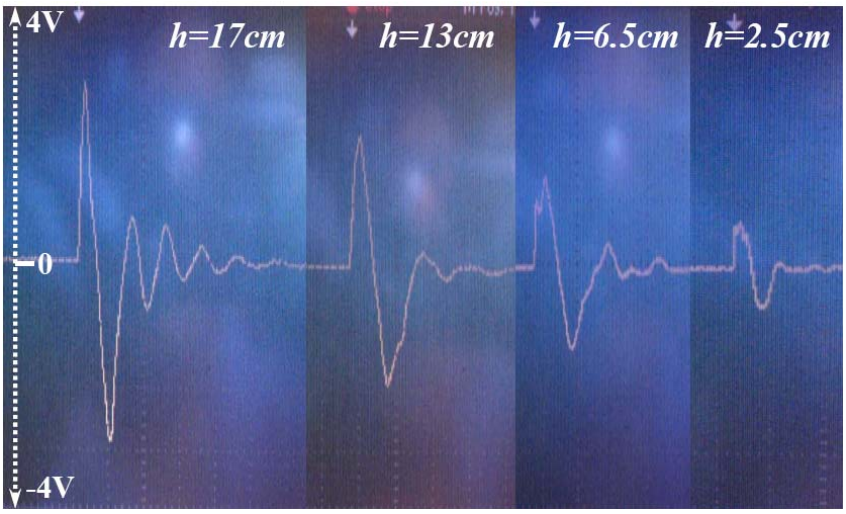

Figure 4.10: Curve of the voltage output of the sample as a function of time in response to different heights of the ball drop.

4.6.2 Mechanical Oscillation Induced Power Generation

The power generation behavior of the charged PDMS/CNT composite was further tested by vertically deforming the sample at varying frequency. Given the fact that PDMS is a viscoelastic material with a higher E_y than air, the materials developed herein should be more suitable for low frequency vibration energy harvesters that exploiting human or automotive motion. Therefore, the frequency range in which the material was characterized was chosen to be 1-50Hz.

The experimental setup is configured as shown in Figure 4.11. The sample has a circular-disk geometry with a diameter of 3.4 cm and a thickness of 1 cm. The top

PDMS/CNT composite layer is approximately 2μm thick, sitting on top of a bottom bulk PDMS film. Because of the large surface area of the tested sample, the aforementioned corona charging apparatus in Figure 4.5 was modified in an attempt to ensure a uniform charge distribution across the composite surface. A metal wire grid mesh (500μm spacing) was inserted 15mm above the sample holder and a voltage of -2500 V was applied to it during the corona charging process. Other settings were kept the same.

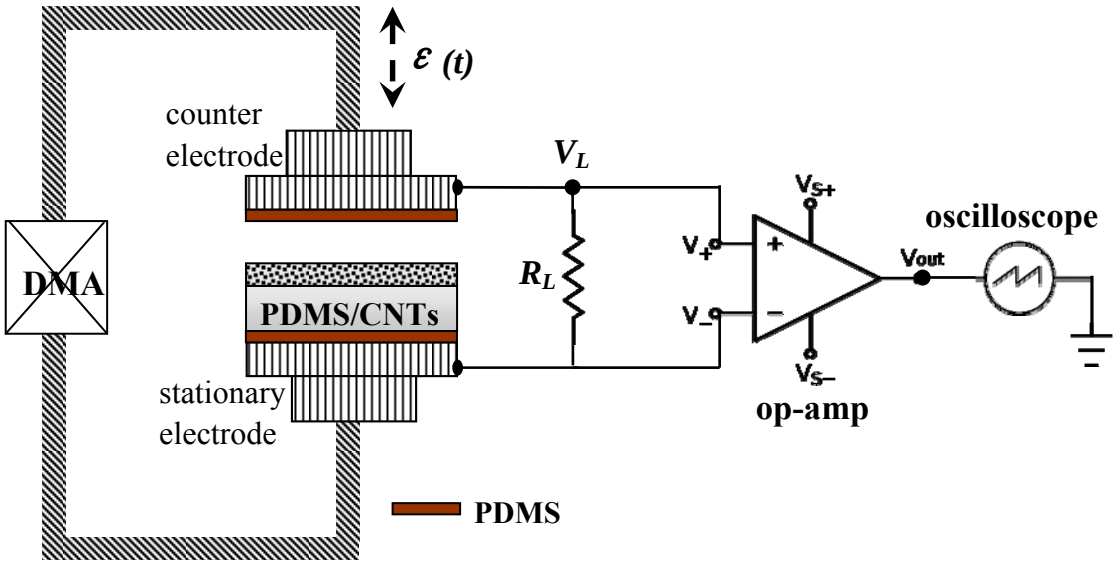

Figure 4.11: Scheme of the power generation experiment through cyclic displacement.

The two metal electrodes were coated with a very thin film of PDMS (~2μm) as an electrical insulation layer to prevent the charges on the electret from leaking to the external circuit. The electrodes have the same circular geometry and dimensions as the sample, and they were tightly fixed to a dynamic mechanical analyzer (DMA, ElectroForce® 3200, Bose Inc.). The bottom stationary electrode where the sample sat

was kept immobilized during the test, while the top counter electrode served as the moving electrode through which the cyclic vertical displacement was applied to the sample. A load resistor, R_L, was electrically connected to the top and bottom electrodes through two metal wires and was further connected to an op-amp (INA111, Texas Instruments) with an input impedance of $10^{12}\ \Omega$ and a gain of 6. The high input impedance of the amplifier allows the load matching by applying different external load resistances. The signal from the op-amp was further fed to an oscilloscope (Tektronix TDS 2014, P2220 probe with 1MΩ input impedance and 95pf input capacitance) where the voltage output across the sample induced by the cyclic change of the composite thickness was recorded (V_{out}). The voltage generated across the load (V_L) can be calculated by dividing V_{out} by the gain, which is 6 in this configuration. The generated instantaneous electrical power from the device is simply $P=V_L^2/R_L$.

In this study, a sinusoidal oscillation ($d(t)$) with amplitude of d_{p-p} was applied through the top counter electrode to the charged sample under different frequency (f), with $d(t) = d_{p-p}\left|\sin(2\pi f \cdot t)\right|$. During the testing, the charged sample was initially brought into intimate contact with both the top and the bottom electrode to ensure a synchronized response to the applied strain. The capacitance of the electret at the time=t, $C(t)$, can be calculated as:

$$C(t) = \varepsilon_0 \varepsilon_r \frac{A}{g - d(t)} \tag{4.15}$$

where ε_r is the relative permittivity of the electret (ε_r =2.65 for PDMS), ε_0 is the vacuum permittivity ($\varepsilon_0=8.7\times10^{-12}$ F/m), A and g are the surface area and unstrained thickness of the material.

The PDMS/CNT composite was charged in the abovementioned apparatus for 30min to a surface charge density of 1.7×10^{-7} C/m^2. A sinusoidal displacement with a d_{p-p} of 2mm was imparted to the sample, which corresponded to a maximum strain of 20%. The power generation was performed with a series of load resistance ranging from 150 Ω to 300 MΩ at frequencies ranging from 1-50Hz. The analysis of the data from all measurements showed that the voltage response in the time domain exhibited similar curve profiles as the one plotted in Figure 4.12a. A high voltage spike followed by a plateau in each cycle of the measurement was observed in samples with different load resistance driven at different frequency. A close observation of the deformation of the electret revealed that at the end of each displacement cycle when the top electrode was retracted to the initial position, it was lifted and disengaged with sample surface due to the resolution of the DMA transducer. A tiny air gap was consequently created between the top electrode and the electret. Therefore, the top electrode first struck the top surface in the subsequently cycle and the high power spike was found to be recorded when this impact occurred. The plateau in the voltage curve was found to correspond to the deformation of the sample when top electrode was in intimate contact with the composite.

The plateau in the *V-t* curve is ascribed to the mismatch between the cut-off frequency of the devices and the driven frequency. Here, the maximum applied load resistance was 300 MΩ. Hence the RC time constant of the device is $\tau=R_LC_0 < (300\times10^6) \times (\varepsilon_r\times\varepsilon_0\times A/g_0) = 6\times10^{-4}$ s. The cut-off frequency can then be calculated as $f_c= 1/(2\pi \tau)>270$Hz. Since the driven frequency applied by the DMA was two orders of magnitude lower than f_c, no signal was recorded. This explanation was further confirmed by a study where the initial position of the top electrode was carefully adjusted to ensure intimate

contact with the sample throughout the whole testing duration. As expected, no voltage output was observed in this experiment either as shown in Figure 4.12b.

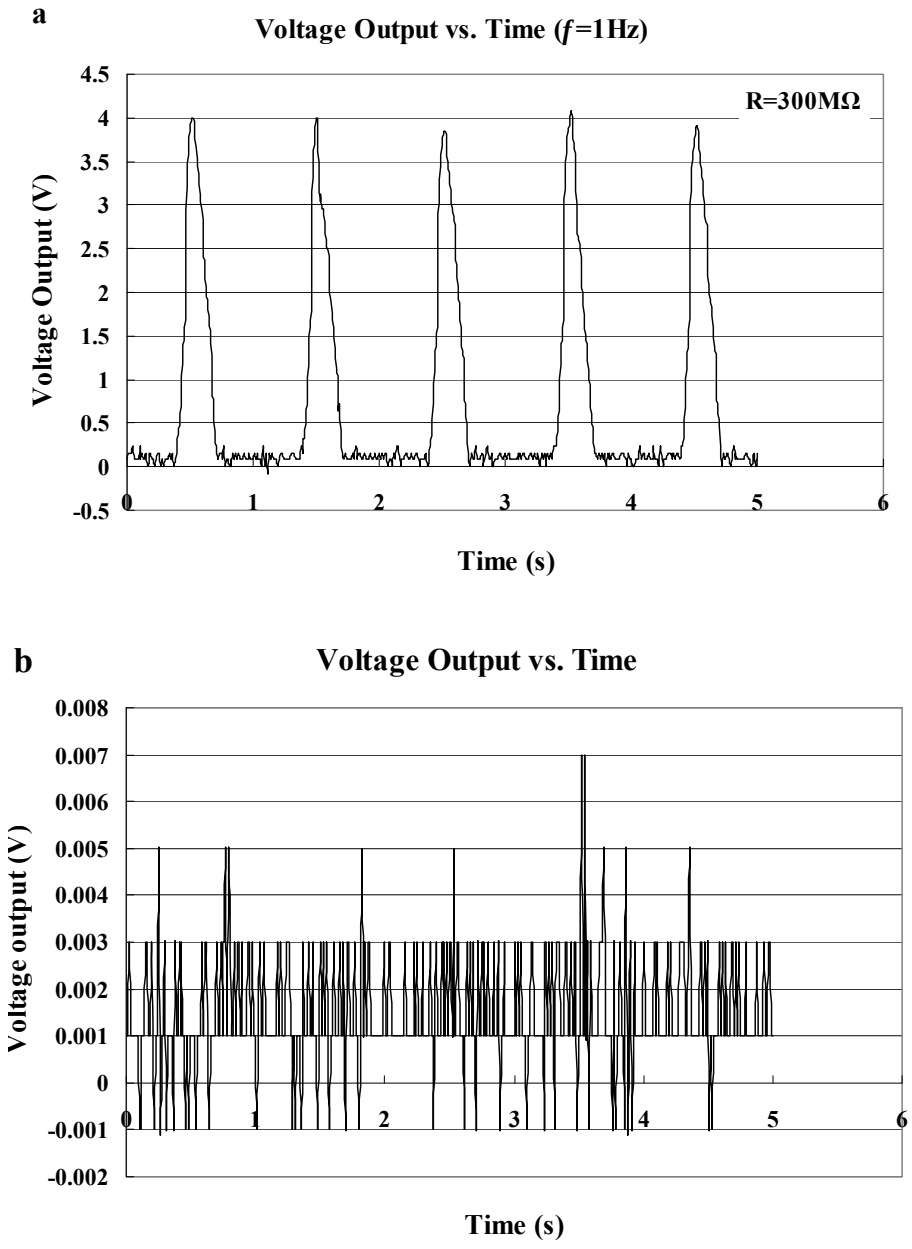

Figure 4.12: Time trace of voltage output under (a) an air gap mode, and (b) intimate contact mode.

The high power spike acquired in the curve likely arose from the high frequency component associated with the initial impact between the counter electrode and the sample surface, which may cause rapid compression/deformation of the composite. Kranz[30] showed that the frequency generated from a Hertzian contact could be in the range of 10^4Hz, which is orders of magnitude higher than the f_c and the signal can therefore be recorded by the circuit. A similar phenomenon was observed in a shoe-mounted piezoelectric power generator[31,32], as shown in 4.13,where the larger power spikes generated from the PZT Unimorph was considered to resulte from the rapid initial bending or compression of the device when the human foot hit the device.

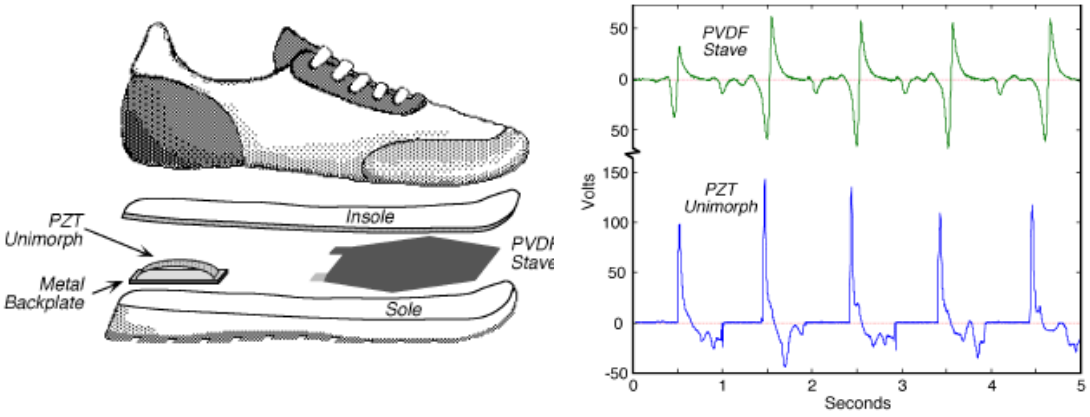

Figure 4.13: Power generation behavior of a shoe-mounted piezoelectric energy harvester[32].

In an attempt to match the cut-off frequency of the material with the driven frequency in the practical application, the thickness of composite was reduced from 10mm to 1.8mm and the input impedance was increased to 500MΩ. Hence the RC time constant of the new sample became $\tau=RC= 5\times10^8\ \Omega\times\ 1.2\times10^{-11}$ F=0.006s. The resultant

cut-off frequency (f_c) is $f_c = \frac{1}{2\pi\tau} = 27\text{Hz}$, which falls in the range of the aimed applications (1~50Hz). In order to separate the voltage spike induced by the impact from the voltage generated by the actual periodic deformation of the elastic composite, the initial position of the top electrode in the device was carefully adjusted to eliminate the possibility of air-gap formation during the test. Similarly, a sinusoidal cyclic displacement, $d(t) = d_{p-p}\left|\sin(2\pi f \cdot t)\right|$, was imparted to the sample bearing a surface charge density of 1.7×10^{-7} C/m^2. When a sinusoidal displacement with a d_{p-p} of 3×10^{-4} m was applied to elastic electret at the f=1Hz, the voltage output exhibited a sinusoidal response with a maximum voltage output (V_{p-p}) of 0.17V upon a 270μm actual displacement amplitude (Figure 4.14b). In order to rule out the possibility that the recorded voltage response may arise from the transducer of the DMA, a similar test was performed without the charged sample. No voltage response was recorded in this case as indicated in Figure 4.14c, which verified that the power was generated from the deformation of the charged elastic PDMS/CNT composite. The average power generated is 1.2×10^{-11} W, which was calculated through the following equation:

$$\overline{P} = \frac{E}{t} = \frac{\int_0^t \frac{V^2}{R_L}}{t} = \frac{\sum (V_i)^2 \cdot \Delta t}{t \cdot R_L} \tag{4.16}$$

Where $\overline{P}$ is the average power, E is the total energy generated, and Δt is the sampling interval, t is the measurement duration. Though the generated power in this preliminary study is small because of the high input impedance, it can potentially be improved when the device is scaled up into larger area. The surface area of the PDMS/CNTs composite

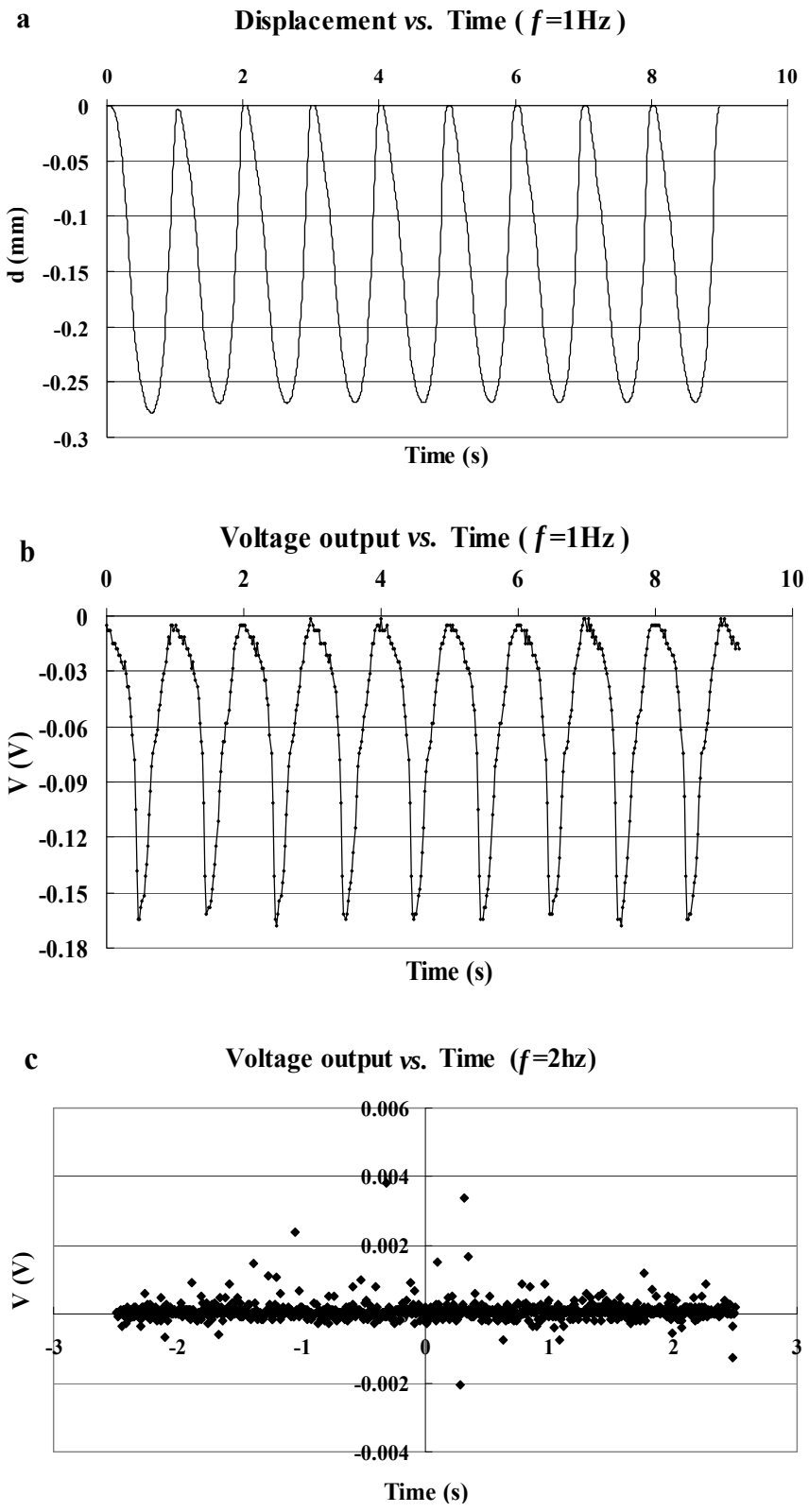

Figure 4.14: Time trace of (a) displacement, (b) voltage output at f =1Hz, and (c) voltage output at f=2Hz when no sample was present.

(A) can be easily increased by orders of magnitude, and thereby the capacitance of the material will be increased proportionally with the increased A. the input impedance can then be reduced in orders of magnitude to achieve the same f_c. Consequently, a higher power output may be accomplished. This PDMS/CNT composite is suitable for low-cost and large area applications such as energy harvester in playground or car tires, and microphone if embedded onto walls.

Furthermore, the maximum voltage output ($V_{p\text{-}p}$) as a function of the displacement amplitude ($d_{p\text{-}p}$) imparted to the devices was investigated, aiming to correlate the power generation of the sample with the applied strain. From equation 4.12 and 4.13, the following relation can be derived:

$$V_{p-p} = \frac{Q}{C_2} - \frac{Q}{C_1} = \frac{Q(d_2 - d_1)}{\varepsilon_0 \varepsilon_r A} = \frac{\sigma_s}{\varepsilon_0 \varepsilon_r} d_{p-p} \tag{4.17}$$

The maximum voltage output is expected to increase linearly when the maximum displacement increases. In this study, the voltage response of the sample was recorded under different d_{p-p} at the same frequency. Both the theoretical and experimental values of V_{p-p} were collected and plotted as a function of d_{p-p} at f=1Hz in Figure 4.15. Though some minor deviations are observed, the experimental values agree well with the theoretical predications, which indicates that the power generation behavior of the developed material could be well controlled and predicted.

The V_{p-p} and the generated power as a function of oscillation frequency were further characterized and plotted in Figure 4.16. Due to the limit of the DMA transducer used in this study, when the applied frequency was over a certain value, the actual

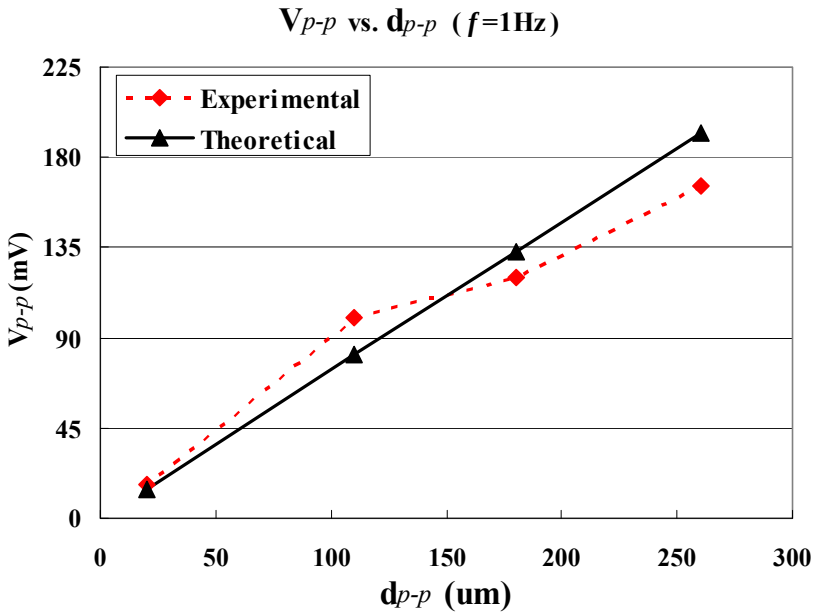

Figure 4.15: Theoretical and experimental plot of V_{p-p} as a function of d_{p-p}.

amplitude of the displacement imparted to the device failed to reach the setting values, and it decreased with increased frequency. As found in Figure 4.15, different d_{p-p} could lead to the variation of the voltage output. In order to decouple the frequency effect from the displacement effect on the voltage/power output, the setting value of the displacement amplitude was adjusted each time the frequency was varied to achieve a relatively similar d_{p-p} among all the measurements. The d_{p-p} was selected to be approximately 20μm, which was readily achievable for the majority of the frequencies applied in this study (1-50Hz). The test results in Figure 4.16a indicates that increased frequency also induced an increased V_{p-p} when the f was less than 35Hz. However V_{p-p} was found to start to fall when the frequency was higher than 35Hz, which was likely due to the significant decrease in the actual d_{p-p} the top electrode could reach under this frequency range as shown in Figure 4.16a. The power output showed a similar trend with the frequency, with

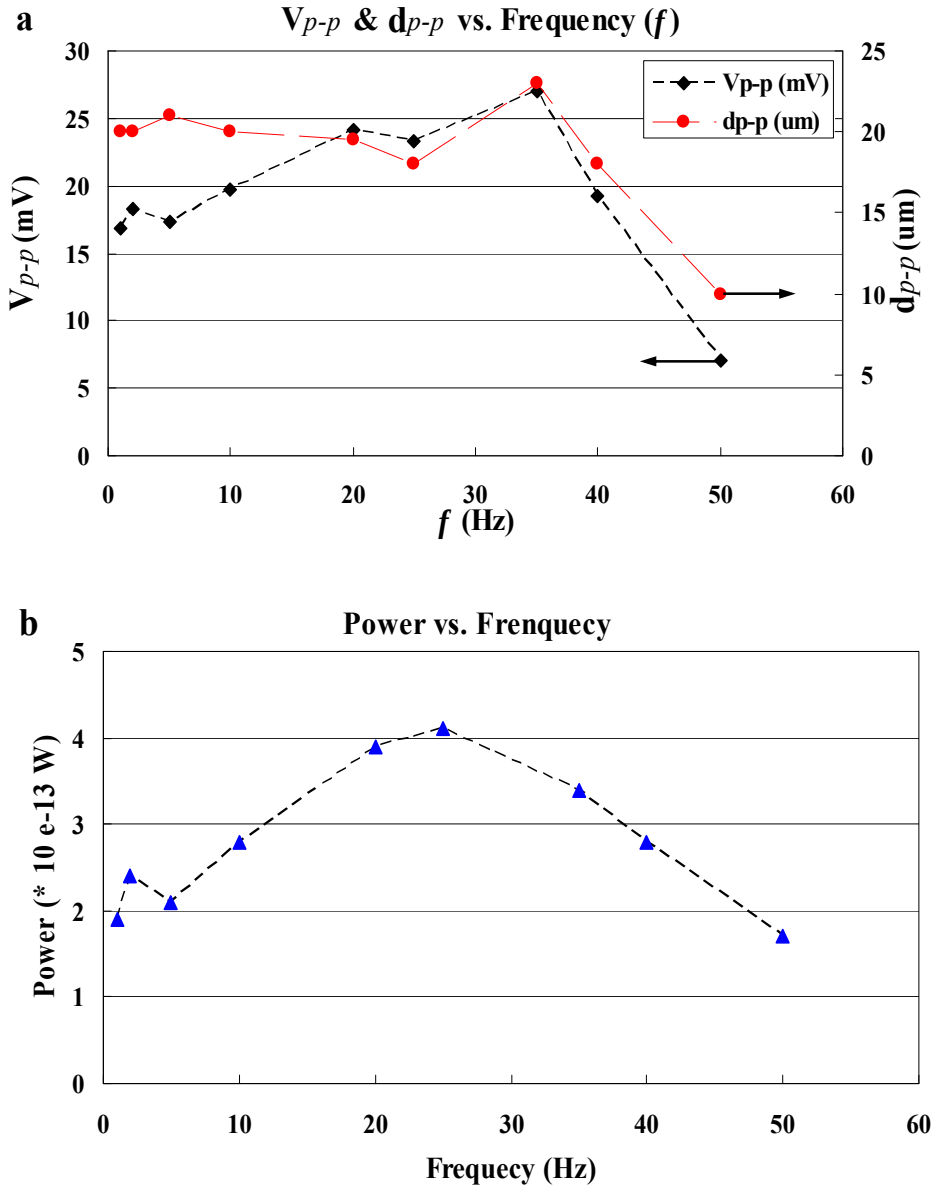

Figure 4.16: Frequency dependence of (a) maximum voltage output ($V_{p\text{-}p}$) and displacement amplitude ($d_{p\text{-}p}$), and (b) average power output.

a maximum power output occurring at f=25Hz which was very close to the cut-off frequency of the material (f_c=27Hz). The significant decrease of the power output observed when the frequency was higher than 30Hz may also be attributed to the much lower displacement amplitude the device could achieve at this high frequency range.

Similar observations have also been reported by other peers[8,33]. It is worth noting that the power reported here is not the maximum power the device can achieve, because the displacement applied is much smaller than the maximum value that the composite can be compressed, and so is the electret area.

In the charge storage stability study, it has been shown that PDMS itself can not store charges for a sufficiently long time and therefore can not serve as an electret (Figure 4.8). Here, we further compared the power generation capability of the non-charged PDMS with the PDMS/CNT composite. The results in Figure 4.17 showed that non-charged PDMS exhibited a similar voltage response with the composite under the same testing conditions (i.e. actual displacement amplitude). After the experiment, the surface charge density of the PDMS was measured to be 0.25×10^{-7} C/m^2. This charging of the PDMS was likely due to the electrification/triboelectricity when PDMS was periodically compressed and rubbed with the top and bottom metal electrodes during the

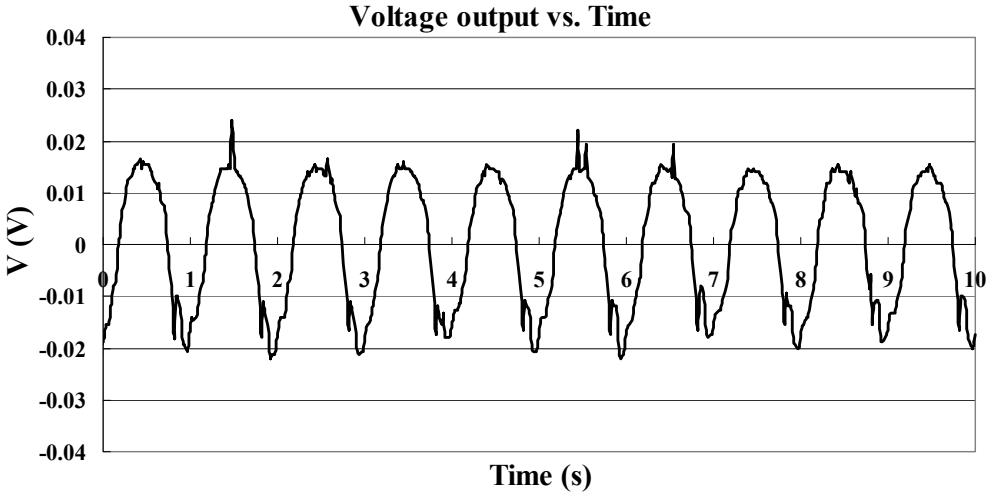

Figure 4.17: Time trace of voltage output of a non-charged PDMS at f=2Hz.

test. Triboelectricity is the generation of electricity from rubbing two dissimilar things together. The mechanical motion causes electrons to be transferred from one material to another, resulting in an excess of electrons on one material and a deficiency of electrons on the other. However, the voltage output generated of the non-charged PDMS is 33 mV, which is much lower than what was achieved from the PDMS/CNT composite (170 mV) under the same external load.

Besides the study of the contact mode power generation, the performance of the charged PDMS/CNT composite was characterized in a non-contact mode as well. In this test, the top electrode was initially placed 1mm above the top surface of the charged composite. A vertical sinusoidal oscillation with the amplitude of 2mm was applied to the counter electrode through DMA, and the lowest position of the counter electrode was kept at 1mm above the composite throughout the oscillation. This configuration is the same with the type (Out-of-plane Electret Power Generator with Variable Gap Distance) discussed in 4.2.3. As expected, the voltage output of the device showed similar sinusoidal response to the sinusoidal variation of the capacitance at different frequency (top graph in Figure 4.18). The maximum power output was found to occur at R_L=10MΩ.

4.7 Equivalent Piezoelectric Coefficient of the Elastic Composite

The piezoelectric coefficient, d_{33}, is an intrinsic material property utilized to evaluate the power generation capability of a piezoelectric material. Though an electret is not a piezoelectric material by definition, it shares certain similarities in terms of its power generation behavior/pattern. That is, in both cases the power is generated through the displacement current induced by an external mechanical force. Though the equation

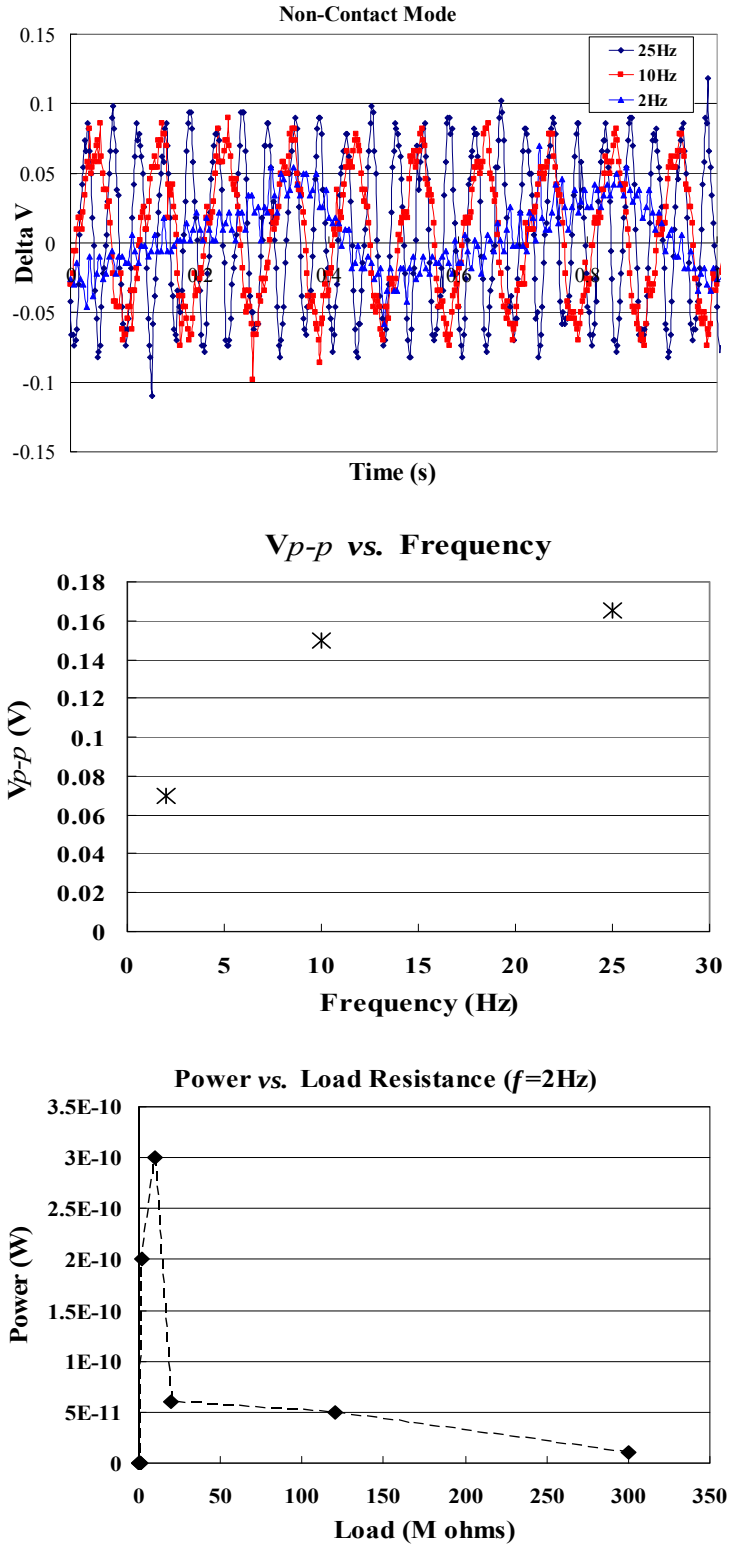

Figure 4.18: top: Time trace of the voltage output at different frequency, middle: peak voltage at different frequency, and bottom: power output as a function of load resistance.

4.1 could not be utilized to calculate the equivalent piezoelectric coefficient of the electret-like material, $d`_{33}$, due to the lack of the knowledge of the η in this study, we calculated this value in the compressive force mode according to the following equation[34]:

$$d`_{33} = \frac{Q}{F} = \frac{I\Delta t}{\varepsilon A E_y} = \frac{V\Delta t}{R_L \varepsilon A E_y} \tag{4.18}$$

where the Q is the induced charge under the mechanical force F, I is the displacement current flow through the load resistor R_L, Δt is sampling interval of the test, ε is the strain applied to the material. E_y is the Young's modulus of the electret, and A is the surface area of the electret. In this test, we have E_y=2MPa, R_L=500MΩ and A=9.1×10^{-4} m^2. From the V-t curve in Figure 4.14, $V_{p\text{-}p}$=0.17V, ε_{max}= 0.26/1.8=0.14,and Δt=0.01s were obtained. Therefore, the $d`_{33}$ can be approximated to be 1.4×10^{-14} C/N.

4.8 Summary and Future Work

In this chapter, a PDMS/CNT composite suitable for micropatternable elastic electrets has been developed and fabricated. Its charged electrical behavior has been discussed. The material exhibited electret characteristics with the charge storage stability in excess of 280 hours. The power generation capacity of the charged composite has been characterized and successfully demonstrated in both a ball drop experiment and cyclic mechanical load experiments. The results indicate that the composite combining two non-electret materials can store charges, which may be conveniently utilized and conformably implemented into shoes, car tires or playground for large area and low cost energy harvesting system. Further work can be focused on improving the charge storage

stability and optimizing the material structure to improve the power generation performance.

4.9 References

(1) Baeg, K. J.; Noh, Y. Y.; Ghim, J.; Lim, B.; Kim, D. Y. *Advanced Functional Materials* **2008**, *18*, 3678.

(2) Altafim, R. A. P.; Qiu, X. L.; Wirges, W.; Gerhard, R.; Altafim, R. A. C.; Basso, H. C.; Jenninger, W.; Wagner, J. *Journal of Applied Physics* **2009**, *106*.

(3) Naruse, Y.; Matsubara, N.; Mabuchi, K.; Izumi, M.; Suzuki, S. *Journal of Micromechanics and Microengineering* **2009**, *19*.

(4) Tianzhun, W.; Suzuki, Y.; Kasagi, N. Micro Electro Mechanical Systems, 2008. MEMS 2008. IEEE 21st International Conference on, 2008; p 591.

(5) Sessler, G. M. *Electrets*; Electrostatic Applications, 1980.

(6) Lushcheikin, G. A. *Physics of the Solid State* **2006**, *48*, 1023.

(7) Xu, W.J.; Allen, M. G. Solid-State Sensors, Actuators and Microsystems Conference, 2009. TRANSDUCERS 2009. International, 2009; p 2242.

(8) Lo, H. W.; Tai, Y. C. *Journal of Micromechanics and Microengineering* **2008**, *18*.

(9) Amjadi, H. *Dielectrics and Electrical Insulation, IEEE Transactions on* **1999**, *6*, 852.

(10) Amjadi, H. *Ieee Transactions on Dielectrics and Electrical Insulation* **1999**, *6*, 852.

(11) Resnick P R, B. W. H. p. *Fluoropolymers 2,*; (Springer US) 2002

(12) Sakane, Y.; Suzuki, Y.; Kasagi, N. *Journal of Micromechanics and Microengineering* **2008**, *18*.

(13) Ogawa, G.; Kanda M.; Okano, K. *in: Reports Res. Lab. Asahi Glass Co., Ltd.* **2005**, *55* 47.

(14) Zhao, D.; Duan, L. T.; Xue, M. Q.; Ni, W.; Cao, T. B. *Angewandte Chemie-International Edition* **2009**, *48*, 6699.

(15) Altafim, R. A. C.; Basso, H. C.; Altafim, R. A. P.; Lima, L.; de Aquino, C. V.; Neto, L. G.; Gerhard-Multhaupt, R. *Dielectrics and Electrical Insulation, IEEE Transactions on* **2006**, *13*, 979.

(16) Tsurumi, Y.; Suzuki, Y.; Kasagi, N. Micro Electro Mechanical Systems, 2008. MEMS 2008. IEEE 21st International Conference on, 2008; p 511.

(17) Tsutsumino, T.; Suzuki, Y.; Kasagi, N.; Sakane, Y. Micro Electro Mechanical Systems, 2006. MEMS 2006 Istanbul. 19th IEEE International Conference on, 2006; p 98.

(18) Jukka Lekkala, M. P. a. K. K. *http://www.azom.com/Details.asp?ArticleID=398* **2001**.

(19) Tsutsumino, T.; Suzuki, Y.; Kasagi, N. Solid-State Sensors, Actuators and Microsystems Conference, 2007. TRANSDUCERS 2007. International, 2007; p 863.

(20) Suzuki, Y. In *PowerMEMS 2010* Leuven, Belgium, 2010.

(21) Boland, J. Ph.D Dissertation, CALIFORNIA INSTITUTE OF TECHNOLOGY, 2005.

(22) Ishii, M.; Hamilton, B.; Poolton, N. *Journal of Applied Physics* **2008**, *104*.

(23) Jespersen, T. S.; Nygård, J. *Nano Letters* **2005**, *5*, 1838.

(24) Li, H.; Zhang, Q.; Marzari, N. *Nanotechnology* **2008**, *19*.

(25) Robert-Peillard, A.; Rotkin, S. V. *Ieee Transactions on Nanotechnology* **2005**, *4*, 284.

(26) Xia, Z. F. *Ieee Transactions on Electrical Insulation* **1991**, *26*, 1104.

(27) Malstrokecki, J. A. *Physical Review B* **1999**, *59*, 9954.

(28) Nguyen, D. H.; Sylvestre, A.; Bechu, S.; Rowe, S. Electrical Insulation and Dielectric Phenomena, 2004. CEIDP '04. 2004 Annual Report Conference on, 2004; p 631.

(29) Prime, D.; Paul, S.; Josephs-Franks, P. W. *Philosophical Transactions of the Royal Society a-Mathematical Physical and Engineering Sciences* **2009**, *367*, 4215.

(30) Kranz, M. S. Ph.D Thesis, Georgia Institute of Technology, 2011.

(31) Shenck, N. S.; Paradiso, J. A. *Ieee Micro* **2001**, *21*, 30.

(32) Kymissis, J.; Kendall, C.; Paradiso, J.; Gershenfeld, N. In *Proceedings of the 2nd IEEE International Symposium on Wearable Computers*; IEEE Computer Society, 1998.

(33) Suzuki, Y. In *PowerMEMS* Belgium, 2010.

(34) Neugschwandtner, G. S.; Schwodiauer, R.; Bauer-Gogonea, S.; Bauer, S.; Paajanen, M.; Lekkala, J. *Journal of Applied Physics* **2001**, *89*, 4503.

CHAPTER 5

HAIRLIKE CARBON-FIBER-BASED SOLAR CELL

5.1 Background & Motivation

Carbon materials carry a variety of properties which exhibit great potential as functional components in MEMS devices. For example, their ability to form densely packed 3D conductive structures with large surface area associated with the 3D spatial geometry is extremely favorable in devices such as mini-batteries and solar cells where the performance relies substantially on large total effective surface area in a small footprint[1,2]. On the other hand, the high elastic moduli of diamond and diamond-like carbon (DLC) films have been exploited in the design of high frequency resonators and comb-drives for communication and sensing applications. Chemically modified surfaces and structures of diamond and DLC films have also been designed to serve as sensor materials for sensing traces of gases, as well as for detecting bio-molecules in biological research and disease diagnosis[3,4,5]. Moreover, as demonstrated in Chapter 3 and Chapter 4, carbon nanotubes have been effectively implemented and utilized as key functional components in MEMS sensing and energy harvesting devices, and successfully demonstrated preferential characteristics in these types of devices such as high sensitivity and flexibility.

In addition to utilizing the carbon material as the key functional constituent in MEMS devices, we would like to further expand the work to exploit carbon materials as substrates/building blocks to realize new types of MEMS devices. The variety of the spatial format of the carbon materials can potentially lead to new MEMS systems with innovative geometries that are not readily available from traditional substrates such as silicon, metal and glass. Specifically in this PhD study, carbon fiber (CF) was selected and its feasibility as a MEMS substrate was evaluated. Similar to CNTs, CF possesses excellent thermal stability, superior mechanical strength, lightweight with a specific strength (strength/density) of three times of that of steel, reasonable electrical conductivity and high aspect ratio geometry that can be produced from a roll-to-roll process. All these merits are advantageous when CF serves as the substrate in MEMS applications such as energy harvesting devices[6] and MEMS scanning micromirror arrays[7] . In this chapter the CF was further exploited as the building block for a fiber type solar cell. This hairlike fiber PV was designed and developed by combining the high aspect ratio fiber spatial format, excellent electrical conductivity and superior thermal stability of the carbon fiber.

Before the unsustainable fossil fuel that the contemporary technology and society rely on heavily is exhausted, alternative energy sources need to be well developed. Solar energy, alongside nuclear and bio-fuel energy, is considered to be one of the primary solutions to tackle the incoming energy crisis due to its availability and eco-friendly nature. Solar cells absorb and convert solar radiation into electrical power, and have undergone intensive studies in the past decade. In principle, a material with a bandgap energy within the range of visible light (1.8eV~3.1eV) can be utilized in photovoltaics

(PV). This refers to a large variety of photosensitive materials, including doped silicon, III-V compounds, organic dyes and polymers, and quantum dots. Among them, silicon possesses the favorable advantages of high energy conversion efficiency at relatively low cost, and it remains the only material that is well-researched in both bulk and thin-film forms. Up to now, large silicon solar panels have been widely commercialized with high volume production.

Miniaturized photovoltaics, in comparison to large solar panels, may serve as integrated renewable power sources for nano/microelectronics such as those in wireless sensor networks (WSN) and robots[8]. In particular, photovoltaic structures with unusual geometries that complement the devices they are powering, or that can be assembled into larger sources with unusual geometries, can be enabled by MEMS-based fabrication techniques. Reported nanowire or micro-sized PV devices yielded output power in the range of pW to μW with photocurrent up to μA and output voltage of 0.1~0.4V[8-9,10]. Their output power can also be scaled up by growing nanowire arrays or connecting each individual cell in series and/or in parallel[8,10,11]. In particular, MEMS devices such as electrostatic or piezoelectric motors usually require driving voltage/current in the range of 3V~400V/nA~μA, which can be readily provided by appropriately interconnected, micro-sized solar cells as the self-contained on-board power supply[10].

In addition to flat panel micro/nano solar cells, flexible fiber-type solar cells (FFSCs) with hairlike structure have received growing attention due to their potential in the fields of smart textiles, wearable electronics and stealth devices to provide energy. Silica fibers, metal wires and plastic optical fibers have been utilized as the building substrates to construct organic solar cells, which may enable large area weavable PVs

with lightweight and low cost[12,13,14]. Another benefit of such cylindrical device architecture is that solar cells with radial p-n junctions can induce efficient carrier separation/collection when the direction of light absorption and carrier collection are orthogonalized[15]. Inspired by the advantages brought by the cylindrical geometry, researchers have developed various wire-type solar cells based on different photosensitive materials and device configurations. Lee *et al.* configured a wire PV where a photosensitive poly(3,4-ethylenedioxylenethiophene) layer was coated over a stainless steel wire serving as the primary electrode[16]. This hybrid wire was electrically adhered to a counter stainless steel wire electrode to collect the photocurrent (Figure 5.1a). An efficiency of 3% was achieved in this device. Shtein *et al.* constructed a CuPc:C60 layer on a polyimide coated silica wire with a diameter of 480um. In this configuration, the anode and the cathode were deposited concentrically around the same fiber substrate as shown in Figure 5.1c. Power conversion efficiency of 0.5% was reported[14]. To resolve the issues associated with the high incident reflection and low conductivity of the outer counter electrode in this configuration, structures such as twisted electrode wire have been introduced into the fiber PV (Figure 5.1b). For instance, a stainless wire coated with P3HT/PCBM as the photosensitive material was twisted with another wire as the counter electrode[17], which leaded to an efficiency of 3.27% . Zou and co-workers also reported a similar structure with a stainless stainless wire coated with TiO_2 film, and twisted with another gold wire to complete the cell[18,19]. The efficiency of the fiber PV is up to 2%. Optical fibers have also been utilized as the building block for wire-shape ZnO-based solar cells, where the light was injected and propogated inside the optical fiber. The energy conversion efficiency is significantly increased due to

continuous refractions and reflections of the light inside the fiber[12, 20]. Fiber-shaped PV can be further extended into mesh-like structures as shown in Figure 5.1d, which possess

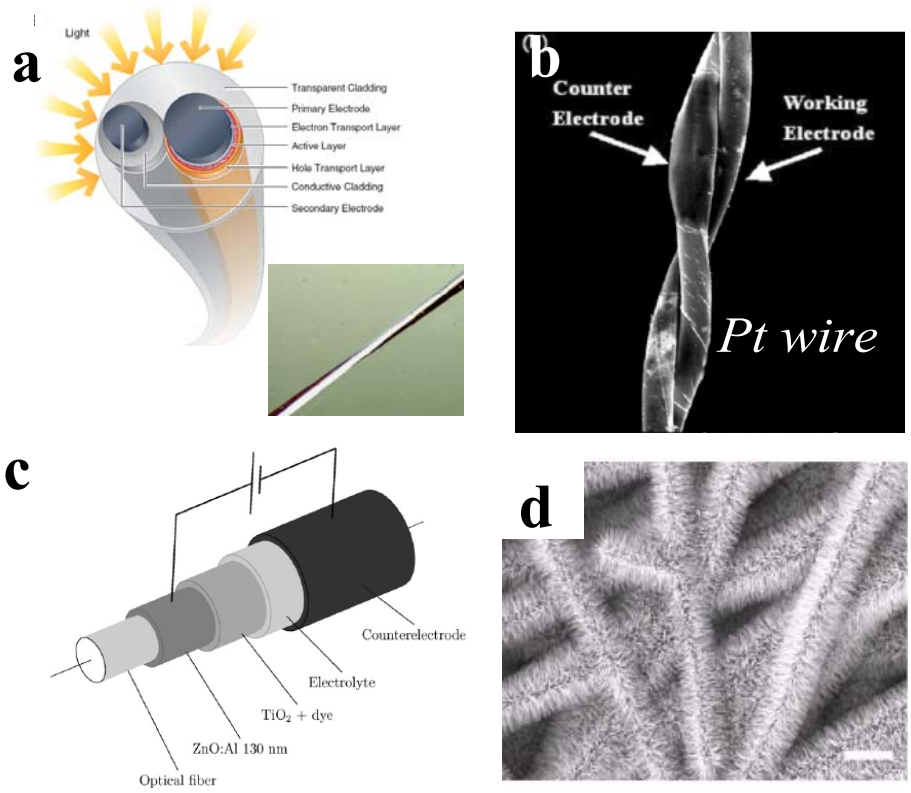

Figure 5.1: Reported fiber type solar cell (a) parallel electrode wires configuration[16], (b) twisted electrode wires configuration[17], (c) concentric coating configuration[12], and (d) zinc oxide coated CF solar cell[6].

the advantages of reduced light loss and the potential to combine fiber cells with different absorption bands[19,20]. In the case of solar cells with reduced photoactive area, gallium arsenide (GaAs), single-crystal silicon or poly-silicon is preferred as the photoactive layer because of their high energy conversion efficiency. This usually requires cell substrates

with good thermal stability to endure the high processing temperature, which is challenging for the aforementioned metal wire or plastic fiber substrates.

5.2 Carbon Fiber based Solar Cell

Carbon fiber, as discussed in Chapter1, is a flexible and light-weight textile material with a diameter of 5-20 um. Researchers are beginning to utilize this material in metal reinforcement and MEMS applications such as video displays[21,22], exploiting the excellent strength and fatigue properties of the CF. Furthermore, CF is a conductor with a resistivity of 1.8×10^{-5} Ω·m and can withstand temperature up to 1500ºC, which is compatible with the high processing temperature of silicon diodes. This micro-fiber can therefore be utilized as a building block to construct silicon-based fiber solar cells. A recent study reported a solar cell composed of ZnO nanowires grown on a random carbon nanofiber network fabricated by electrospray deposition. This mesh-like PV demonstrated an open circuit (V_{oc}) of 350 mV, a short circuit current density (J_{sc}) of 11.2 mA/cm^2 and a fill factor (FF) of 0.28[6]. The work discussed in this chapter focuses on exploring the possibility of fabricating coaxial core-shell solar cells by incorporating a radial poly-Si *p-n* diode onto a carbon fiber. The hairlike solar cell can benefit from the properties of the CF such as cylindrical geometry, excellent electrical and mechanical properties, extremely low cost and excellent thermal stability, which allows the deposition of high quality co-axial poly-Si onto this lightweight substrate. In addition, the conductive CF also serves simultaneously as an electrode to collect photogenerated carriers. The carbon fiber based hairlike PV architecture which has macro-scale cell lengths while maintaining micron-level integration capability was designed, fabricated and characterized. The photovoltaic effect of the device has been demonstrated. The

developed PV not only demonstrates the feasibility of utilizing CF as a MEMS fabrication substrate, but also results in solar cells of spatial format suitable for high-degrees of co-integration into MEMS devices. This type of hairlike PV may be further implemented or embedded into flexible substrates such as PDMS or parylene film to enable applications in foldable and conformable microelectronic systems.

5.2.1 Device Concept

The cross section of the proposed fiber PV is illustrated in Figure 5.2, where the CF serves as the core electrode as well as the mechanical backbone, and a poly-Si p-n diode is utilized as the photoactive shell material. Under illumination, the photosensitive diode will absorb photons whose energies are equal to or greater than the bandgap of the PV material. The photogenerated electrons (e^-) and holes (h^+) will then be swept into the outer n-type and inner p-type poly-Si layer respectively, by the established built-in electric field at the junction. The holes diffused into the p-type layer will be further collected by the CF core electrode. The electrons will be transported within the top n-type layer and collected by the top electrode. Rhe radial *p-n* architecture may endow the cell

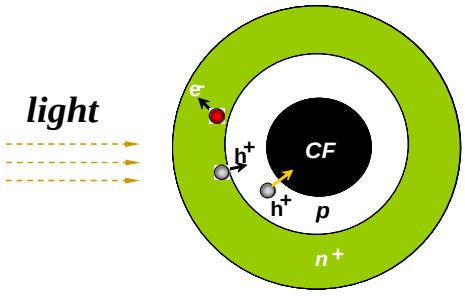

Figure 5.2: Scheme of cross section of the fiber solar cell and separation of the photogenerated electron (e^-) and hole (h^+) under illumination.

with a better charge collection efficiency since the carrier collection distance may be smaller or comparable to the minority carrier diffusion length in this configuration. This will reduce the opportunity of charge recombination and enable short range and efficient radial carrier separation[23].

5.2.2 Material Development and Fabrication Process

The fabrication process of creating fiber PV with a radially-modulated p-n poly-Si diode is depicted in Figure 5.3. The as-received carbon fibers (*34-700, Grafil Inc.)* were first thoroughly cleaned with acetone and isopropyl alcohol (IPA) to remove possible organic impurities. A layer of intrinsic (*i*) poly-Si was then deposited onto the carbon fibers through Low Pressure Chemical Vapor Deposition (LPCVD) at 588 °C. Boron-doping of the polysilicon was further performed by thermal diffusion with a solid dopant source (*Techneglas Technical Products Planar Dopants, GS-183*) at 1050°C, which turned the intrinsic poly-Si layer into *p* type. Phosphorus diffusion into the p-type poly-Si layer was performed subsequently by similar thermal diffusion at 950°C with a solid phosphorus dopant source to generate a shallow *p-n* junction in the radial direction of the fiber. In this study, SUPREM simulation was utilized to parameterize the doping process with an attempt to control and optimize the sheet resistance of the top n type emitter and the junction depth of the diode. To make the electrical connection from the carbon fiber to the external circuit, a wet chemical etching (HNO_3: Water: HF=50:20:1) of the poly-Si was performed to remove part of the poly-Si. However, this process was found to create a very rough surface over the rest of the device and cause breakage of fibers(Figure 5.4), which were likely due to the gas bubbles and heat evolved during the

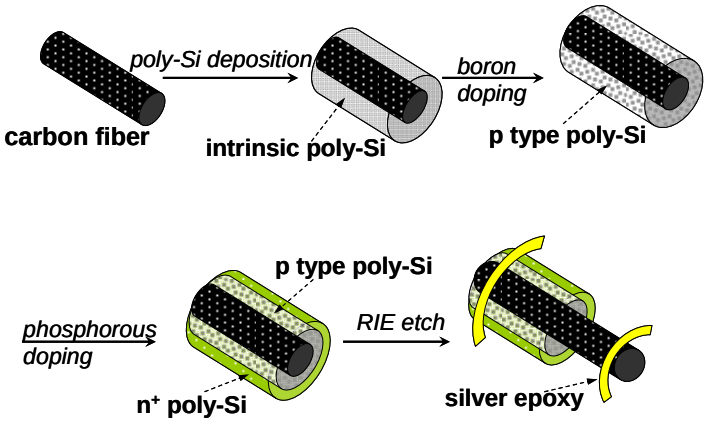

Figure 5.3: Scheme of fabrication process of the radial polysilicon p-n fiber solar cell.

violent chemical reaction. Therefore, a dry etching process of poly-Si was adopted, where a water soluble polymer (polyvinylpyrrolidone: water=1:2) was first cast to cover part of the fiber which served as a mask for the subsequent dry etching process of the poly-Si. The uncovered poly-Si shell was etched away by reactive ion etching (RIE) using SF_6 plasma to expose the underlying carbon fiber core electrode. The polymer was removed after the RIE process. In the last step, silver epoxy was applied on both the exposed CF core electrode and the top n-type poly-Si surface, serving as the electrode pads of the fiber PV to be connected to the external circuit.

The structure and the surface morphology of the fiber PV were investigated by scanning electron microscopy (Zeiss SEM Ultra60). The photovoltaic behavior of an 11 um-diameter single-fiber solar cell with a 500 um-long and a 2 um-thick Si shell layer was characterized with current density–voltage (J–V)-curve measurements in a solar simulator (imitating an air mass (AM) 1.5 spectrum, Oriel, 91160) with a light intensity

of 128 mW/cm^2 . During the testing, the fiber PV was placed directly under a lamp with a light area of 2 in × 2 in. The generated current was measured through a Keithley Model 2400 SourceMeter® with a resolution of 10pA.

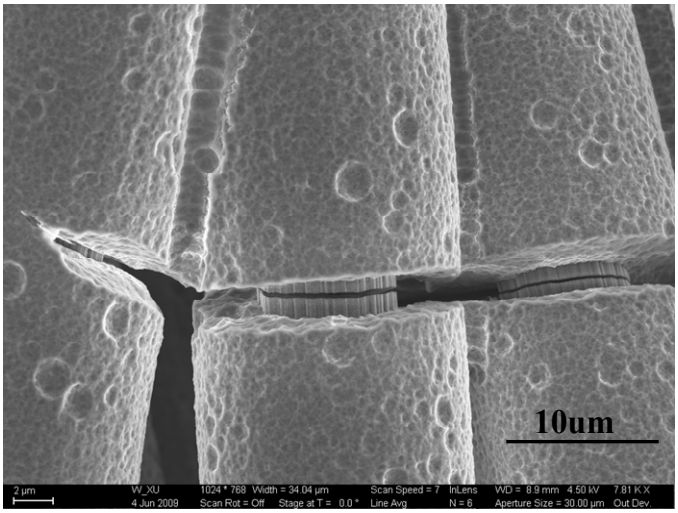

Figure 5.4: Poly-Si coated carbon fibers after wet chemical etching process of Poly-Si.

5.2.3 Morphology of the Fiber Solar Cell

As shown in Figure 5.5a and 5.5b, the as received carbon fiber has a diameter of 7 um and exhibits a rough surface topography with nano-sized trenches, which is considered to be a beneficial feature that can help to achieve a better interface strength between CF and poly-Si. A 200 um-diameter thread with twisted carbon fibers were coated with poly-Si through the process described in 5.2.2. SEM imaging studies showed that the Si-containing gases during the process were able to penetrate the CF bundle network and conformably/uniformly coat on CF fibers (Figure 5.5 c and 5.5d). The process flexibility of building uniform coaxial *p-n* diode on an individual micro-sized CF

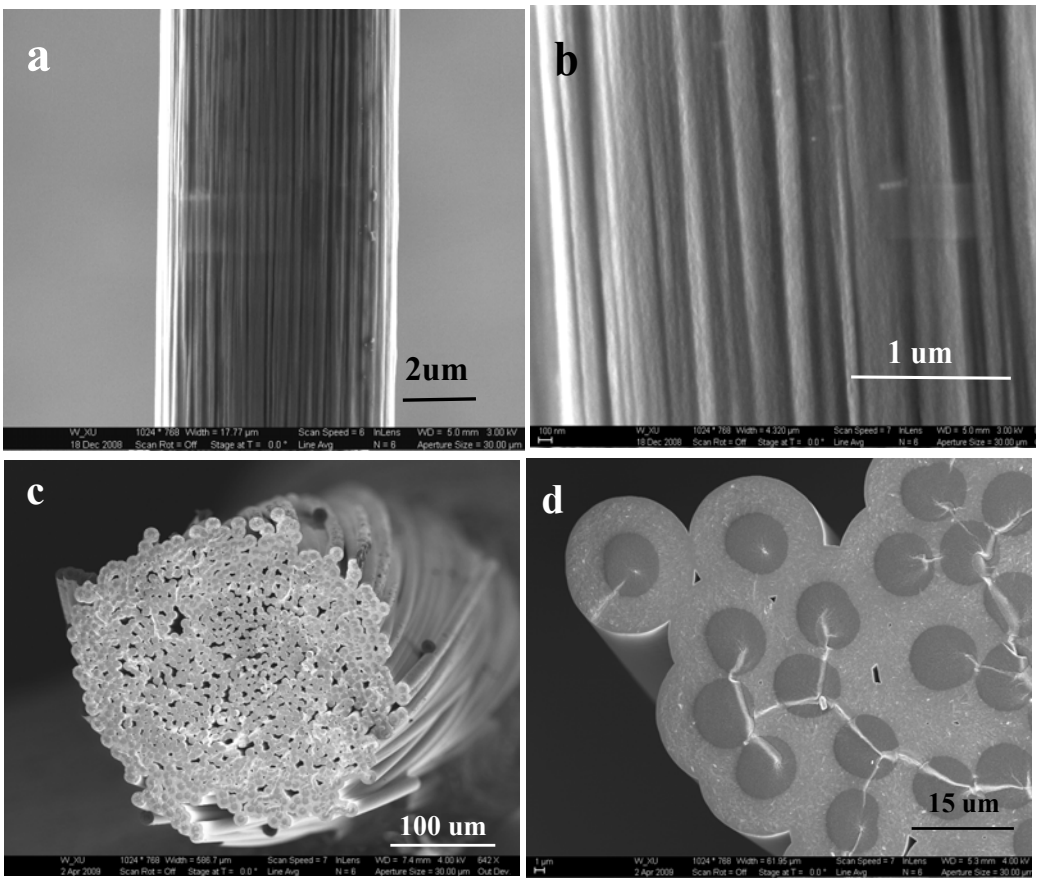

Figure 5.5: SEM image of (a) as received-CF, (b) close-up view of the CF surface, (c) a poly-Si coated CF bundle, and (d) close-up view of the poly-Si coated CF bundle.

was further evaluated. Conformal and uniform deposition of Poly-Si layer thicknesses ranging from 0.85 um (Figure 5.6a) to 10um (Figure 5.6c) on the cylindrical CF were demonstrated. In addition, the poly-Si was able to create a conformal coating around the two adjacent fibers (Figure. 5.6b). A good interface between the poly-Si shell and the CF core was achieved (Figure 5.6d), with the aid of slow ramp-up and ramp-down rates of the processing temperature during the deposition and diffusion, which minimized the negative effects due to the mismatch of the coefficients of thermal expansion between the poly-Si (3×10^{-6} K^{-1}) and the CF (0.5×10^{-6} K^{-1}).

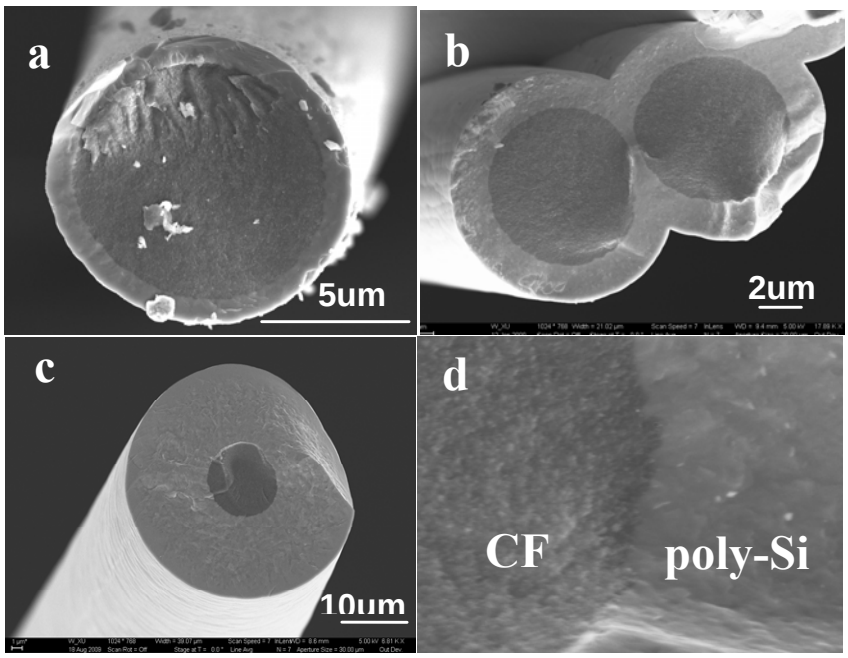

Figure 5.6: SEM image of cross-section of the CF coated with poly-Si with the thickness of (a) 0.85um, (b) 2 um, (c) 10 um, and (d) close up view of the CF/poly-Si interface.

SEM images in Figure 5.7a show the surface morphology of the fiber PV after the dry etching process of the poly-Si. The top n-type poly-Si layer exhibits a smooth texture with a grain size in the range of nanometers (Figure 5.7b). The CF after the RIE process maintained a relatively smooth surface topography as well (Figure 5.7c). The bulk resistivity of the CF before and after the device fabrication were measured to be 1.8×10^{-5} Ω·m and 1.9×10^{-5} Ω·m, respectively, which indicated its good thermal stability under the processing temperature of above 1000°C for several hours and good chemical resistance to the poly-Si etchant.

Figure 5.8 shows macro- and micro-scale views of a hairlike single fiber solar cell, with the digital image of a 4 cm-long PV fiber (Figure 5.8a) and the cross-sectional view of the solar cell (Figure 5.8b). A fiber-shape PV with a 2 um-thick *p-n* polysilicon

layer was fabricated on a 7 μm-diameter CF electrode for the examination of the photovoltaic behavior of the proposed PV protocol.

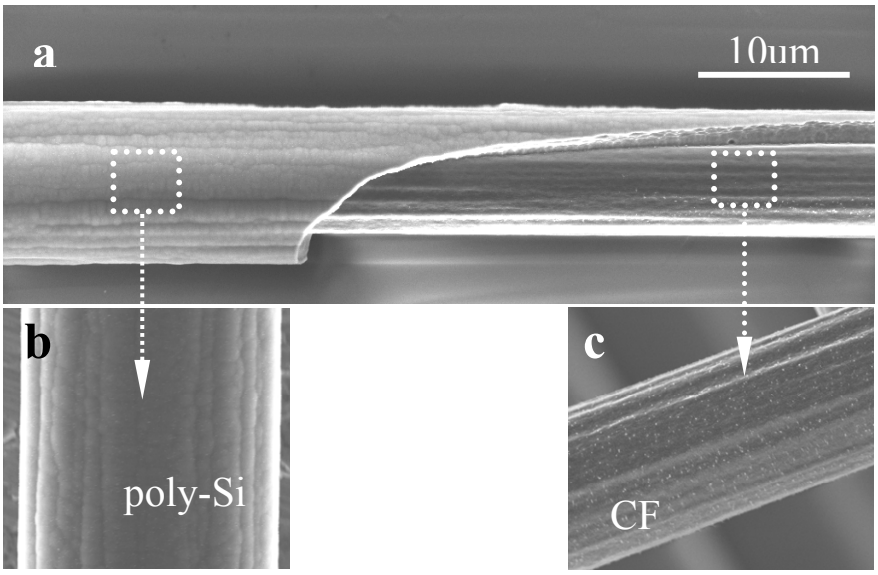

Figure 5.7: SEM image of (a) top surface of the solar cell, (b) carbon fiber (CF) after RIE etching of the poly-Si, and (c) a single fiber solar cell device.

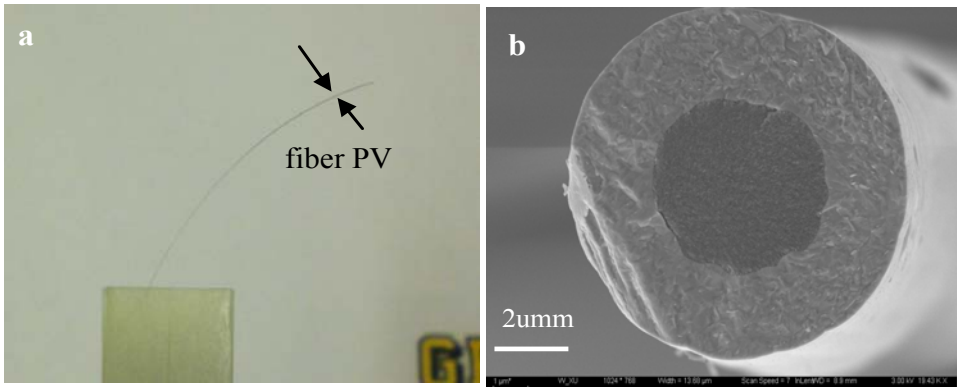

Figure 5.8: (a) Digital image of a hairlike solar cell (11 um-diameter), and (b) SEM image of the cross sectional view of a fiber type PV device with 2 um-thick doped poly-Si.

5.2.4 Current Density-Voltage (J-V) Characteristic of the Fiber Solar Cell

The performance of the aforementioned single-fiber solar cell was characterized with current density–voltage (J–V) curve measurements (Figure 5.9), where a voltage sweep was performed to the cell and the resulting output current density was measured simultaneously. Under illumination, the CF based solar cell with a 1×10^{-4} cm^2 effective area exhibited a photovoltaic effect and produced an open-circuit voltage of 0.14 V and a short-circuit current density of 1.7 mA/cm^2 (Table 5.1). The maximum current density and voltage were calculated to be 0.94 mA/cm^2 and 0.06V, which led to a power conversion efficiency of 0.04%.

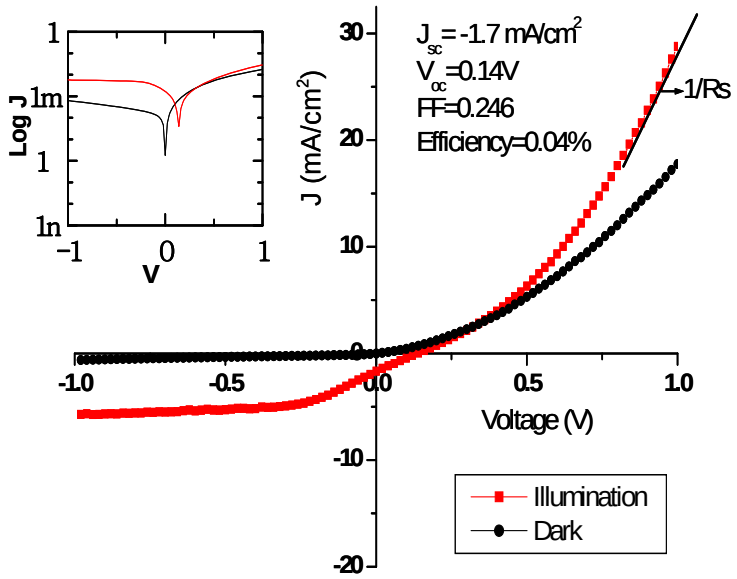

Figure 5.9: Experimental J-V characteristics of the CF based PV in the dark (black) and under illumination (red). Inset: Full-range curve in semi-logarithmic scale.

Table 5.1 Parameters of the CF-based Fiber PV

J_{sc} [mA/cm^2]	V_{oc} [mV]	J_{max} [mA/cm^2]	V_{max} [mV]	FF	R_SA [Ωcm^2]	$R_{SH}A$ [Ωcm^2]	Efficiency [%]
1.7	137	0.94	60	0.246	17	72	0.04

Comparing with a state of art poly-Si solar cell with a reported efficiency of 19.3%[24], the significant power losses in this un-optimized PV could be attributed to multiple factors. Further analysis of the data was performed to elucidate the causes and acquire useful information for optimization. In principle, the poly-Si solar cell in our system can be modeled according to the equivalent circuit illustrated in Figure 5.10, where a current source was connected in parallel with a diode and a shunt resistor, and was further connected a series resistor component. The output current density (J) can therefore be calculated as [25],

$$J = J_{sc} - J_0(\exp(\frac{q(V + JAR_S)}{nkT}) - 1) - \frac{V + JAR_S}{R_{SH}} \quad (5.1)$$

where J_{sc} is the short circuit current density, J_0 is the reverse saturation current density, q is the elementary charge, V is the output voltage, n is the ideality factor of the diode, k is Boltzmann's constant, T is the absolute temperature at which the cell is operated, A is the

effective area of the cell, R_S is the series resistance and R_{SH} is the shunt resistance. For an ideal cell, R_{SH} is infinite and would not provide an alternate

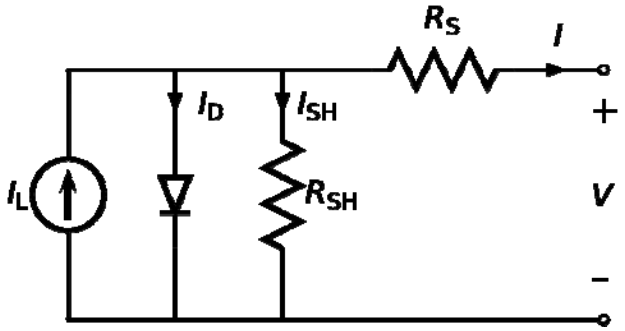

Figure 5.10: The equivalent circuit of a solar cell.

path for current to flow. R_S should be zero, resulting in no further V drop before the load. For real cells, these resistances can differ in value between the light and dark tests. Both R_S and R_{SH} can be approximated from the slopes of the I-V curve at V_{OC} and I_{SC} respectively. J_0 is a very important parameter which differentiates one diode from another. It is a measure of the carrier recombination in a device and a larger J_0 indicates a larger recombination.

In our study, the area normalized-series resistance ($r_s = A \cdot R_S$) of this initial cell device was found to be 17 $\Omega \cdot cm^2$, which is high compared to lab type solar cells and commercialized silicon solar panels (0.5~1.3$\Omega \cdot cm^2$). A high value of R_S will reduce the photogenerated current density as indicated in equation 5.1, as well as the fill factor (FF) [26], and consequently results in a low energy conversion efficiency (η) according to the equation:

$$\eta = \frac{P_{\max}}{P_{in}} = \frac{V_{\max} I_{\max}}{P_{in}} = \frac{FF \cdot V_{oc} \cdot I_{sc}}{P_{in}} \tag{5.2}$$

where P_{in} is the input power and P_{max} is the maximum power output. Compared with the state of art solar cell with a r_S of 0.5Ω·cm^2, the FF decreased from 0.8 to 0.26[27] for a PV with an area-normalized series resistance of 17Ω·cm^2, which lowered the efficiency by 3.2 times according to the equation:

$$\frac{\eta_i}{\eta_1} = \frac{P_{i\max}}{P_{1\max}} = \frac{FF_i \cdot V_{i-oc} \cdot I_{i-sc}}{FF_1 \cdot V_{1-oc} \cdot I_{1-sc}} \tag{5.3}$$

This high series resistance may be partially attributed to the high resistance of the CF itself due to its small diameter (7 um). The high surface resistance of the top thin n-type emitter and the contact resistance in the device may also add up to the R_S.

Similarly, the effect of the shunt resistance on the cell efficiency could also be evaluated. For the cell with an area normalized-series resistance (r_{sh}=A •R_{SH}) of 72Ω·cm^2, the FF reduced from 0.85 for the cell with infinite r_{sh} to 0.65[28]and the efficiency was reduced by 1.3 times according to the equation 5.3.

The reverse saturation current density, J_0, was calculated to be -2×10^{-4} A/cm^2 for the fiber PV. This value is much higher than the typical value in commercialized silicon solar cells (10^{-8} A/cm^2 ~ 10^{-12} A/cm^2), which indicates a high charge carrier recombination in the present cell. The recombination of the charge carriers usually has a great impact on the open circuit voltage and small effect on the short circuit current[26]. The relation of J_0 with V_{oc} and J_{sc} can be described as:

$$V_{oc} = \frac{kT}{q} \ln(\frac{J_{sc}}{J_0} + 1) \quad (5.4)$$

V_{oc} decreased significantly from 0.63V for a cell with a J_0 of 10^{-8} A/cm^2 to 0.15V for the cell with a J_0 of 10^{-4} A/cm^2. Therefore the efficiency could be reduced by more than 4 times. To reduce the carrier recombination and lower the J_0 may require the optimization of the grain size of the polysilicon[29] and the doping level of the n-type emitter[26].

The thin polysilicon layer in the present PV (~2um) may be another factor that is responsible for the power loss, since the theoretical studies have shown that the thickness of the poly-Si needs to be at least 20 um in order to absorb the majority of the incident solar radiation[30]. Yet considering the fact that the mechanical flexibility of the device may be compromised when the poly-Si layer thickness increases, the optimal thickness of the poly-Si needs to be studied. Another strategy is to introduce light trapping features into this fiber PV such as surface texture and back reflectors, where the efficiency of 10% could be potentially achieved for a 2-um thick polysilicon cell[31].

In summary, future studies can be focused on reducing the R_S and J_0, as well as optimizing the device architecture such as the thickness of the p-type poly-Si base layer to improve the overall performance of the CF based fiber PV.

5.2.5 Issues with Device Robustness

One issue that has been indentified is the mechanical strength of the developed fiber PV. As observed in the experiments, these fibers tended to break during handling. SEM image in Figure 5.110 further revealed that cracks were generated in fibers coated with a 4 um-thick poly-Si layer, which could be reasonably attributed to the brittleness of

the poly-Si. Possible approaches to resolve this issue may be either to reduce the thickness of the poly-Si or to resort to another photosensitive material with higher ductility such as amorphous silicon.

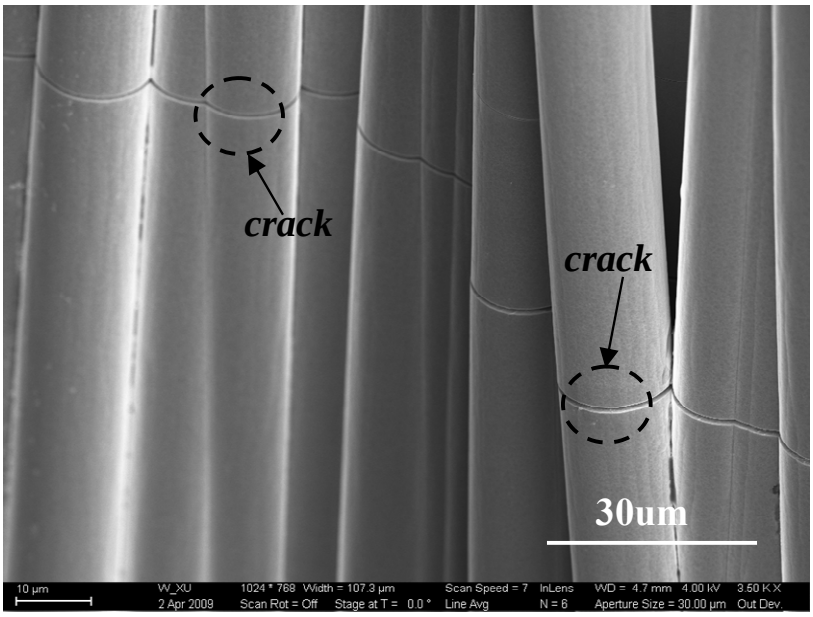

Figure 5.11: SEM image of cracks in CF/poly-Si composite fibers.

5.3 Summary

In this chapter, the feasibility of the carbon fiber as a MEMS substrate was explored in an energy harvesting system. A CF-based solar cell with a radially-modulated *p-n* silicon diode has been designed and successfully fabricated through the conventional MEMS fabrication techniques. The developed process was able to accomplish the deposition of high quality photoactive materials with tunable physical structures. The

photovoltaic effects of the present fiber PV was demonstrated with an output power density of 0.059mW/cm^2. The output current and voltage could be further scaled up by connecting each fiber solar cell in series and/or in parallel to meet the specific power requirement of certain MEMS systems and wearable devices. The feasibility of CF serving as both building block and electrode of the fiber PV has also been demonstrated. Future work can be focused on optimizing the device architecture and reducing the series resistance to improve the power conversion efficiency, and meanwhile resolving the issue of the composite fiber breakage.

5.4 References

(1) Madou, M. J.; Zaouk, R.; Wang, C.; Park, B. Y. *ECS Transactions* **2006**, *1*, 1.

(2) Wang, C. T., Lili; Jia, Guangyao; Kassegne, Sam; Zoval, Jim V.; Madou, Marc J. *MEMS, MOEMS, and Micromachining, Proceedings of the SPIE* **2004**, *5455*, 295.

(3) Peiner, E.; Tibrewala, A.; Bandorf, R.; Luthje, H.; Doering, L.; Limmer, W. *Journal of Micromechanics and Microengineering* **2007**, *17*, S83.

(4) Luo, J. K.; Fu, Y. Q.; Le, H. R.; Williams, J. A.; Spearing, S. M.; Milne, W. I. *Journal of Micromechanics and Microengineering* **2007**, *17*, S147.

(5) Schueller, O. J. A.; Brittain, S. T.; Marzolin, C.; Whitesides, G. M. *Chemistry of Materials* **1997**, *9*, 1399.

(6) Unalan, H. E.; Wei, D.; Suzuki, K.; Dalal, S.; Hiralal, P.; Matsumoto, H.; Imaizumi, S.; Minagawa, M.; Tanioka, A.; Flewitt, A. J.; Milne, W. I.; Amaratunga, G. A. J. *Applied Physics Letters* **2008**, *93*.

(7) www.mezmeriz.com. Retrieved March 25, 2011,

(8) Tian, B.; Kempa, T. J.; Lieber, C. M. *Chemical Society Reviews* **2009**, *38*, 16.

(9) Tian, B.; Zheng, X.; Kempa, T. J.; Fang, Y.; Yu, N.; Yu, G.; Huang, J.; Lieber, C. M. *Nature* **2007**, *449*, 885.

(10) Lee, J. B.; Chen, Z. Z.; Allen, M. G.; Rohatgi, A.; Arya, R. *Journal of Microelectromechanical Systems* **1995**, *4*, 102.

(11) Fan, Z.; Razavi, H.; Do, J.-w.; Moriwaki, A.; Ergen, O.; Chueh, Y.-L.; Leu, P. W.; Ho, J. C.; Takahashi, T.; Reichertz, L. A.; Neale, S.; Yu, K.; Wu, M.; Ager, J. W.; Javey, A. *Nat Mater* **2009**, *8*, 648.

(12) Toivola, M.; Ferenets, M.; Lund, P.; Harlin, A. *Thin Solid Films* **2009**, *517*, 2799.

(13) O'Connor, B.; Pipe, K. P.; Shtein, M. *Applied Physics Letters* **2008**, *92*.

(14) Fan, X.; Chu, Z. Z.; Chen, L.; Zhang, C.; Wang, F. Z.; Tang, Y. W.; Sun, J. L.; Zou, D. C. *Applied Physics Letters* **2008**, *92*.

(15) Kayes, B. M.; Richardson, C. E.; Lewis, N. S.; Atwater, H. A. Photovoltaic Specialists Conference, 2005. Conference Record of the Thirty-first IEEE, 2005; p 55.

(16) Lee, M. R.; Eckert, R. D.; Forberich, K.; Dennler, G.; Brabec, C. J.; Gaudiana, R. A. *Science* **2009**, *324*, 232.

(17) Fan, X.; Chu, Z. Z.; Wang, F. Z.; Zhang, C.; Chen, L.; Tang, Y. W.; Zou, D. C. *Advanced Materials* **2008**, *20*, 592.

(18) Weintraub, B.; Wei, Y. G.; Wang, Z. L. *Angewandte Chemie-International Edition* **2009**, *48*, 8981.

(19) Fan, X.; Wang, F. Z.; Chu, Z. Z.; Chen, L.; Zhang, C.; Zou, D. C. *Applied Physics Letters* **2007**, *90*.

(20) Liu, Z.; Subramania, V.; Misra, M. *The Journal of Physical Chemistry C* **2009**, *113*, 14028.

(21) Lee, J. A.; Lee, S.; Lee, K. C.; Il Park, S.; Lee, S. S. *Journal of Micromechanics and Microengineering* **2008**, *18*.

(22) Abdel Gawad, O.; Abou Tabl, M. H.; Abdel Hamid, Z.; Mostafa, S. F. *Surface and Coatings Technology* **2006**, *201*, 1357.

(23) Lewis, N. S. *Science* **2007**, *315*, 798.

(24) http://techon.nikkeibp.co.jp/english/NEWS_EN/20100217/180340/.Retrieved march 25, 2011.

(25) Nelson, J. *The Physics Of Solar Cells*; UK: Imperial College Press, 2003.

(26) Boxwell, M. *Solar Electricity Handbook, 2010 Edition: A Simple Practical Guide to Solar Energy - Designing and Installing Photovoltaic Solar Electric Systems* Greenstream Publishing, 2010.

(27) http://pvcdrom.pveducation.org/CELLOPER/SERIES.HTM. Retrieved March 25, 2011,

(28) http://pvcdrom.pveducation.org/CELLOPER/SHUNT.HTM. Retrieved March 25, 2011,

(29) Kumari, S.; Arora, N. K.; Jain, G. C. *Solar Energy Materials* **1981**, *5*, 383.

(30) ZOHRA BENMOHAMED, M. R. In *Proceedings of the 5th WSEAS Int. Conf. on Microelectronics, Nanoelectronics, Optoelectronics* Prague, Czech Republic, 2006.

(31) Yamamoto, K. *Electron Devices, IEEE Transactions on* **1999**, *46*, 2041.

CHAPTER 6

CONCLUSIONS AND RECOMMENDATIONS

This PhD work investigated approaches to effectively incorporate the unique and superior properties of two carbon materials, carbon nanotubes and carbon fiber, as either key functional components or unconventional substrates in MEMS systems. Their performance in three different types of MEMS devices, namely, strain/stress sensors, vibration power generators, and fiber solar cells, were evaluated and the working mechanisms of these two non-traditional materials in these systems were discussed. The study can potentially enable the development of new types of carbon-MEMS devices.

The reason that carbon nanotubes were selected was due to several advantageous characteristics this nanomaterial offers. They carry extremely high Young's modulus (E_y=1TPa), superior electrical properties (current density of 4×10^9 A/cm^2), exceptional piezoresistivity (G=2900), and unique spatial format (high aspect ratio hollow nanocylinder), among other properties. If properly utilized, all these merits can give rise to a variety of new types of carbon nanotube based micro- and nano-electronics that can greatly fulfill the need for the next generation of faster, smaller and better devices. However, before these functions can be fully realized in a nano/microsystem, one substantial issue to cope with is how to implement CNTs into these systems in an effective and controllable fashion. Challenges associated with CNTs integration include very poor dispersibility in solvents, lack of melting/sublimation point, and unfavorable rheology with regard to mixing and processing highly viscous, CNT-loaded polymer solutions. These issues hinder the practical progress of CNTs from being studied in a lab

scale as well as applied in the industrial level. Therefore, a MEMS-assisted electrophoretic deposition technique was first developed, aiming to achieve controlled integration of CNT into both conventional and flexible microsystems. MEMS technology has demonstrated strong capability in developing silicon and metal based microsystems. In this thesis, this mature technique was exploited to generate different microelectrode structures to facilitate the micropatterning and manipulation of the CNTs. Selective deposition of electrically charged CNTs onto desired location of these microstructures was realized through spatial control of the electric field lines in the EPD process. Through the combination of the aforementioned technique and transfer micromolding process, the generated CNT patterns can be transferred to the flexible polymeric substrate, which eliminates the rheology issue associated with the mixing of CNT with viscous polymers, while simultaneously maintaining the spatial geometry of the CNT patterns. A variety of 2-D and 3-D micropatterns of CNTs with wafer-scale areas have been successfully achieved in both rigid and elastic systems at room temperature with relatively high throughput. This approach was capable of generating desired localized CNT assembly on three sets of conventional MEMS microstructures, including interdigitated microelectrode arrays, silicon microchannels and photoresist microstructures. The deposited CNT layer thickness exhibited monotonic increase with the increase of applied electric field and deposition time when other process parameters were kept constant, which was in good agreement with the theoretical predication of EPD of spherical particles. Controllable CNT layer thicknesses ranging from 133nm to the micrometer range were accomplished within 5 min in a single step at room temperature. Moreover, the morphology of the assembly film and the porosity of the CNT film were

found to be readily controllable through the manipulation of deposition parameters. Under appropriate deposition conditions, CNTs only assembled on energized electrodes, leaving un-energized microelectrodes with no deposition. It was also observed that CNT deposited conformally around the SU-8 microwell inner surface and generated a 20 μm wide circular belt around the well opening, creating a continuous 3-D coating in each isolated well. Similar assembly behavior was revealed in rectangular microchannels constructed of photoresist, where a rectangular CNT belt was generated around the channel opening. This phenomenon was considered to arise from the conformal coating nature of the EPD process. The resultant CNT network displayed a random planar distribution with a certain degree of local orientation when the feature size of the microstructures was sufficiently small. For this technique, high surface hydrophobicity of the non-conductive regions in microstructures was found to be critical to accomplish selective micropatterning of CNTs. Microstructures with hydrophilic dielectric regions yielded no selective patterning of the CNTs, which was considered to be partially due to the potential wetting effect in the non-conductive hydrophilic regions. Compared with other reported CNT patterning processes, this process offers several favorable advantages simultaneously such as high throughput, room temperature processing, good control over deposited mass, relatively high resolution, and the ability to achieve micropatterns of pristine CNTs over a large scale on both rigid and compliant substrates. This approach may also be extended to the co-electrophoresis or successive deposition of different materials to enable the fabrication of advanced CNT-based hybrid nanostrucutres for a variety of functional, structural and biomedical applications.

Upon clearing the hurdles of the CNT pattering, the exceptional and unique

piezoresistive, structural and electrical characteristics of a specially constructed PDMS/CNTs nanocomposite fabricated through the approach developed previously were incorporated, investigated and validated in force/strain microsensors and electret-based energy harvesters. The nanocomposite combines the excellent piezoresistive and charge storage properties of the CNTs with the ductility of the polymer simultaneously, in an effort to develop conformal, low cost and mechanically elastic/flexible electronics with tunable properties.

The resultant PDMS/CNT composite exhibited a bi-layer structure and demonstrated very high sensitivity to both transverse compressive force and tensile strain. The gauge factor in tensile strain sensing was found to have a strong dependence on both the initial resistance of the PDMS/CNTs composite and the applied strain, which could be attributed to the different piezoresistive mechanisms (piezoresistivity induced by tunneling resistance change and intrinsic piezoresistivity of CNT) in this system. The morphology and entanglement of the CNT network showed a significant influence on the piezoresistivity of the PDMS/CNT composite, which suggested that the sensitivity of such materials can be readily tailored through the fabrication parameters discussed in Chapter 1. These results provide useful guidance for the design and fabrication of the strain/stress sensors with a specific sensitivity and the prediction of the performance could be obtained through controlling the process parameters. Moreover, the PDMS/CNT bi-layer material in this study exhibits much higher or comparable strain sensitivity, compared with traditional metal foil strain sensors (G=2.1) or silicon piezoresistors (G<120), with additional advantage of larger working range (>10%) before device failure. The patterned PDMS/CNTs flexible composite developed in this work can be potentially

utilized to sense and monitor local pressure or structural change in tissues or micro-fluidic systems, as well as flexible 3-D microsystems. However, one issue remaining is the hysteresis behavior of the composite material at high applied strain level (>3%), which could be a limit for the accuracy of this type of sensors. A specially designed data recording program may be required to resolve this problem.

In addition to being utilized as strain sensors, the micropatternable PDMS/CNT composite was further investigated as an elastic electret. During the fabrication process, an ultra-thin film of PDMS was formed *in situ* on the top surface of the PDMS/CNT composite. Electrons injected during the corona charging process were found to be capable of penetrating this dielectric layer and becoming trapped inside the PDMS/CNT composite, which exhibited charge retention characteristics. The material exhibited electret characteristics with charge storage stability in excess of 280 hours. The power generation capacity of the corona-charged composite has been characterized and successfully demonstrated in detail in both a ball drop experiment and the cyclic mechanical load experiments. The results indicated that the composite combining two non-electret materials can store charges, which may be conveniently utilized and conformably implemented into shoes, car tires or playgrounds for a large area and low cost flexible energy harvesting system. Nevertheless, this composite material suffers from relative charge storage stability and low power generation. The low bulk resistivity and high gas permeability of the PDMS could be the two factors that are responsible for these issues. Future work can be focused on replacing the PDMS with some other polymers/elastomers with higher bulk resistivity and low gas permeability such as fluorinated-PDMS or polyurethane.

In addition to exploiting CNTs as functional components in MEMS systems, the feasibility of extending the application of another carbon material, carbon fiber, to serve as a substrate/building block for MEMS devices was explored. Though carbon fiber has been utilized as a flexible spring in MEMS scanning micro-mirror array, its full potential in advanced electronics has yet not been fully tapped. The excellent Young's modulus (E_y=530GPa), fiber-shape geometry with micro-scale diameter and macro-scale length, superior thermal stability (up to 1500 °C), good electrical conductivity (10^6 S/m) and roll-to-roll processability of the CF suggest that it can serve as both a building block and the electrode in constructing next generation of hairlike silicon solar cells for wearable or stealth devices. In this study, a CF-based solar cell with a radially-modulated *p*-*n* silicon diode has been designed and successfully fabricated through conventional MEMS fabrication techniques. The developed process was capable of accomplishing the deposition of high quality photoactive materials with tunable physical structures. The CF acted as both building block and electrode in this solar cell configuration. The photovoltaic effects of the present fiber PV was demonstrated with an open-circuit voltage of 0.14 V, a short-circuit current density of 1.7 mA/cm^2, and output power density of 0.059mW/cm^2. The output current and voltage could be further scaled up by connecting each fiber solar cell in series and/or in parallel to meet the specific power requirement of certain MEMS systems and wearable devices. Despite the success in proof of concept of the CF fiber PV, the current solar cell still suffered from low energy conversion efficiency (0.04%). Further analysis of the cell performance was conducted to elucidate the possible causes. High series resistance, pronounced charge carrier recombination, and thin light absorbing layer in this initial cell were found to be the

possible factors that led to the power loss. To improve the power conversion efficiency, and meanwhile to avoid the potential issue of the fiber breakage when the silicon layer thickness increases substantially, several optimization strategies can be taken. First, the design of the overall architecture of the fiber PV can be parameterized and optimized by simulation software/tools such as Solar Advisor Model (SAM) and RETScreen®. The optimal sheet resistance of the n-type emitter and the junction depth, as well as the suitable layer thickness of the base layer may be obtained. Moreover, in an effort to maintain the flexibility of the fiber PV, an alternative photoactive material that has a higher light absorption coefficient such as amorphous silicon can be applied into this system.